AN ABSTRACT OF THE THESIS OF

John Barry King Jr. for the degree of Doctor of Philosophy in Mechanical Engineering and Nuclear Engineering presented on May 1, 1991.

Title: A Study of Buoyant Backflow in Vertical Injection Lines

Redacted for privacy

Abstract approved: _____
Lorin R. Davis

Redacted for privacy

Abstract approved: _____
Jose N. Reyes Jr.

In the event of a small break loss of coolant accident (SBLOCA) in a nuclear reactor, cold fluid is injected through the reactor system high pressure injector to compensate for the coolant loss. When this flow rate is less than a critical value, however, the hot fluid in the cold leg penetrates into the vertical injection line in a process called buoyant backflow. Because the resulting penetrations induce thermal stresses in the pipe, the presence of backflow in the injection lines is potentially significant.

Since these penetrations could potentially damage the pipe, it was the purpose of this study to evaluate the backflow behavior. To this end, both the critical injection conditions and the subcritical penetration depth were experimentally determined through flow simulation in a 1/5 scale model. In addition, the experimental trends were

modeled theoretically. By matching the theoretical results to the experimental data, it was determined that backflow began below a critical Froude number of .65 and increased in depth with the negative logarithm of the injection velocity. The agreement between theory and experiment was excellent.

For a certain class of reactor systems, the full scale Froude numbers were then compared to the critical value obtained in the analysis. For the systems involved in this comparison, the full scale Froude numbers were shown to be less than .65 for all practical flow rates. As a consequence, buoyant backflow is expected within the injection lines of these reactors, under safety injection conditions.

A Study of Buoyant Backflow in Vertical Injection Lines

by

John Barry King Jr.

A THESIS

submitted to

Oregon State University

in partial fulfillment of
the requirements for the
degree of

Doctor of Philosophy

Completed May 1, 1991

Commencement June 1991

APPROVED:

Redacted for privacy

Professor of Mechanical Engineering in charge of major

Redacted for privacy

Head of department of Mechanical Engineering

Redacted for privacy

Professor of Nuclear Engineering in charge of major

Redacted for privacy

Head of department of Nuclear Engineering

Redacted for privacy

Dean of Graduate School

Date thesis is presented May 1, 1991

Typed by John King for John Barry King Jr.

ACKNOWLEDGEMENT

I wish to acknowledge PGE for supporting this research and the U.S. Department of Energy for financial support received during my first four years of graduate school. This support was received through the Nuclear Engineering, Health Physics, and Radioactive Waste Management Fellowship Program administered by Oak Ridge Associated Universities for the U.S. Department of Energy. I especially wish to thank Dr. Jose Reyes for developing this project and for his selfless assistance in seeing me through my doctoral program. Without the valuable insights of Dr. Lorin Davis this project would not have been possible. I thank him. I am also extremely grateful for the previous research of Drs. F.K. Moore and Vijay Modi, which formed the background for this analysis. In addition, I appreciate the patience shown by Dana Cramer and Robin Keen in helping me operate the word processor.

On a more personal level, I wish to thank my wife, Donna, for her patience with my schedule and for her assistance with the figures. I also wish to thank my grandparents for taking me at a young age and raising me as their own. It is the result of their nurturing that this effort is possible. In addition, I must express my gratitude to Dr. Samim Anghaie, a former professor and a dear friend. He led me into the field of reactor thermal hydraulics and has helped me to see my potential.

Finally, I wish to thank God the Father Almighty, Creator of Heaven and Earth. It is only on the basis of His Grand Design that mankind has any hope of discovering scientific order, and all scientific discoveries therefore reveal His Handiwork.

TABLE OF CONTENTS

LIST OF FIGURES

LIST OF TABLES

A STUDY OF BUOYANT BACKFLOW IN VERTICAL INJECTION LINES

CHAPTER 1

INTRODUCTION

1.1 Problem Description

In the event of a small break loss of coolant accident (SBLOCA), cold fluid is injected through the reactor system high pressure injector (HPI) to compensate for the loss of reactor coolant and lower the system temperature. A potential problem with this injection process, however, is that high density cold fluid is injected over lighter hot fluid. When the injection velocity is less than a critical value, the hot fluid penetrates into the HPI in a process called buoyant backflow as shown in Figure 1.1. In this process the resulting penetrations are chaotic in nature, rising to a zenith, where they persist momentarily, and then suddenly break up.

Since the penetrations occur nonuniformly around the periphery of the HPI, they induce circumferential temperature gradients and consequent thermal stresses in the HPI piping. Moreover, the coupling of the induced stress with the cyclic nature of buoyant backflow creates thermal fatigue which increases with each penetration. If the fatigue should become severe, the pipe may crack, increasing

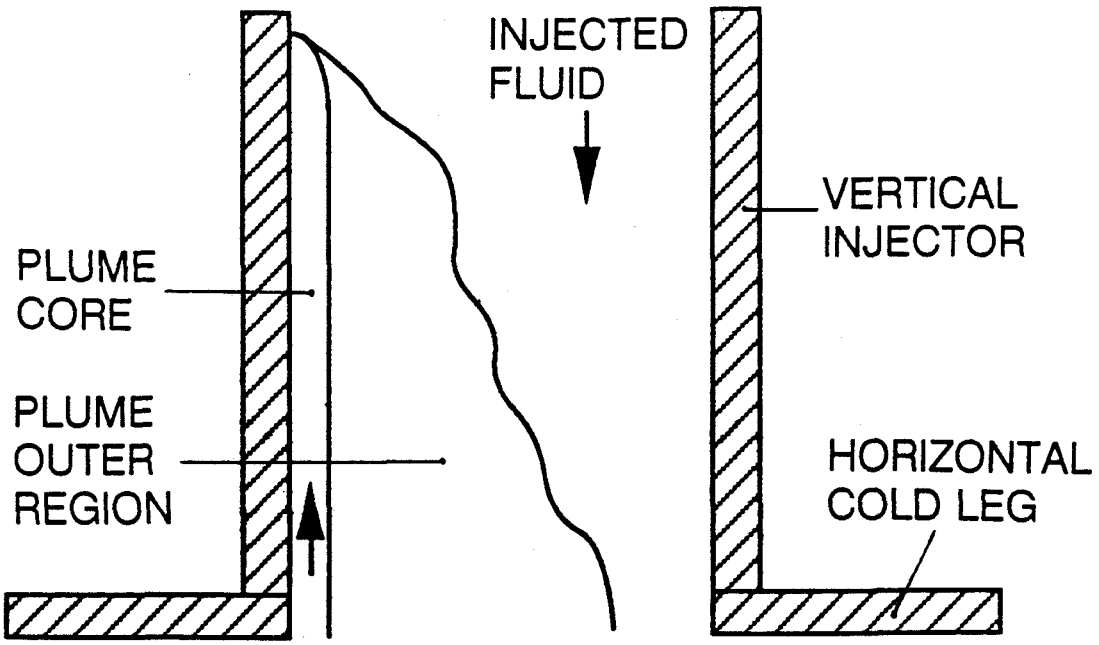

Figure 1.1 Buoyant Backflow in Vertical Injection Lines.

the loss of coolant for which the injection was initially supposed to compensate. As shown in Appendix 1, such cracking has already occurred in two plants where leaking valves allowed cold fluid to pass continuously through the injection lines[1],[2]. Because the resulting flow rates were extremely low, the pipes were subjected to cyclic thermal stratification and consequent thermal fatigue.

Since cracking has already resulted from valve leakage, it is possible that such cracking may occur during a SBLOCA as well. In addition, the potential for such cracking may be increased as a result of the leakage problem. For example, if valve leakage has damaged the HPI prior to the SBLOCA, a greater possibility exists for cracking to occur during this transient. Furthermore, since conditions may arise during a SBLOCA which cause one of the cooling loops to stagnate, the effects of cracking and loop stagnation may combine to reduce the reactor cooling capacity with serious consequences.

Although a complete investigation of buoyant backflow would require an analysis of the material effects, the first step in this process is to determine the injection behavior during a SBLOCA. Under these conditions, as will be shown later, the injection flow rates are turbulent and the primary fluid remains in its liquid phase. For these reasons the present research involves the study of buoyant backflow under turbulent injection conditions. In particular, it will be the objective of the subsequent

analysis to determine the critical conditions and the subcritical penetration behavior as functions of both the injection flow rate and fluid buoyancy. To simplify this analysis the case of loop stagnation will be assumed.

To begin this investigation it is first necessary to become more familiar with the problem at hand. For this reason the significant parameters governing buoyant backflow will first be derived. Once these parameters have been determined, previous research on buoyant penetrations will then be presented to gain additional understanding. Finally, based on this information the procedure undertaken to satisfy the research objectives will be briefly outlined.

1.2 Parameters Governing the Problem

To gain some sense of direction in the present study, it is necessary to obtain the relevant dimensionless groups. In this regard, there are two ways to proceed. The first is to determine all significant variables intuitively and then group them using the Buckingham Pi theorem. The second is to nondimensionalize the governing equations directly. Clearly, since three conservation equations govern the backflow process, all significant variables could be obtained from these equations, eliminating the need for guess work. Additionally, the variables so obtained would arise in a physical context that makes their meaning clear. Since the resulting dimensionless groups would therefore

also be physically meaningful, the second approach will be used in the present analysis.

To obtain all the relevant parameters it is first necessary to apply the conservation equations in a manner that includes all possible effects. For example, when studying the onset of buoyant backflow, the pipe and jet regions are both important as shown in Figure 1.2a. Inside the HPI the buoyancy is zero, and the gradient of the dynamic pressure drives the flow. In the jet, however, the reverse is true. To include both effects, it would be necessary to apply the conservation equations to each domain separately. When studying the depth of penetration, on the other hand, the effects of buoyancy and dynamic pressure are simultaneously important as shown in Figure 1.2b. In addition, since azimuthal symmetry no longer exists, angular derivatives, previously unimportant, are now significant. Because all of the relevant effects are simultaneously present in this case, it will be chosen for dimensional analysis.

Having chosen the domain of application, it is next necessary to discuss the equations themselves. Since the present problem involves a turbulent pipe flow, the governing equations will be the turbulent, Navier-Stokes equations in cylindrical geometry. In their complete form these equations are quite formidable. In addition to being time dependent, they contain three dimensional diffusive, convective, and turbulent transfer terms as well.

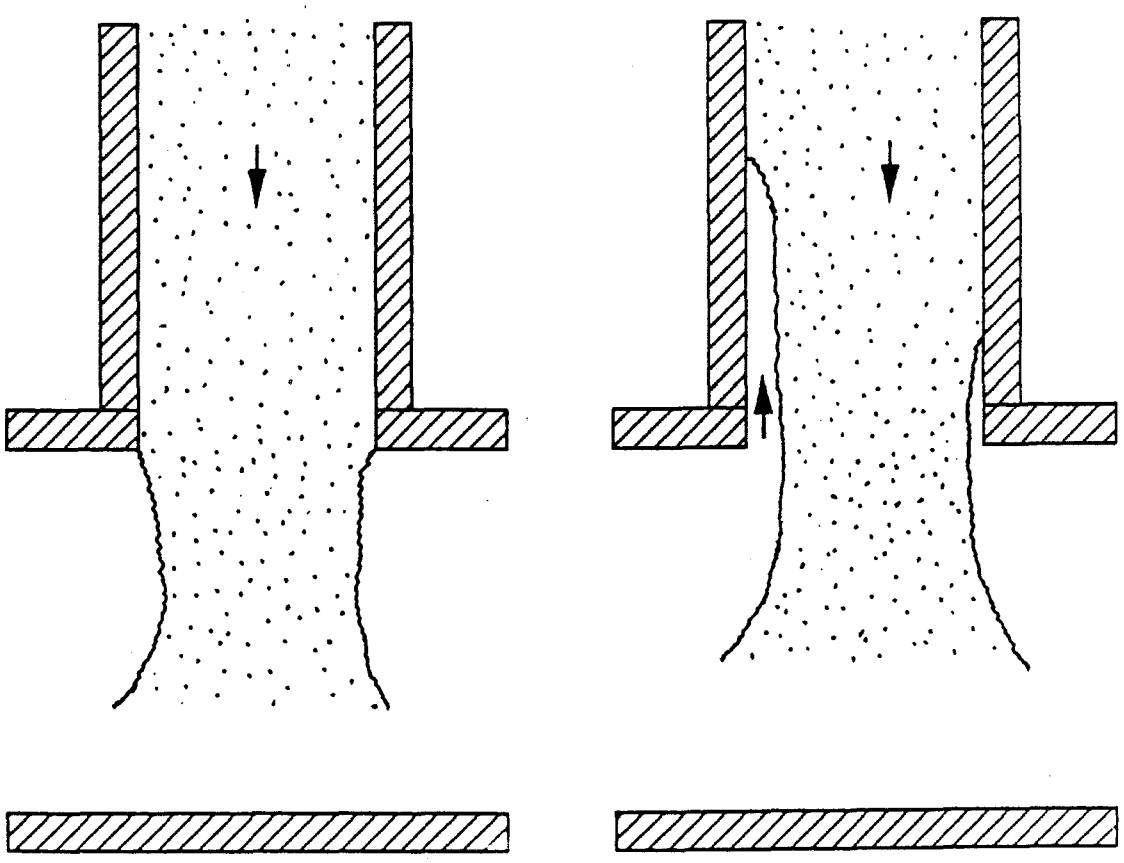

1.2A: ONSET

1.2B: PENETRATION

Figure 1.2 Illustration of the Different Fluid Regions Significant to Buoyant Backflow

Fortunately, however, the problem physics may be invoked to eliminate several of these terms. First, by assuming the plume to be steady at its maximum height, the transient terms may be eliminated. Next, by comparing the diffusive terms to their turbulent counterparts, the diffusive terms may be neglected as well. Third, vertical turbulence may be neglected in comparison to vertical bulk motion due to its relative insignificance. In the polar directions, however, the bulk motion may be assumed negligible, making the turbulent motions dominant. Finally, the Boussinesq approximation may be invoked to eliminate the effects of density differences in the nonbuoyant terms of the continuity and momentum equations.

With these assumptions the third conservation equation, which is usually written in terms of temperature or concentration, may be re-expressed in terms of fluid density differences alone. Implementing these assumptions in the turbulent Navier-Stokes equations yields.

$$\frac{\partial \overline{V_z}}{\partial z} = 0 \tag{1.1}$$

$$\rho_L \overline{V_z} \frac{\partial \overline{V_z}}{\partial z} = - \frac{\partial P}{\partial z} - \rho_L g - \rho_L \frac{1}{r} \frac{\partial (r \overline{V_r' V_z'})}{\partial r} - \rho_L \frac{1}{r} \frac{\partial (\overline{V_\theta' V_z'})}{\partial \theta} \tag{1.2}$$

$$\overline{V_z}\frac{\partial\overline{\Delta\rho}}{\partial z} = -\frac{1}{r}\frac{\partial(r\overline{V_r'\Delta\rho'})}{\partial r} - \frac{1}{r}\frac{\partial(\overline{V_\theta'\Delta\rho'})}{\partial\theta} \tag{1.3}$$

In these expressions the term, ρ_L, is used to denote the density of the light fluid in the plume.

To put these equations in a better form, it is necessary to determine the pressure gradient in the pipe. To this end it will be assumed that the backflow penetration does not disturb the pressure distribution in the HPI line. As a consequence, the pressure gradient may be determined from its previous value before the penetration occurred. Under those conditions, the flow was fully developed, producing a force balance between pressure, gravity, and the wall shear stress. By letting C_f and ρ_H represent the friction factor and the density of the heavy fluid in the pipe, this force balance may be expressed as

$$(P|_z - P|_{z+dz})\frac{\pi D^2}{4} + C_f\frac{(\rho_H\overline{V_z}^2)}{2}\pi D dz - \rho_H g\frac{\pi D^2}{4}dz = 0 \tag{1.4}$$

Upon rearrangement this yields

$$-\frac{\partial P}{\partial z} = \rho_H g - 2\rho_H C_f\frac{\overline{V_z}^2}{D} \tag{1.5}$$

Replacing the pressure gradient in equation (1.2) by this expression, ignoring the density differences in the nonbuoyant terms and expressing the remaining densities as simply ρ, yield the final form of the momentum equation.

$$\overline{V_z}\frac{\partial \overline{V_z}}{\partial z} = g\frac{\Delta\rho}{\rho} - 2C_f\frac{\overline{V_z}^2}{D} - \frac{1}{r}\frac{\partial(r\overline{V_r'V_z'})}{\partial r} - \frac{1}{r}\frac{\partial(\overline{V_\theta'V_z'})}{\partial \theta} \tag{1.6}$$

Having re-expressed the momentum equation, it is clear that equations (1.1), (1.3), and (1.6) constitute the new set governing equations. As a consequence, they form the basis for obtaining relevant dimensionless groups. To obtain these dimensionless groups, a length scale, a velocity scale, and a reference density difference may be introduced to nondimensionalize the problem variables and the governing equations. If these scales are denoted L_o, V_o, and $\Delta\rho_o$, respectively, then the nondimensional variables (asterisks) may be defined to be:

$$(r_*, D_*, z_*) = \frac{(r, D, z)}{L_o}\,;\ (V_{r*}', V_{\theta*}', \overline{V_{z*}}) = \frac{(V_r', V_\theta', \overline{V_z})}{V_o}\,;\ \Delta\rho_* = \frac{\Delta\rho}{\Delta\rho_o}, \tag{1.7}$$

and the angle, Θ, already dimensionless, remains unchanged. Substituting these relations into (1.1), (1.3), and (1.6)

yields

$$\frac{\partial \overline{V_{z*}}}{\partial z_*} = 0 \tag{1.8}$$

$$\overline{V_{z*}}\frac{\partial \overline{V_{z*}}}{\partial z_*} = \left[\frac{g\Delta\rho_o L_o}{\rho V_o^2}\right]\Delta\rho_* - \left[\frac{C_f}{D_*}\right]2\overline{V_{z*}}^2 - \frac{1}{r_*}\frac{\partial(r_*\overline{V'_{r*}V'_{z*}})}{\partial r_*} - \frac{1}{r_*}\frac{\partial(\overline{V'_{\theta*}V'_{z*}})}{\partial \theta_*} \tag{1.9}$$

$$\overline{V_{z*}}\frac{\partial \overline{\Delta\rho_*}}{\partial z_*} = -\frac{1}{r_*}\frac{\partial(r_*\overline{V'_{r*}\Delta\rho'_*})}{\partial r_*} - \frac{1}{r_*}\frac{\partial(\overline{V'_{\theta*}\Delta\rho'_*})}{\partial \theta_*} \tag{1.10}$$

To obtain the dimensionless groups initially sought, it is necessary to interpret the equations just derived. The significance of these equations is that as a result of their nondimensionalization, the variables have been normalized with the effects of the scales isolated in the coefficients. In addition, the boundary conditions which are not shown have also been nondimensionalized. Ordinarily these would introduce certain aspect ratios (ratios of length scales) into the problem. Theoretically, the nondimensional differential equations could be solved subject to their dimensionless boundary conditions. The resulting

dimensionless solutions could then be multiplied by their respective scales to yield the final solutions of the problem. From this observation, it should be apparent that the nondimensional solutions determine the qualitative trends of the fluid behavior while the scales determine the magnitude. To assess the trends of fluid behavior, then, it is necessary to determine what influences the nondimensional solutions.

Clearly, anything that influences the system of nondimensional differential equations will influence the value of the dimensionless solutions. As can be seen, however, the only possible means of influence are through the boundary conditions or the coefficients. Since the boundary conditions have also been nondimensionalized, the only means of affecting them is through the aspect ratios, and these remain constant in the problem at hand. The resulting invariance of the boundary conditions leaves the coefficients as the only remaining influence on the solutions. Since these coefficients alone control the dimensionless solutions, they are the governing parameters of the problem and, hence, the dimensionless groups sought in the present analysis.

To derive the final expressions of these coefficients, it remains only to choose values for the scales they contain. If the pipe diameter, the average injection velocity, and the maximum density difference are chosen to represent L_o, V_o, and $\Delta\rho_o$, then the first of the coefficients

in equation (1.9) is seen to be the reciprocal of the Froude number, Fr. Obviously, since D_* reduces to a value of unity, the second coefficient simply becomes the friction factor, C_f. Re-expressing the coefficients in equation (1.9) in accordance with these results yields

$$\overline{V_{z*}}\frac{\partial \overline{V_{z*}}}{\partial z_*} = \frac{1}{Fr}\Delta\rho_* - C_f 2\overline{V_{z*}}^2 - \frac{1}{r_*}\frac{\partial(r_*\overline{V'_{r*}V'_{z*}})}{\partial r_*} - \frac{1}{r_*}\frac{\partial(\overline{V'_{\theta*}V'_{z*}})}{\partial \theta_*} \tag{1.11}$$

where

$$Fr = \frac{V^2}{g\frac{\Delta\rho}{\rho}D} \tag{1.12}$$

and

$$C_f = \frac{\tau}{\frac{1}{2}\rho V^2} \tag{1.13}$$

The significance of this result is twofold. First, since geometrically similar systems have identical aspect

ratios, they have the same nondimensional boundary conditions as well. As a consequence, the matching of these dimensionless coefficients between geometrically similar systems ensures the equality of their dimensionless solutions. Since geometric similarity may exist between systems of differing size, these parameters provide the basis for scaling data between models and prototypes. This fact will be important in the chapter 2.

In addition to their utility in scaling, these parameters provide the governing effects in the problem. Since the Froude number and the friction factor may be roughly said to express the ratios of inertia to buoyancy and friction to inertia, the analysis shows that inertia, buoyancy, and friction govern the backflow process. Dimensional analysis has therefore revealed the physics of the problem. To gain additional understanding it is necessary to review some previous research.

1.3 Review of the Literature

Having determined the governing forces of the problem, it is next necessary to review some previous research on buoyant penetrations. This research may be divided into the categories of forced and natural flow. In the first category buoyant penetrations intrude against a forced counter flow of injected fluid whose magnitude remains constant. In natural flows, however, penetrations occur

against a buoyancy driven counter flow which may therefore be affected by the presence of the penetrations. In the case of forced flows, the emerging fluid is more properly referred to as a jet while in the case of natural flows it is referred to as a plume. Since reactor injection falls into the former category, the forced flow studies will be presented first.

1.3.1 Forced Flow Studies

In regard to forced flow situations, the injection flow rates against which the penetrations propagate are usually driven by a pump. Because such flow rates are usually quite large, ambient penetrations are seldom a concern. Accordingly, the research in this area is rather sparse.

In what seems to be the first work in this area of research, Jörg and Scorer[3] sought to experimentally study the downward penetration of cold air into chimneys against an upward counter flow of hot gas. In their analysis, however, they studied a dynamically equivalent problem of fresh water penetration against a downward salt water flow. In their work they attempted to experimentally determine both the critical conditions and the subcritical penetration behavior under both laminar and turbulent conditions for low values of buoyancy and a range of pipe diameters. Unfortunately, however, they did not specify the ranges in which their various correlations apply, and therefore only

the trends are significant.

They showed penetration to occur below a critical value of the injection velocity in a random fashion around the periphery of the duct. The observed penetrations were chaotic in nature, rising to their zenith where they persisted momentarily and then broke up. In addition, the penetrations occurred over a range of heights from zero to a maximum value which increased as the injection velocity was reduced.

They supposed that the critical conditions were determined by a balance between buoyancy, which promoted the penetration of ambient fluid, and friction, which carried the invading fluid out. Because the penetrations occurred against the weak part of the velocity profile, the nature of the boundary layer was said to determine the critical conditions. When the velocity profile was flat, and the boundary layer was thin; the critical relationship was of the form

$$Fr = C_1 \tag{1.14}$$

With thick boundary layers, however, the velocity profile was more rounded, and the critical relationship became

$$ReFr = C_2 \tag{1.15}$$

where Re is the Reynolds number in the pipe

$$Re = \frac{VD}{\nu} \tag{1.16}$$

Obviously, flat velocity profiles resisted penetration better than rounded ones.

Wilkinson[4] studied the related problem of buoyant sewage discharge into the ocean. At low injection velocities he observed the downward penetration of dense seawater into the pipe. In his study he confirmed the observations of Jörg and Scorer[3] that the velocity profile affects the critical conditions. He found that when the discharge passed through an orifice, the critical Froude number was reduced by a factor of two in comparison to discharge through a nozzle. When the experiments were repeated on different sized systems, however, he found the critical Froude number to be insensitive to the effects of scale.

In addition, Wilkinson seems to be the only author to have studied the effect of the injection angle on the penetration behavior. He observed that as the injection angle departed from the vertical, the critical Froude number increased, and the intrusion behaved less like a plume. Additionally, the penetration depth increased for constant Froude numbers, and beyond a certain angle the penetration

became stabilized against the lower wall of the pipe.

These effects may be explained in terms of the fluid behavior at the interface. As the injection becomes more horizontal, the increasing component of the buoyant force perpendicular to the interface begins to suppress the instabilities which cause the turbulent exchange. As the turbulent exchange decreases, both the interfacial friction and mixing decrease, promoting increased penetration and stability.

With regard to reactor injection systems, the effect of buoyant backflow was first noticed by Theofanous[5] while performing reactor flow experiments on a 1/2 scale model. Theofanous was trying to determine how the HPI flow would mix in the reactor cold leg and downcomer under the conditions of loop stagnation. In this investigation he was trying to determine whether the resulting flow would be stratified or mixed in order to evaluate the potential for pressurized thermal shock (PTS). Since PTS is increased for stratified flows, Theofanous perceived the backflow phenomena as beneficial due to the increased mixing resulting from it. In his study he observed backflow to occur below injection Froude numbers of .5. Since this was not the focus of his study, however, he had little else to say about this subject.

1.3.2 Natural Flow Studies

Although the research on forced flows is sparse, a greater contribution comes from natural flow studies. These studies which focus on the flow characteristics of cooling towers were undertaken to determine the effects of cold inflow on the cooling tower draft. Since this effect is factored into the cooling tower studies, a short description will be provided here.

The natural draft which drives certain cooling tower flows results from the partial isolation of the internal warm air from the ambient. Since this isolation causes the pressure gradient within the tower to differ from the ambient, a potential is created to drive the flow. Obviously, this potential increases with tower height. When cold air penetrates into the top of the tower, however, the effective draft height is reduced, diminishing the exit velocity and increasing the depth of penetration. The tendency of ambient intrusions to propagate themselves by reducing the counter flow is peculiar to natural flows and is not a factor in reactor injection systems. This fact should be remembered in reviewing the cooling tower literature.

In the following review a study which describes the effect of cross wind on buoyant penetrations will be briefly mentioned. This will be done to identify effects that may be significant in future reactor studies, where cross flow

in the cold leg is added to the analysis.

In studying the behavior of cooling tower plumes, Ernst[6] measured the temperatures at eleven points inside the top of a cooling tower. As a result of these measurements, he observed the unsteadiness of the upward air flow and the downward intrusion of cold ambient air. He also noticed that through the bending of the cooling tower plume, a cross wind could cause ambient intrusions by forcing the plume to prematurely separate from the upwind lip of the tower. However, although he noted the effect of wind, he carefully distinguished between cold inflow which essentially results from buoyant instabilities and wind induced separation which is not a buoyant effect.

After making this distinction, he then described the complicated manner in which these two phenomena interact. He observed that at low to no wind velocity cold air entered the top of the cooling tower in a steady fashion. As the wind velocity increased, however, the penetrations became unsteady causing the warm outflow to take on a puffing character. At high wind velocities a steady vortex of cold air became established at the wind side of the cooling tower creating a region of low pressure at the tower exit, and suppressing cold inflow. The work of Ernst was extended by his student, Baer[7], and also by Moore and Torrance[8].

Since it was observed that inflow occurred in the absence of wind, it was believed that the problem of cold inflow could be decoupled from the problem of wind induced

separation. For this reason several authors studied the problem of cooling tower flows in stagnant ambient environments. Moore[9],[10] studied the behavior of cooling tower plumes under these conditions and noted that when the exit velocity was low, the plume assumed an hour glass shape in which the initial convergence was caused by buoyant acceleration and the subsequent divergence by turbulent entrainment. As a result of this observation, he reasoned that severe convergence would cause the plume to "fall in" the tower, resulting in an annular intrusion between the cooling tower wall and the boundary of the "fallen in plume".

The first step in his analysis, then, was to determine the conditions necessary for convergence. By including the effects of buoyancy and turbulent entrainment, he discovered that convergence would occur if

$$F = \epsilon Fr < \frac{1}{8} \tag{1.17}$$

In his expression the inflow parameter, F, was equal to the product of the turbulent entrainment coefficient, ϵ, and the Froude number. Since plume convergence was not a sufficient condition for cold inflow, he next sought to determine the depth of penetration through a mass balance on the inflow region.

In this analysis he noted that the plume would penetrate until the inflow of mass over the cooling tower lip was balanced by entrainment losses at the interface. In this balance the incoming mass flow rate was dependent on the exit gap width between the tower wall and the plume boundary. The entrainment, on the other hand, was proportional to the interfacial area between the plume and the inflow region. As the depth of penetration increased, it was shown that beyond a certain point the divergent section of the plume would also "fall in" the tower, narrowing the gap at the exit. Since this narrowing limited the incoming mass flow rate, a maximum penetration depth could be determined beyond which the assumed entrainment rate could not be maintained. By varying the tower parameters, this maximum penetration depth was presented as function of the exit velocity and the slenderness of the tower.

Dayal[11] expanded Moore's results in two ways. First, he relaxed an assumption made by Moore that the inflow velocity was constant within the penetration. In addition, he extended Moore's analysis of annular intrusions to fingerlike intrusions which are more common in practice. By varying the cross-sectional shape of these intrusions, he demonstrated that the penetration depth was fairly insensitive to the penetration shape.

Wynne[12] attempted to experimentally characterize the effects of cold inflow in terms of reductions in the

effective tower height and also in terms of head loss. However, since most of his work is devoted to analyzing the fitness of a model cooling tower, it provides little insight into the penetration behavior itself.

In a three part study Modi[13] investigated the cooling tower problem under the peculiar conditions of a forced laminar airflow. (For this reason Modi's research should technically be included under the discussion of forced flows, but since it is cooling tower related, it is mentioned here.) In an experimental study he directly observed the penetration behavior and noticed the formation of interfacial instability waves near the critical conditions. He next performed a numerical analysis in which he showed the penetration depth to vary with the Grashof number in the low Reynolds number range. Finally, through a theoretical analysis, he illustrated several effects caused by the low velocity convergence of the emerging flow. He stated that due to the elliptic nature of the Navier-Stokes equations, the convergence caused the bending of initially straight streamlines within the duct. He also noted that in the bending process, the wall retained its identity as a streamline. Since the wall could not bend, however, the distance between streamlines increased near the wall as the exit was approached. As a consequence, the fluid decelerated near the wall, increasing its vulnerability to penetration.

1.4 General Procedure

As a result of the previous development, the main parameters governing the backflow process have been identified. In addition, valuable insight has been gained from the previous experience of several authors. Significant in this regard is the observation that the penetration behavior is sensitive to the velocity profile in the pipe[3],[4] and, hence, the problem geometry. Because the effect of reactor geometry has not yet been thoroughly studied, it is necessary to go beyond the previous research. For this reason a combined experimental and theoretical analysis was undertaken to investigate the backflow behavior. This study will now be briefly outlined.

The discussion in Chapter 2 will center around the experimental portion of this research which involved reactor flow experiments in a 1/5 scale model. In discussing this research, scaling criteria will first be used to show that the model adequately simulated full scale behavior. Following this discussion, the experimental facility, instrumentation, and procedure will next be thoroughly described. Finally, the experimental results will be discussed and presented in tables which give the penetration depth as functions of the fluid fractional density difference, $\Delta\rho/\rho$, and the injection velocity. From these tables the critical velocity will be determined as the value for which the penetration depth is zero.

The experimental results obtained in chapter 2 will then be theoretically derived in chapter 3. First, several assumptions will be made to reduce the problem to analytical proportions. Next, the critical conditions will be derived by balancing the friction and buoyancy forces on intruding plumes. Finally, through simple considerations of mass conservation, the penetration depth will be predicted. In all cases the theoretical relationships will be derived in terms of experimental proportionality constants and matched to the experimental data. To verify the analysis, a comparison between experiment and theory will then be made.

Following this comparison, the results of chapters 2 and 3 will be extended to full scale systems in chapter 4. Finally, the major conclusions of this study will be summarized along with several suggestions for future research in chapter 5.

CHAPTER 2

EXPERIMENTAL ANALYSIS

2.1 Introduction

As a consequence of geometric sensitivities, a proper analysis of buoyant backflow must include an experimental study in a reactor geometry. For this reason reactor flow experiments were conducted in a 1/5 scale model of a reactor HPI, cold leg, and downcomer. The purpose of these experiments was to empirically determine the penetration behavior for turbulent injection flow rates in a stagnant loop. More specifically, the experiments were designed to evaluate the dependence of both the critical conditions and the subcritical penetration depth on the injection velocity and the density difference between the two fluids. The description of these experiments is the purpose of the present chapter.

To describe the experimental research the following discussion will involve several related topics. First, scaling analysis will be used to show that the experimental facility adequately simulated the full scale behavior of a nuclear reactor. Following this discussion, the experimental facility, instrumentation, and procedure will be thoroughly described. Finally, the experimental results themselves will be presented along with several qualitative observations. At

this time trends observed in the data will be described.

2.2 Scaling Analysis

Before describing the experimental model, it is necessary to show that the results obtained adequately reflect full scale behavior. To this end it was mentioned in section 1.2 that under turbulent injection conditions the backflow process is governed by the Froude number and the friction factor. It was also mentioned that under the additional conditions of geometric similarity, these two parameters form the basis for scaling experimental results between different sized systems. For the model data to represent full scale behavior, then, it is necessary to maintain turbulent flows in each system ($Re_{HPI} \geq 2300$) and to match these parameters.

To show the suitability of the model, the following analysis will compare the values of the model scaling parameters with the full scale values that would occur during a SBLOCA. In this analysis the full scale behavior assumed will be that of the Trojan nuclear power plant, henceforth referred to as the prototype. In comparing these two systems, the following discussion will consist of four stages. First, some additional implications of the scaling criteria will be discussed to refine the basis for comparison. Next, the scaling parameters will be evaluated for the prototype. Following this, a similar evaluation will be performed for the model. Finally, the two results will be compared.

2.2.1 Scaling Criteria

To analyze the scaling criteria imposed by dimensional analysis, it must be realized that the friction factor match necessarily implies a Reynolds number match as well. Unfortunately, however, at reduced scale the Froude and Reynolds number relationships place divergent demands on the experimental model, making it impossible to satisfy both criteria simultaneously. For this reason it is necessary to sacrifice either the Froude number or the friction factor relationship. Since the backflow penetrations are driven by buoyancy, it would seem on intuitive grounds that the friction factor relationship is the one to sacrifice. This may be shown by a simple analysis.

To prove this result it is necessary to compare the main forces on the plume with the wall friction represented by friction factor. When backflow occurs, the main forces on the penetrations are an upward buoyancy force and a downward shear stress at the interface. Since the penetrations rise, it is clear that buoyancy exceeds the interfacial friction. However, as a consequence of the greater interfacial roughness and the increased turbulent exchange, the interfacial friction greatly exceeds the friction at the walls. Since the wall friction must therefore be negligible in comparison to buoyancy as well, the friction factor relationship may be safely eliminated.

As a consequence of this analysis, it is clear that

turbulent backflow behavior may be modeled at reduced scale by preserving the Froude number only. To this end Froude numbers will be computed for the prototype and the model separately as a basis for future comparison. In addition, the Reynolds numbers will also be computed to determine the state of turbulence in each system. In these computations the prototype will be considered first.

2.2.2 Full Scale Analysis

To evaluate the scaling parameters associated with a SBLOCA, it is first necessary to determine the fluid conditions resulting from such a transient. To facilitate this discussion, Figure 2.1, which was taken from the FSAR of the Trojan nuclear power plant[14], shows the timewise variation of the reactor system pressure following an assumed three inch break. As can be seen from the figure, the system pressure drops rapidly in the first few minutes following the break and then levels off momentarily. After remaining constant for several minutes, the pressure again drops, albeit gradually, throughout the rest of the transient. Since these trends are important in obtaining the fluid behavior, they will be briefly discussed.

Because the reactor pressure is 2300 psi before the break, the initial rate of leakage is necessarily large, causing a rapid reduction in system pressure. When the system pressure falls below about 1500 psi, however, high pressure

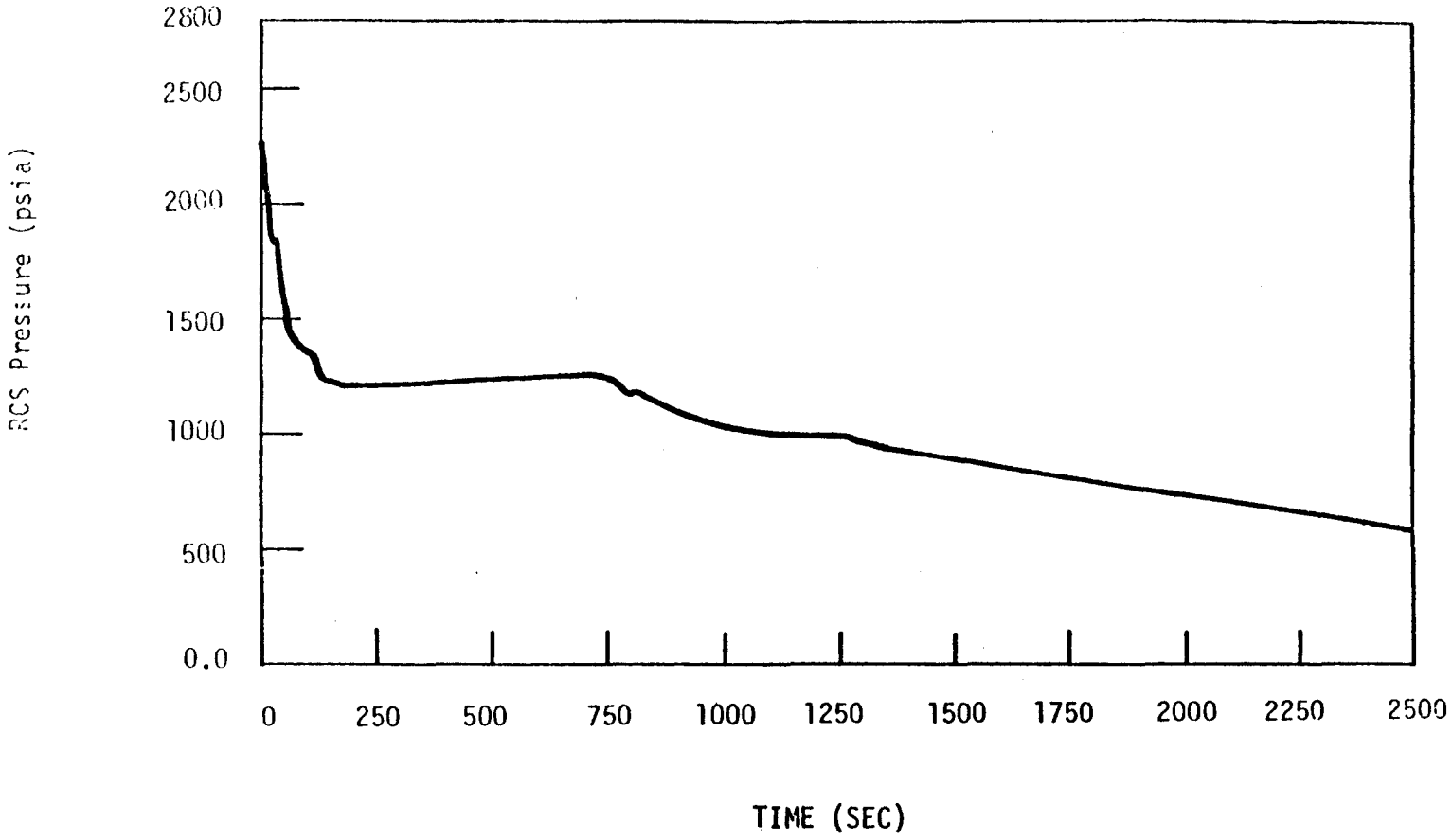

Figure 2.1 Timewise Pressure Variation for Trojan Nuclear Power Plant Following an Assumed Three Inch Break.

injection is initiated. As the system pressure continues to drop, the increased driving head magnifies the injection flow rate as shown in Table 2.1[15]. However, in contrast to the injection flow rate, the rate of leakage decreases as the pressure is reduced. Since these two flow rates have opposite tendencies, a steady state is eventually achieved where the conservation of system mass produces a temporary stabilization of pressure. Beyond this plateau region, however, the cooling effect of the injected fluid becomes significant, causing the system pressure to slowly drop throughout the remainder of the transient.

Since the injection Reynolds and Froude numbers depend on fluid properties, it is necessary to determine the temperature behavior of the injected and ambient fluids throughout the transient. For most PWRs the injection temperature, T_i, remains constant at 68 °F (room temperature) and the ambient cold leg temperature, T_a, is initially 540 °F[16]. Since the saturation pressure corresponding to the cold leg temperature is 961 psi, it is clear that the ambient fluid remains liquid throughout the initial pressure drop. In addition, because the effects of cooling are not yet significant, the ambient fluid may be assumed to remain at 540 °F during this phase of the transient. Furthermore, since the final pressure reductions result from cooling, the ambient fluid may be assumed to remain liquid during the final phase of the transient as well. As a consequence of this cooling, for pressures below 961 psi, ambient temperatures may be

approximated by the saturation temperature corresponding to the prevailing system pressure. As a result of these assumptions, the ambient temperatures may be evaluated throughout the transient.

Table 2.1 Injection Flow Rates vs. System Pressure for Trojan Nuclear Power Plant.

RCS Pressure (psig)	Injection Flow Rate (gpm)
1468.0	0.0
1400.0	78.4
1300.0	183.4
1200.0	273.0
1100.0	341.8
1000.0	403.7
900.0	454.8
800.0	501.4
700.0	546.9
600.0	588.3
500.0	622.1
400.0	657.6
300.0	691.9
200.0	723.6
100.0	752.7
0.0	781.2

With both the injection and ambient temperatures known, the density difference between the two fluids may now be computed. In addition, the injection viscosity may be determined from the injection temperature. To calculate the Froude and Reynolds numbers, it is simply necessary to obtain

the HPI diameter and the pressure-velocity relationship for the plant injection system. For the Trojan nuclear power plant, the HPI diameter is 8.75 inches (22.23 cm) and the pressure-velocity relationship is given in Table 2.1. By using this information, the characteristics of the injection process may be evaluated as functions of the system pressure as shown in Table 2.2.

In these calculations it was decided to evaluate the injection Reynolds and Froude numbers over a complete range of reactor system pressures since the pressure appears to still be dropping at 2500 s in Figure 2.1. As a consequence, Table 2.2 gives the complete range of injection parameters possible during this transient. These values will therefore serve as the basis of comparison for the model.

2.2.3 Model Analysis

To evaluate the flow characteristics of the model, it is necessary to understand the experimental approach. Since the purpose of the experiments was to determine the penetration behavior as a function of the injection velocity and density difference (buoyancy), these two parameters were independently varied over wide ranges to test the effect of each. The value of the scaling parameters was therefore dependent on how these ranges were determined.

The range of density variations was determined by material constraints in the model. To prevent the cracking of

glass, it was decided to use salt rather than heat to generate the density differences. Because this choice limited the maximum obtainable fractional density difference, $\Delta\rho/\rho$, to .16, it was decided to determine the effect of buoyancy by varying $\Delta\rho/\rho$ over the fullest possible range of values. Accordingly, $\Delta\rho/\rho$ was varied over the range, (.02-.16), in increments of .02.

Table 2.2 Injection Characteristics as Functions of System Pressure for Trojan Nuclear Power Plant.

P(psi)	T_i°F	T_a°F	$\Delta\rho/\rho$	V(cm/s)	Re	Fr
1400.	68	540	.248	3.19	7057	.0019
1300.	68	540	.248	7.46	16509	.0103
1200.	68	540	.248	12.74	28201	.0301
1100.	68	540	.248	13.90	30769	.0358
1000.	68	540	.248	16.41	36341	.0499
900.	68	532	.244	18.49	40941	.0643
800.	68	518	.231	20.39	45136	.0827
700.	68	503	.217	22.24	49231	.1045
600.	68	486	.203	23.92	52958	.1297
500.	68	467	.187	25.29	56001	.1568
400.	68	445	.170	26.74	59197	.1930
300.	68	417	.151	28.13	62284	.2409
200.	68	382	.127	29.42	65138	.3123
100.	68	328	.095	30.60	67757	.4513
14.	68	212	.040	31.76	70323	1.1557

Once a particular value of $\Delta\rho/\rho$ was chosen, the allowable velocity range was determined from this value. First, the effect of salt on the injection viscosity was determined from

the CRC Handbook of Chemistry and Physics[17]. Using the updated value of the injection viscosity together with the model injection diameter, 2 in. (5.08 cm), the minimum injection velocity was then determined from the requirement that the flow be turbulent ($Re \geq 2300$) in the injection line. Using this velocity, the minimum Froude number was also calculated. The maximum velocity (28 cm/s), on the other hand, was obtained from the maximum capacity of the pump (9 gpm). This value was then used with the other parameters to calculate the maximum Reynolds and Froude numbers.

By reiterating this procedure for each value of $\Delta\rho/\rho$, the complete range of model parameters was determined as shown in Table 2.3. In this table the subscripts, l and h, are used to denote quantities at the low and high ends of the allowed velocity range for each value of $\Delta\rho/\rho$. As a result of these calculations, it is now possible to compare the two systems.

Table 2.3 Injection Characteristics as Functions of $\Delta\rho/\rho$ for the Model

$\Delta\rho/\rho$	ν/ν_o	$V_l$cm/s	Re_l	Fr_l	$V_h$cm/s	Re_h	Fr_h
.02	1.03	4.68	2300	.220	28.0	13812	7.88
.04	1.05	4.79	2300	.115	28.0	13454	3.94
.06	1.09	4.95	2300	.082	28.0	12992	2.63
.08	1.15	5.21	2300	.068	28.0	12371	1.97
.10	1.22	5.53	2300	.061	28.0	11654	1.58
.12	1.29	5.89	2300	.058	28.0	10933	1.31
.14	1.42	6.46	2300	.060	28.0	9975	1.13
.16	1.59	7.23	2300	.066	28.0	8913	.99

2.2.4 Comparison of Systems

From the information presented in Tables 2.2 and 2.3, the injection flow rates are seen to be turbulent in both systems. In addition, the Froude numbers obtainable in the model matched those in the Trojan plant over a significant portion of the transient. For the portion of the transient unobtainable in the model, however, conclusions can still be made. For example, since the full scale Froude numbers are extremely low in this region, the presence of backflow in the model would imply subcritical conditions in this portion of the transient. In addition to the Trojan plant, the Calvert Cliffs and H. B. Robinson plants produce injection Froude numbers of .4 and .6 respectively at 1000 psi [5]. Since these Froude numbers lie within the model range, the data obtained in the model would adequately represent these plants as well. With the assurance that the model data is be relevant, the experimental facility may now be discussed.

2.3 Experimental Facility

To simulate reactor flow conditions a 1/5 scale model of a reactor HPI, cold leg, and downcomer was constructed as shown in Figure 2.2. As can be seen from the figure, the complete facility consisted of the following:

1. A supply tank to contain dense fluid
2. A centrifugal pump to drive the flow with a maximum flow rate of 9 gpm.
3. A throttle valve to control the flow rate
4. A factory calibrated turbine flow meter to measure the flow rate
5. Two paddle wheel flow sensors for the same purpose
6. A pyrex test section to simulate reactor flow behavior
7. A discharge tank into which the fluid drained
8. Interconnecting piping to transfer fluid between the previous components

The flow path can be described in reference to figure 2.2. In normal operation salt water was drawn from the supply tank through the pump and driven past the throttle valve and factory calibrated flow meter. Next, it traveled past the paddle wheel flow sensor, and through the 90° injection line from which it entered the cold leg. As it left the cold leg, it passed through the downcomer and then the overflow line, emptying into the discharge tank.

As can be seen from figure 2.3, the main test section consisted of the HPI and cold leg which formed a tee junction. In addition, a 45° injection line was added to this section to test the angular dependence of backflow in separate experiments. The cold leg and the two injection lines formed a single structural unit composed of pyrex glass for the purposes of flow visualization. Because special manufacturing would have been required to make the dimensions exactly 1/5 scale, the scaling requirements were relaxed slightly to take advantage of large cost savings. In spite of this fact, however, the model dimensions came very close to being 1/5 scale as can be seen from Table 2.4.

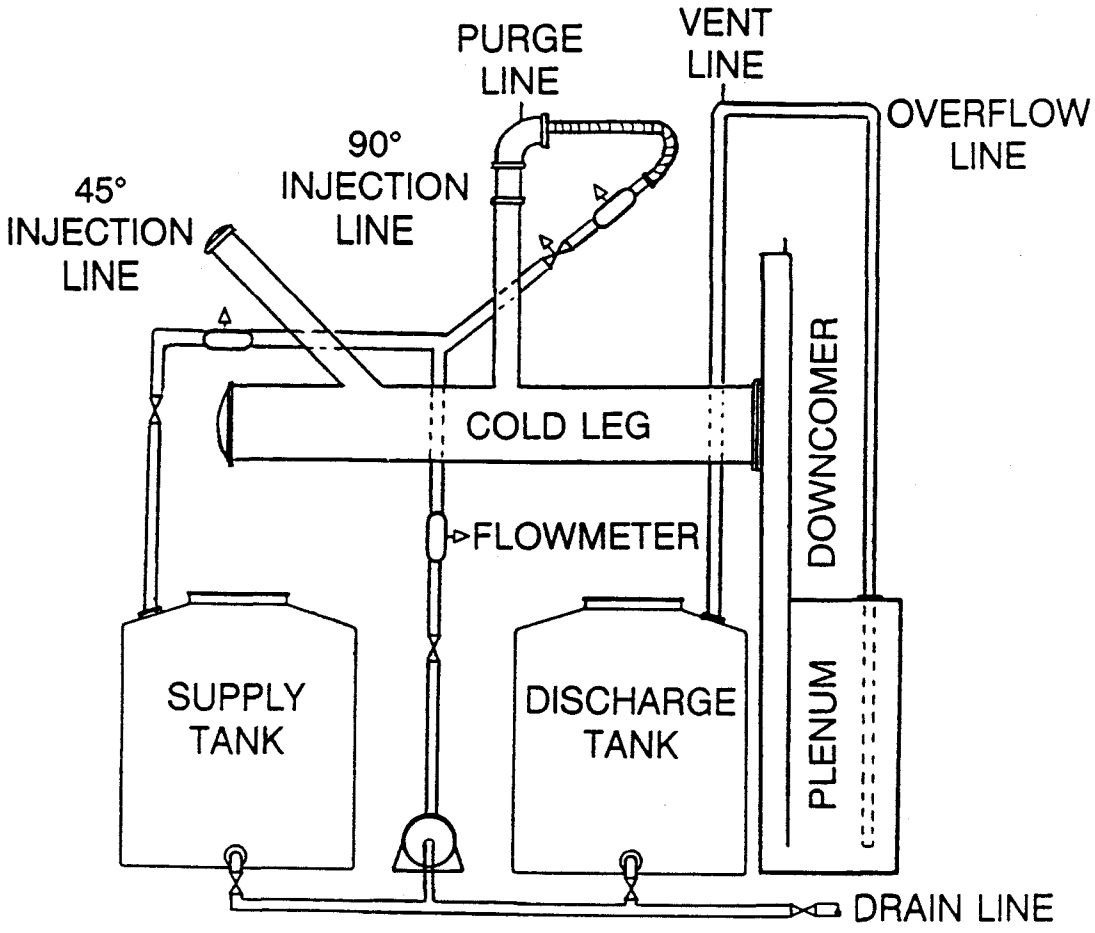

Figure 2.2 Schematic of 1/5 Scale Facility Used to Measure Plume Heights in a Vertical Injection Line.

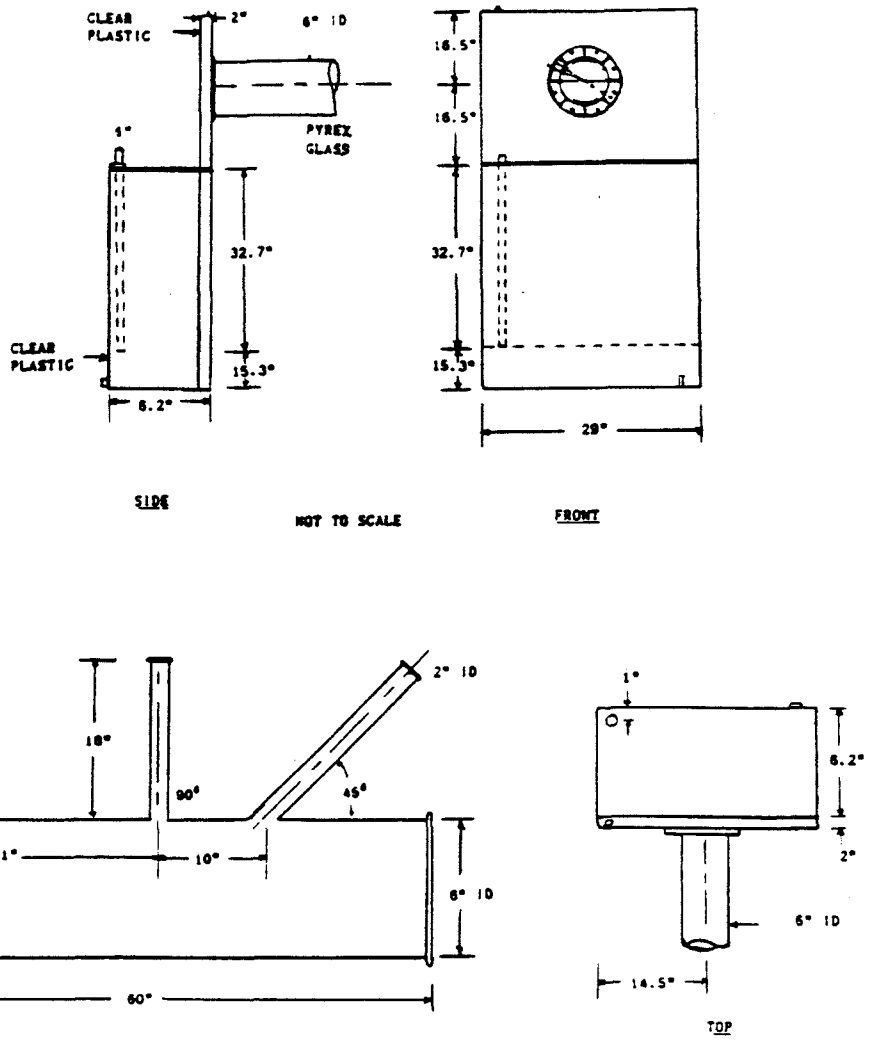

Figure 2.3 Significant Dimensions of the Main Test Section.

In order to sample the ambient density, a port was provided at the junction of the HPI and the cold leg. The fluid samples were taken by means of a long, unobtrusive needle inserted into the port and bent through an angle of 180°. The immediate 180° bend in the needle prevented disturbances in the injection flow rate and caused the density samples to be taken away from the injector in the uppermost region of the cold leg. By providing a considerable distance between the injector and the point of measurement, the needle guaranteed that the density samples taken were unaffected by the injection flow.

Table 2.4 Comparison of the Model Dimensions to Full Scale in Inches.

Component	Full Scale	1/5 Scale	Model
HPI I.D.	8.8	1.8	2.0
Cold Leg I.D.	27.5	5.5	6.0
Downcomer Gap	10.0	2.0	2.0
Core Barrel	260.7	52.1	66.0
Cold Leg Length	232.5	46.5	60.0

2.4 Instrumentation and Measurement

Closely related to the discussion of the experimental facility is the discussion of the means used to collect the data. Since the experiment was simply designed to measure the penetration depth for various density differences and

injection velocities, the following discussion will describe the measurement of these three quantities.

To obtain the density differences between the fluids, the densities of each fluid were measured separately. To determine these densities, 200 ml of each fluid was first measured by using a previously weighed volumetric flask. Since the volume of the fluid could be determined to within .1 ml, the measurement uncertainty was less than .05%. The 200 ml of fluid was next weighed on a Mettler electronic balance which automatically subtracted the mass of the flask. Since the scale was accurate to .01 g, the fluid mass could be determined to within .005%. As a consequence of the extreme accuracy of these measurements, the maximum uncertainties for ρ, $\Delta\rho$, and $\Delta\rho/\rho$ were calculated to be .05%, 4.2%, and 4.2%, respectively.

With regard to the injection velocity, the injection flow rates were measured by means of an Omega FP 5300 paddle wheel flow sensor connected to a high speed Keithly data acquisition system. (It should be mentioned here that although the discussion usually centers around the injection velocity, the parameter directly measured was the injection flow rate.) To calibrate the flow meter its voltage output was converted to a computer channel number and compared to the injection flow rate over a wide range of values. To obtain these flow rates initially, the flow into the discharge tank was measured by means of a 4 liter beaker and a stop watch. To minimize the human errors inherent in this process, the measurements were

repeated several times for each flow rate and then averaged. When these flow rates were compared to the output of the sensor, a linear response was observed above 2 gpm as shown in figure 2.4. This response was then quantified to calibrate the meter within its linear range. As guaranteed by the manufacturer, the accuracy of the meter was 1% of the full scale velocity after calibration. Since the maximum possible flow rate was less than 10 gpm, the calibration uncertainty for the velocities was less than .1 gpm (.31 cm/s).

For flow tests within the linear range of the meter, the flow rates were determined by the meter and directly fed into a computer. As the flow rates were observed on the computer screen, they were seen to fluctuate about their mean value. As determined from the computer data, the standard deviations of these fluctuations were less than .1 gpm (.31 cm/s). By combining the calibration and fluctuation uncertainties, the maximum uncertainty for the injection flow rate was determined to be less than .15 gpm (.47 cm/s) above 2 gpm.

For tests below the linear range of the meter, the flow rates were obtained by direct measurement with a beaker and stop watch. Concerning these tests, the accuracy of the direct flow measurement was determined from the series of low flow measurements undertaken to obtain the calibration curve. When these measurements were taken, the flow rate varied between 1.74 and 1.84 gpm over a series of 10 measurements with a standard deviation of .015 gpm (.047 cm/s). These values were therefore taken as the uncertainties for flow

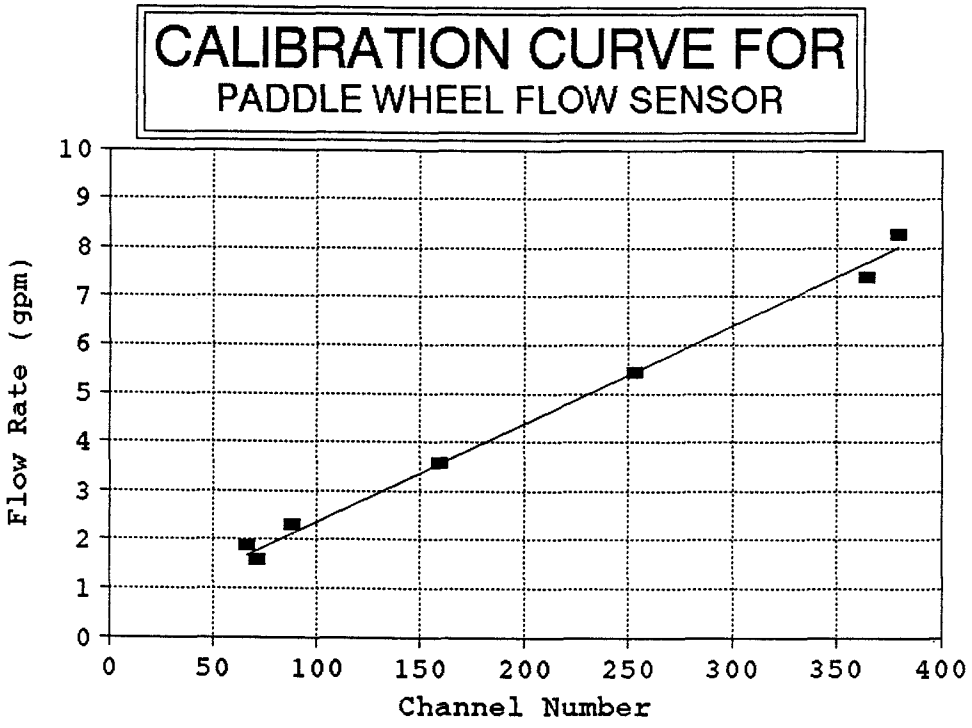

Figure 2.4 Calibration Curve for the Omega FP 5300 Paddle Wheel Flow Sensor

rates below 2 gpm.

Finally, with respect to the penetration depth, it was necessary to provide a means of detection prior to measurement. For this reason the backflow penetrations were made visible by coloring the ambient fluid with a green fluorescent dye. Since the injected solution contained no dye, it remained clear. The backflow penetrations could then be seen in the HPI as green plumes of ambient fluid penetrated against the clear downflow. To accentuate these penetrations the tests were run in darkness against a black back drop, using an ultraviolet light to increase the brightness of the plumes.

To determine the height of these plumes, a meter stick was attached to the HPI line. Because the tests were run in darkness, the stick was made visible by illuminating the centimeter divisions with a fluorescent paint. Since the smallest visible division of the scale was 1 cm, the uncertainty of the backflow heights was taken as .5 cm. To minimize the observation errors, the penetration behavior was video recorded so that the heights could be determined at reduced speed.

2.5 Experimental Procedure

Having described the experimental facility and the methods used to obtain the data, it remains to describe the procedure in which they were used. As mentioned previously,

the purpose of the experimental research was to determine the effects of buoyancy and injection velocity on the penetration behavior. To this end the experimental data was obtained by running a series of tests on the experimental facility shown in Figure 2.2. During each test, the control parameters were held constant to allow sufficient time to observe the backflow behavior and to eliminate potential transients. Because the injection occurred in a finite volume, however, it was thought that the mixing of the two fluids might reduce the buoyancy between them. Since initial tests showed this effect to be negligible for the first minute, variations in the buoyancy were avoided by limiting the tests to this amount of time.

Although the control parameters were effectively held constant during each test, they were systematically varied between the tests to isolate the effect of each on the penetration behavior. With respect to the variations in buoyancy, it was mentioned previously that material constraints dictated the use of salt to generate the density differences. Since this choice limited the maximum fractional density difference, $\Delta\rho/\rho$, to .16, the effect of buoyancy was determined by varying $\Delta\rho/\rho$ over the range, (.02-.16), in increments of .02. For each of the resulting eight cases, the desired value of $\Delta\rho/\rho$ was initially set by mixing a salt solution in the supply tank and flooding the rest of the system with fresh water containing the green fluorescent dye.

While $\Delta\rho/\rho$ was held constant, a series of one minute, constant velocity tests was run, beginning with a low velocity

for the first test and increasing it for each subsequent test. Since the salt solution contained no dye, backflow could be seen as green plumes of ambient fluid penetrated against the injected salt solution. As the test velocity was steadily increased, the maximum height of these plumes decreased until a point was reached beyond which backflow no longer occurred. Since it was surmised that the critical velocity lay between this and the previous value, additional tests were then conducted within this velocity range to determine the critical value more precisely.

Once the critical velocity was determined, a new value of $\Delta\rho/\rho$ was chosen. This value was again held constant for another series of one minute, constant velocity tests, beginning, as mentioned previously, with a low velocity. By continuing this systematic variation of the control parameters, both the critical velocity and the subcritical penetration behavior were obtained for each value of $\Delta\rho/\rho$.

2.6 Experimental Results

By watching the video recordings of these tests, the penetration behavior was closely observed. The penetrations were seen to be chaotic in nature, rising to their zenith where they persisted momentarily and then suddenly broke up. With decreasing injection velocities, the penetrations became deeper, more concentrated, and longer lasting. In reference to the cold leg, the penetrations occurred almost exclusively

at the upstream and downstream portions of the HPI. This result, which conflicts with the uniform penetration observed by other researchers, was most likely an effect of the asymmetric geometry.

By recording the height of each penetration, the results of the one minute tests were plotted as histograms of height vs. number of occurrences. These plots are contained in Appendix 2. From these histograms two experimental trends were evident. First, the penetrations occurred over a range of heights from zero to a maximum value which increased as the injection velocity was reduced. Second, the range of heights over which the plumes occurred also increased as the injection velocity was reduced.

Since the maximum penetration depth was the most significant parameter, the maximum heights from Appendix 2 have been presented as functions of the injection velocity and $\Delta\rho/\rho$ in Tables 2.5 and 2.6. As a result of the data in these tables, it can be seen that backflow began below a critical value of the injection velocity and that this value increased with buoyancy. Obviously, since the height vanished at the critical velocity, there are no histograms in Appendix 2 corresponding to the critical cases. By looking across the rows in Tables 2.5 and 2.6, the same trends observed for decreasing injection velocity may be observed for increasing $\Delta\rho/\rho$. Unfortunately, however, since precise control of the injection velocity was impossible, the velocities vary across any given row, allowing these trends to be only roughly

observed.

It may be observed by comparison with Table 2.3 that the low injection velocities in Table 2.6 were less than the minimum values deemed necessary for turbulent flow. However, once the penetration entered the pipe, the effective velocity was increased by its presence. Because of this increase, turbulent conditions were induced in the pipe as was evident from the behavior of the plumes.

Table 2.5 Backflow Heights as Functions of Experimental Parameters for $\Delta\rho/\rho \leq .08$. Heights are in Centimeters and Velocities in Centimeters per Second.

$\Delta\rho/\rho$ = .02		$\Delta\rho/\rho$ = .04		$\Delta\rho/\rho$ = .06		$\Delta\rho/\rho$ = .08	
V	h	V	h	V	h	V	h
4.73	11.0	5.51	12.0	5.02	20.0	5.31	20.0
6.02	8.0	7.87	8.0	7.82	11.0	7.76	15.0
7.76	5.0	9.34	5.0	9.21	8.0	9.32	11.0
8.57	4.0	11.05	5.0	10.98	7.0	10.89	7.0
9.77	3.0	11.61	3.5	12.67	5.0	12.58	5.0
10.81	0.0	12.60	0.0	13.36	3.0	14.10	4.0
				13.92	2.0	14.49	4.0
				14.91	0.0	14.73	4.0
						14.84	3.0
						15.01	2.0
						16.22	0.0

In addition to kinematic trends, information regarding the plume dynamics was also obtained from the experiments. As shown in Figure 1.1, the plumes were seen to consist of a thin

core region near the wall in which the dye was concentrated and a thick outer region that was more dilute. Since the plumes penetrated near the wall, it was concluded that the buoyancy in the core was large, providing the driving force for penetration and consequently a positive velocity. Experiments showed this area to remain essentially constant with height. The outer region, on the other hand, was more dilute and characterized by turbulent eddies. For

Table 2.6 Backflow Heights as Functions of Experimental Parameters for $\Delta\rho/\rho \geq .10$. Heights are in Centimeters and Velocities in centimeters Per Second.

$\Delta\rho/\rho$ = .10		$\Delta\rho/\rho$ = .12		$\Delta\rho/\rho$ = .14		$\Delta\rho/\rho$ = .16	
V	h	V	h	V	h	V	h
5.00	23.0	5.43	18.0	5.29	22.0	4.71	27.0
7.83	14.0	7.54	15.0	8.56	16.0	9.45	15.0
9.51	12.0	9.05	13.0	10.15	13.0	10.58	13.0
11.11	10.0	11.37	9.0	12.25	12.0	12.45	12.0
12.69	7.0	12.37	8.0	12.97	8.5	13.89	10.0
14.09	5.0	14.47	6.5	14.00	6.0	15.33	7.0
15.61	3.5	15.42	4.0	15.31	6.5	16.99	4.5
15.67	3.0	16.30	3.5	18.57	4.0	18.24	5.0
16.40	3.0	16.41	4.0	19.36	4.0	18.78	4.5
17.22	2.0	17.31	4.0	21.04	0.0	19.46	3.0
17.80	0.0	17.49	3.0			20.05	3.5
		17.97	3.0			21.84	0.0
		18.36	1.5				
		19.15	0.0				

this reason it was assumed to consist of well mixed fluid entrained from the core. Since its buoyancy was considerably reduced, the fluid in this region could not advance against the injection flow and was consequently dragged downward by the injection fluid. The velocity in this region was therefore negative.

As these examples clearly show, the nature of the backflow process was revealed in the experiments. As a result of this research, the gross characteristics of penetration were described, and several anticipated trends were qualitatively confirmed. In addition, insight into the dynamics of penetration was gained from close observation. Although the experimental data provides a great deal of factual information, it provides little insight into the inter-relationships involved. To systematize these observations, a theoretical analysis is required.

CHAPTER 3

THEORETICAL ANALYSIS

3.1 Introduction

A complete analysis of the buoyant plume would necessitate the solution of three conservation equations plus three additional relations to determine the velocity fields, concentration profiles, and the plume cross-sectional area as functions of both time and spatial coordinates. Such an analysis would be quite involved and would require a detailed computer code for its completion. Because this type of analysis depends upon the correct identification of the relevant physical processes, it makes more sense to seek an analytical solution first. It is to these ends that the present discussion is directed.

To obtain an analytical solution, the following analysis will consist of three stages. First, several assumptions regarding the nature of the plume will be made to reduce the problem to analytical proportions. Next, the critical velocity will be determined as a function of the fluid fractional density difference. Finally, the relationship between the penetration depth and the injection velocity will be determined for subcritical velocities.

3.2 Basic Assumptions

As mentioned previously, the plume rises to a quasi-steady maximum height where it persists momentarily before chaotically breaking up. A plume in this state consists of a thin core region near the wall and a thick outer region as shown in Figure 3.1a. The core is the active portion which has a positive velocity and, hence, drives the plume. The outer region, on the other hand, is the passive portion consisting of well mixed fluid entrained by the downflow and consequently having a negative velocity. Since the well mixed outer region is obviously more dilute than the core, the outer region will be assumed to have the same density as the injected fluid and consequently to move at the same velocity. This assumption is equivalent to eliminating the outer region and reducing the problem to that shown in Figure 3.1b. All subsequent analysis will therefore focus on the core region only.

Having eliminated the outer region, the pipe cross-section will be assumed to consist of the cross-sectional areas of the core, A_L, and the downflow region, A_H. These areas will border each other along an interface of lateral dimension, f, as shown in Figure 3.2. (It should be mentioned here that in these and future designations the subscripts L and H will represent quantities associated with the light and heavy fluids in the plume and downflow regions, respectively.) Since the experiments showed A_L to be fairly constant with

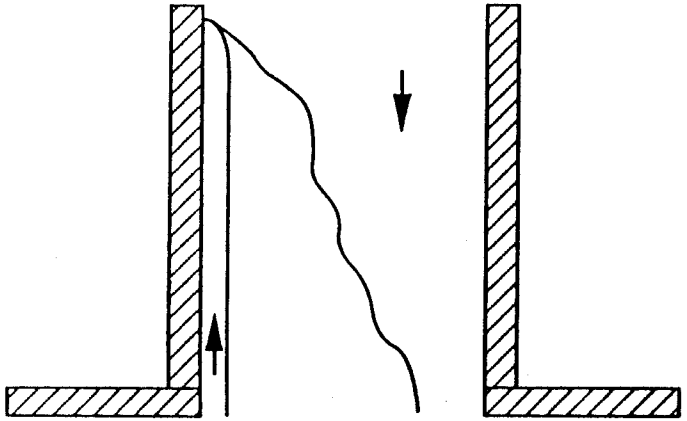

3.1A: CORE AND OUTER REGION OF A PLUME AT ITS QUASI-STEADY MAXIMUM HEIGHT

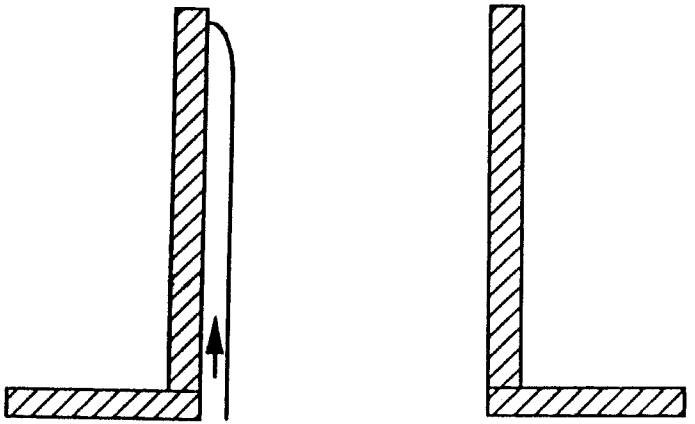

3.1B: CORE REGION ONLY

Figure 3.1 Description of Buoyant Plume's Core and Outer Regions at its Quasi-Steady Maximum Height.

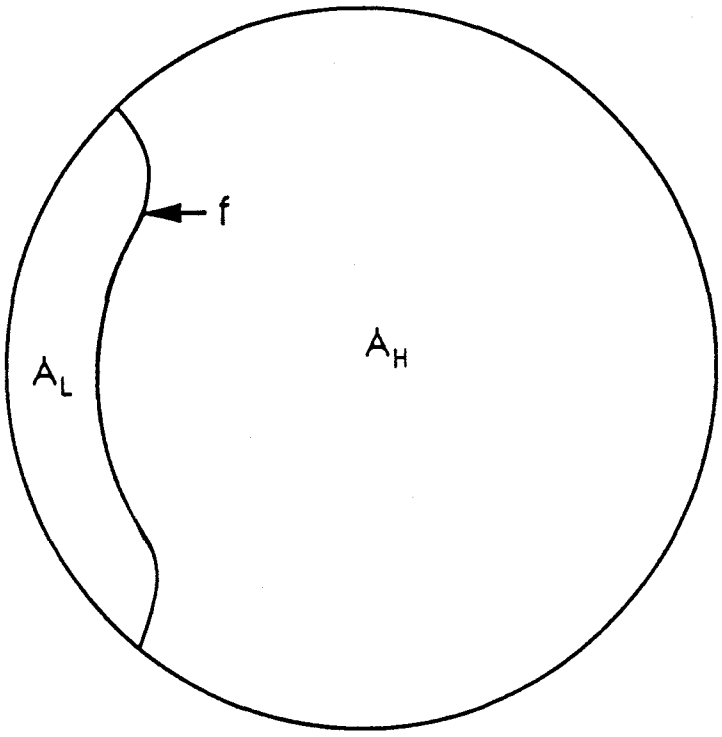

Figure 3.2 Schematic of the Cross-Sectional Area of the Core of the Plume, A_L, the Downflow Area, A_H, and the Interfacial Dimension, f.

respect to height, A_H and f must also be constant with respect to height. It will later be seen that A_L and f both enter the analysis in such a way as to form products with uncertain turbulent quantities and also in such a way as not to affect the functional relationships derived. Since determining the precise values of A_L and f would neither reduce the uncertainty of these products nor affect the functional relationships derived, no attempt will be made to determine the values of these quantities.

In addition to the cross-sectional areas, assumptions must be made regarding the velocity profiles. The velocities, V_L and V_H, will be assumed constant over their respective areas due to the relative flatness of turbulent velocity profiles. While V_L will vary with height, V_H will remain constant due to the constancy of both the injection flow rate and A_H. (Actually V_H will increase slightly in the downward direction due to increases in the mass flow rate caused by entrainment. This effect will be assumed negligible.) With the velocities defined in this manner, the relative velocity between the two fluids may be expressed as $V_R = V_L+V_H$. From this definition it can be seen that the constancy of V_H implies that the derivatives of both V_R and V_L with respect to height are identical.

Finally, since the plume behavior is significantly affected by friction and entrainment, it is necessary to make some assumptions regarding these effects. In determining the frictional effects on the plume, the wall friction will be neglected in comparison to the interfacial friction. The

latter quantity will be expressed as $C_{fi}(\rho V_R^2/2)$ where C_{fi} is an interfacial friction factor. With respect to the subject of entrainment, the transfer of fluid from one region to another will occur as the result of lateral entrainment velocities at the interface. As is common in plume problems, these will be assumed proportional to the relative velocity. Having made these preliminary assumptions, the critical conditions will now be determined.

3.3 Critical Conditions

The first thrust of the theoretical analysis must be to determine the critical conditions since these are foundational to analyzing the penetration depth. Most significant in this regard is the previous experience of two researchers in studying the flow from cooling towers. (It should be re-emphasized here that the cooling tower research is directly applicable to the present problem since the upward flow of positively buoyant fluid from cooling towers is dynamically equivalent to the downward flow of negatively buoyant fluid from HPI lines.) As mentioned in section 1.3.2, Dr. F.K. Moore[9],[10] studied the cooling tower problem under turbulent conditions. He noted that when the exit velocity was large, the emerging plume diverged upon leaving the tower as shown in Figure 3.3a. For lower velocities, however, the buoyancy became more significant, causing an initial acceleration and consequent convergence of the plume as shown

in Figure 3.3b. For still lower velocities ambient fluid penetrated into the cooling tower as shown in Figure 3.3c. Since this problem is dynamically equivalent to the reactor problem, a decreasing injection velocity should cause the same trends in the HPI line as shown in Figures 3.3d-f.

In studying this same problem, Dr. Vijay Modi[13] through excellent scientific reasoning illustrated several effects caused by the low velocity convergence of the jet. He stated that due to the elliptic nature of the Navier Stokes equations, this convergence causes the bending of initially straight streamlines within the cooling tower. In his analysis of this effect, Modi noted that in the bending process, the wall retains its identity as a streamline. Since the wall cannot bend, the curvature of the other streamlines forces the distance between streamlines to increase near the wall as the exit is approached. This situation clearly implies that the velocity near the wall decreases in the vicinity of the exit. Since these effects increase as the exit velocity is reduced, the flow near the wall becomes increasingly vulnerable to penetration. Obviously, since the cooling tower and reactor injection problems are dynamically equivalent, the same streamline bending would be expected in the reactor injection line as shown in Figure 3.4.

In an experimental cooling tower study involving a warm laminar airflow, Dr. Modi found that as the critical conditions were approached, the initial bursts of ambient fluid penetrated randomly around the periphery of a model

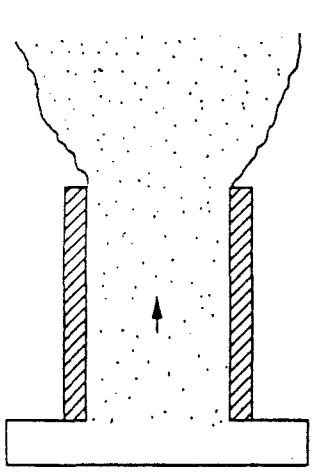

3.3A: PLUME DIVERGENCE

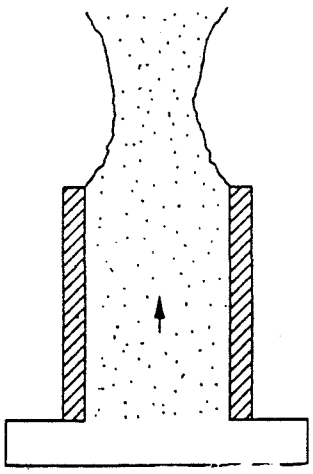

3.3B: PLUME CONVERGENCE

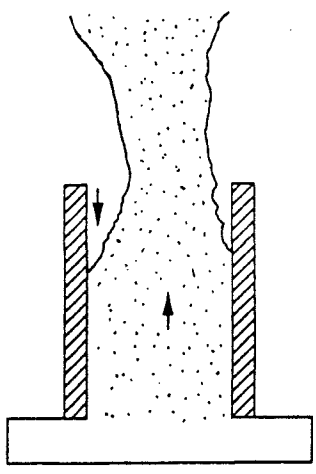

3.3C: AMBIENT PENETRATION

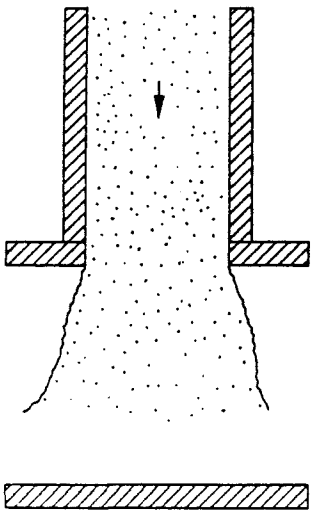

3.3D: JET DIVERGENCE

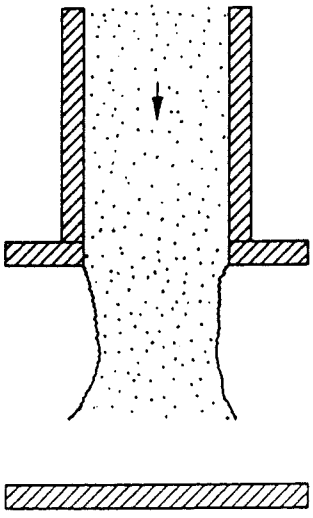

3.3E: JET CONVERGENCE

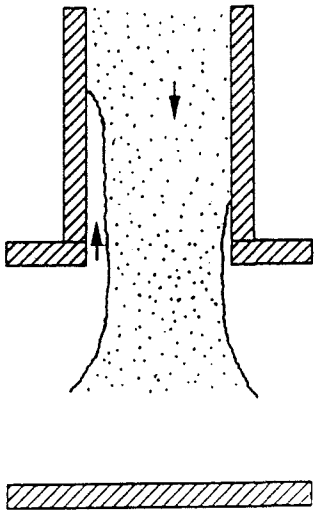

3.3F: AMBIENT PENETRATION

Figure 3.3 Buoyant Flow in Cooling Towers and Vertical High Pressure Injection Lines.

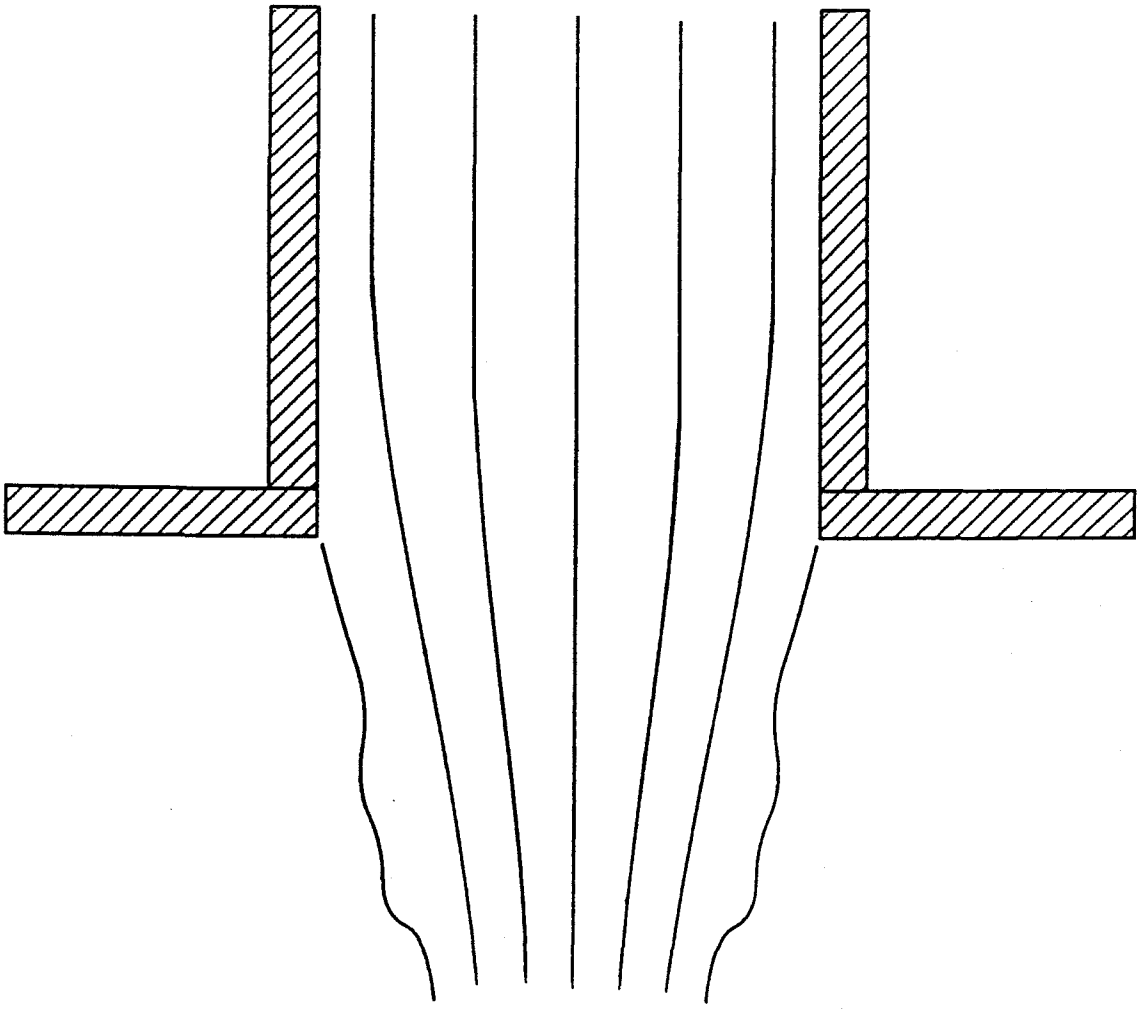

Figure 3.4 Bending of the Streamlines Inside a High Pressure Injection Line.

cooling tower. In addition he observed that further reductions in the Froude number lead to a "wavy interface pocked at regular intervals by a mass of cold air plunging in." Based on a discussion with Dr. Modi, it was determined that for the reactor problem the observed interface would look like that shown in Figure 3.5.

Having discussed these significant points, the preceding information may now be judiciously applied to the reactor problem to determine the penetration mechanism. First, at low injection velocities the predominance of buoyancy causes an initial acceleration and consequent necking of the jet, allowing the light ambient fluid to position itself beneath the heavy fluid at the HPI circumference. As the injection velocity is further lowered, the effect of the increasing streamline curvature within the HPI causes an increasing deceleration of the flow near the wall in the vicinity of the exit. The flow near the wall thus becomes increasingly vulnerable to penetration until a point is reached where the ambient fluid having previously positioned itself beneath the heavy, penetrates into the HPI line. The sudden waviness of the interface just beyond this point indicates that the penetrations are caused by the Rayleigh Taylor instability[18] with the associated wave lengths determining the cross-sectional shapes of the plumes. It would seem then that the critical conditions could be obtained from the requirement that the Rayleigh Taylor perturbations be able to penetrate against the downflow. It is to this end that attention will

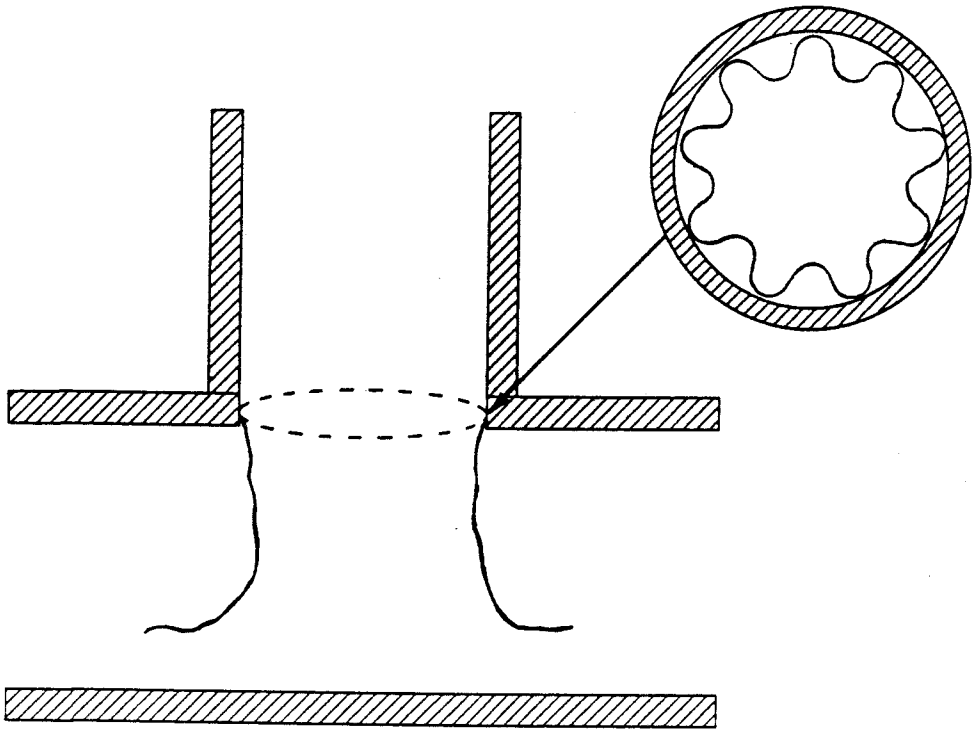

Figure 3.5 Wavy Interface at the Onset of Backflow.

now be focused.

To determine the critical conditions, an initial perturbation of cross-sectional area, A_L, and interfacial dimension, f, is assumed to have penetrated a distance, dz, into the HPI. Under these conditions such a perturbation will be subject to an upward buoyancy force, $g\Delta\rho A_L dz$, and a downward friction force, $C_{fi}(\rho V_R^2/2)fdz$. Clearly, if buoyancy exceeds friction, the perturbation will rise, and if the reverse is true, it will not. The onset condition is therefore determined by the equality of these two opposing forces.

$$C_f \frac{\rho V_R^2}{2} f dz = g\Delta\rho A_L dz \qquad (3.1)$$

Because this equation expresses a terminal force condition on the plume, the relative velocity involved, V_R, is the maximum possible relative velocity between the two fluids, V_{Rmax}. Since penetrations obviously cannot occur when the downflow velocity exceeds this maximum value, this value must in fact be the critical value, V_{crit}. Furthermore, because the perturbation has zero velocity in the critical state, the critical relative velocity, V_{crit}, and the downflow velocity, V_H, are then identical. Finally, since the plume is thin, the near equivalence of the downflow and cross-sectional areas

allows the downflow velocity to be estimated by the average velocity of injection, V_{inj}. By making this substitution and rearranging, equation (3.1) may be re-expressed as

$$\frac{V_{inj}^2}{g\frac{\Delta\rho}{\rho}\frac{A_L}{f}} = \frac{2}{C_{fi}} \tag{3.2}$$

Equation (3.2) defines a critical Froude number relationship based on a peculiar length scale, A_L/f. If C_{fi} can be assumed to be fairly constant in the turbulent regime, and if A_L/f is also somewhat constant, equation (3.2) may be multiplied by A_L/fD to yield a more conventional Froude number relationship for the critical conditions.

$$\frac{V_{inj}^2}{g\frac{\Delta\rho}{\rho}D} = \frac{2}{C_{fi}}\frac{A_L}{fD} \tag{3.3}$$

However, since the critical Froude number derived in equation (3.2) is based on A_L/f and not D, problems may arise in using a diameter based Froude number to scale the critical conditions. More will be said about this possibility in

chapter 4.

With respect to equation (3.2), it should be noted that the values of A_L and f do not affect its functional form. In addition, because a turbulent interface between two miscible fluids is hard to define, the value of the interfacial friction factor is also highly uncertain. Since the values of A_L and f do not affect the functional form of equation (3.2), and since C_{fi} is uncertain; determining the precise values of A_L and f has little benefit. As a consequence, it makes more sense to rearrange the equation and lump these parameters together with g into an experimental constant to express the critical relationship between the experimental control variables

$$V_{Rmax} = V_{crit} = V_H \sim V_{inj} = k\sqrt{\frac{\Delta\rho}{\rho}} \qquad (3.4)$$

In this expression the previously mentioned velocities have been included to re-emphasize their mutual equality in the critical state.

Equation (3.4) was used to compare the theoretical development with the experimental results. In this comparison the experimental values of V_{crit} were first plotted against the corresponding values of $\sqrt{\Delta\rho/\rho}$. The theoretical relationship was then matched to the experimental data to determine the

proportionality constant and tested by the tightness of fit. It can be seen from Figure 3.6 that equation (3.4) was well satisfied by the experimental data producing a proportionality constant of 57.16 cm/s and an R squared value of .97.

To express the critical conditions in a more conventional form, equation (3.4) was rearranged to yield a critical Froude number relationship

$$Fr = .65 \tag{3.5}$$

which is the numerical counterpart of equation (3.3). This relationship was also plotted against the experimental data as shown in Figure 3.7. As can be seen from the figure, a constant Froude number relationship expresses the critical conditions quite well for all but the lowest value of $\Delta\rho/\rho$. Since this case involved the lowest critical velocity, the divergence of the data at this point may have resulted from a thickening of the boundary layer in the injection line. In spite of this short coming, the relationship between theory and experiment is again quite good, lending credibility to the previous theoretical development. The penetration depth may now be analyzed.

3.4 Penetration Depth

Having determined the critical conditions, it is now

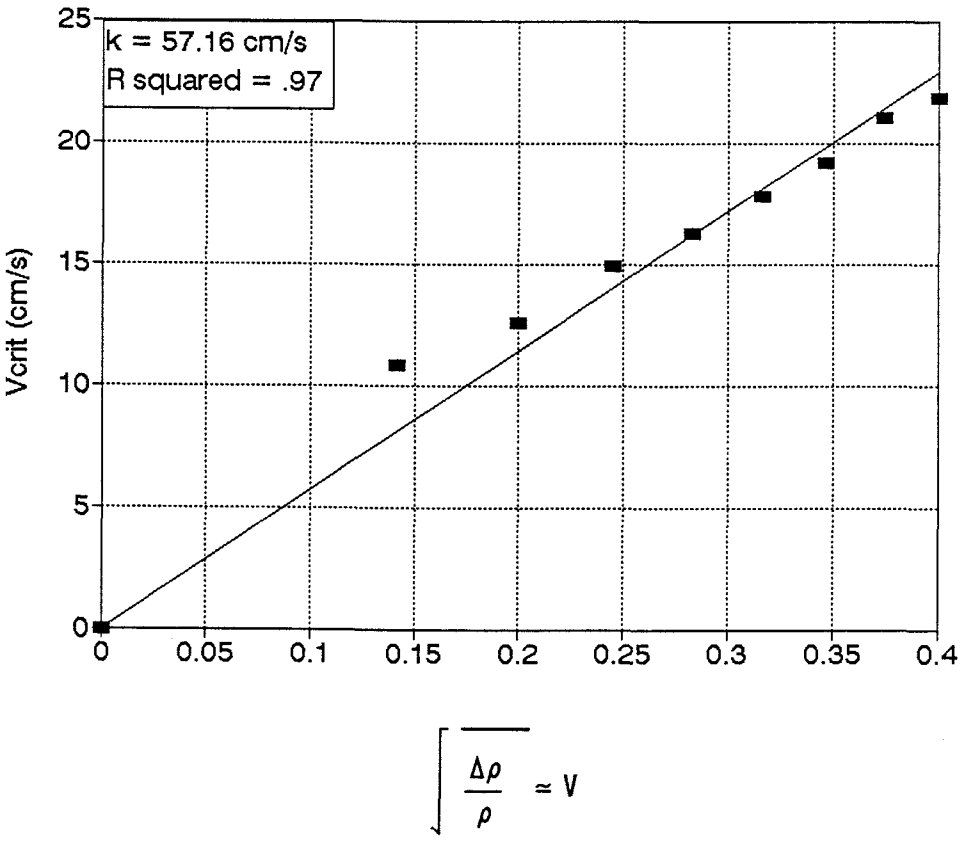

Figure 3.6 The Linear Relationship between the Critical Velocity and the Square Root of the Fractional Density Difference as Demonstrated Using Experimental Data. (Uncertainty in the Velocity is less than .47 cm/s; Uncertainty in the Square Root of $\Delta\rho/\rho$ is less than 2.5 %.)

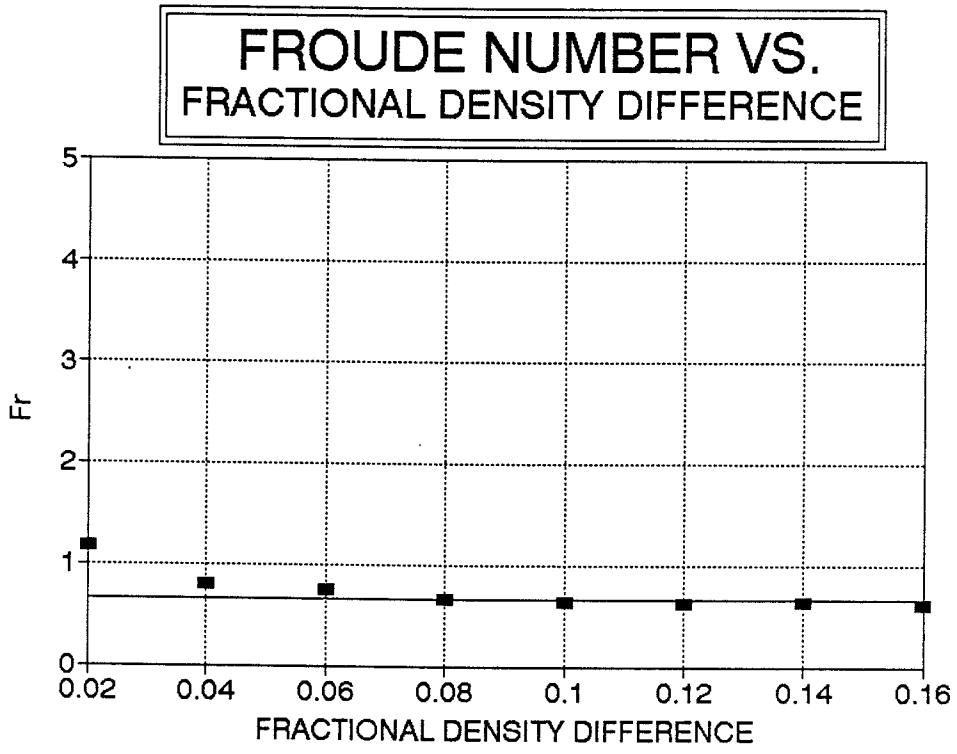

Figure 3.7 The Constant Critical Froude Number Relationship as Demonstrated Using Experimental Data. (Uncertainty in the Froude Number is less than 10 %; Uncertainty in $\Delta\rho/\rho$ is less than 5 %.)

possible to analyze the relationship between the penetration depth and the injection velocity. As mentioned previously, the plume reaches a quasi-steady maximum height before breaking up. For this reason the analysis of the maximum height will assume the existence of steady state conditions. This analysis is best begun by observing several general trends in the core region of the plume.

If the mass flow rates into and out of a differential slice of the core region are examined, it is evident that at the interface between the two flow regions, fluid both leaves and enters the core at each axial level along the plume. This entrainment process, shown in Figure 3.8, has two major effects. First, because the entrainment acts to transfer heavy fluid in and light fluid out, the density difference in the core decreases with height from a maximum value at the bottom. A second effect of this entrainment process is that the incoming fluid has negative momentum whereas that of the outgoing fluid is positive. The entrainment process, therefore, acts to reduce both the buoyancy and the momentum in the core, causing the velocity to also decrease with height.

If the continuity equation is next applied to the core region as a whole, two facts are immediately evident. First, steady state conditions imply that the incoming mass flow rate at the bottom of the core must be identically balanced by entrainment losses at the interface. Second, because entrainment is a loss mechanism, the rate of outgoing

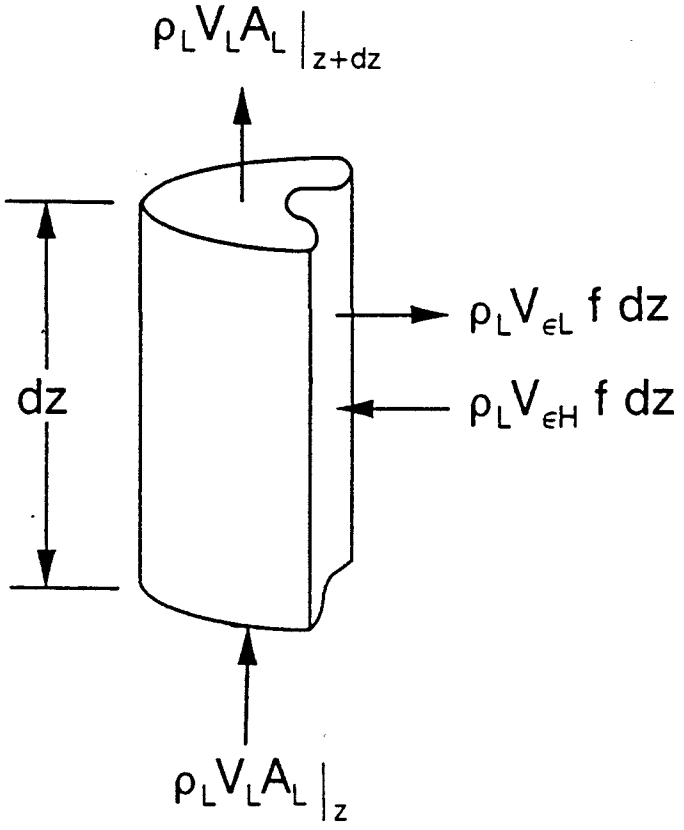

Figure 3.8 Mass Conservation for a Differential Slice of the Plume Core Region.

entrainment must exceed the incoming rate.

The significance of the first observation is that the mass balance implied by steady state conditions may be used to determine the maximum height of the plume. The reason for this fact is that the plume will rise until it obtains sufficient surface area so that entrainment losses balance incoming gains. Stated differently, when the plume reaches the height where entrainment losses balance incoming gains, the mass flow rate at the top will be zero, and the plume will cease to rise beyond this point. The situation implied by this mass balance is that the maximum plume height will increase as the incoming mass flow rate increases and as the entrainment becomes less vigorous. From this discussion, then, it would seem that the most direct way to determine the height of the plume would be to apply the continuity equation directly to the core region as a whole. Unfortunately, however, such a procedure is not possible at this point in the analysis because the resulting integration would require a knowledge of the velocity profile in the core. To obtain this information the continuity equation must first be solved in differential form.

The differential form of the continuity equation is obtained by performing a mass balance on the differential core slice shown in Figure 3.8 and dividing the result by dz to yield

$$\frac{d(\rho_L V_L A_L)}{dz} = \rho_H V_{\epsilon H} f - \rho_L V_{\epsilon L} f \tag{3.6}$$

Since this equation involves six unknowns, its solution would ordinarily require the simultaneous solution of two other conservation equations plus three additional relations. Fortunately, several simplifying assumptions are possible. First, A_L and f may be assumed constant with height as mentioned previously. Second, the Boussinesq approximation may be invoked to eliminate the density variations and therefore make the densities constant and equal in the continuity equation. Third, as mentioned previously, the lateral entrainment velocities, $V_{\epsilon H}$ and $V_{\epsilon L}$, may be considered proportional to the relative velocity and expressed as $\epsilon_H V_R$ and $\epsilon_L V_R$, respectively. Implementing these assumptions and rearranging yields.

$$A_L \frac{dV_L}{dz} = -(\epsilon_L - \epsilon_H) V_R f \tag{3.7}$$

Since the net entrainment is out of the core, ϵ_L exceeds ϵ_H, and the quantity, $(\epsilon_L - \epsilon_H)$, may be defined as ϵ, the net entrainment coefficient. In addition, the derivative of the plume velocity may be replaced by the derivative of the rela-

tive velocity as mentioned previously. Making these substitutions yields

$$\frac{dV_R}{dz} = - \frac{\epsilon f}{A_L} V_R \tag{3.8}$$

This is the simplest type of differential equation possible, and its solution is

$$V_R(z) = V_{RO}\, e^{-\left[\frac{\epsilon f z}{A_L}\right]} \tag{3.9}$$

The question that now arises is how to evaluate the boundary condition, V_{RO}. In this regard, it was mentioned previously that the plume would rise to greater heights as the incoming mass flow rate was increased. Since the purpose of this analysis is ultimately to evaluate the maximum height of the plume, it is logical to suppose that when the plume reaches its maximum possible height, the initial velocity and, hence, the initial relative velocity are also at their maximum possible values. However, the maximum possible value of the relative velocity is simply the value determined from the friction-buoyancy balance in equation (3.1). Thus V_{RO} may be replaced by V_{crit}, and equation (3.9) becomes

$$V_R(z) = V_{crit}\, e^{-\left[\frac{\epsilon f z}{A_L}\right]} \tag{3.10}$$

With the velocity distribution in the core region known, the maximum plume height may now be determined from the global application of the continuity equation to the core. Setting the incoming mass flow rate equal to the entrainment losses yields

$$\rho_L V_{LO}\, A_L = \int_0^h \rho_L \epsilon V_R f dz \tag{3.11}$$

Replacing V_R by its expression from equation (3.9), integrating, and canceling like terms yields

$$V_{LO} = V_{RO}\left(1 - e^{-\left[\frac{\epsilon f h}{A_L}\right]}\right) \tag{3.12}$$

By rearranging this equation and taking the logarithm of both sides, the maximum height may be determined as

$$h = -\frac{A_L}{\epsilon \bar{f}} \ell n\left[\frac{V_{RO}-V_{LO}}{V_{RO}}\right] \tag{3.13}$$

In this expression it should be recognized that $(V_{RO}-V_{LO})$ is simply the downflow velocity, V_H. As mentioned previously, this quantity is approximately equal to the average injection velocity, V_{inj}, due to the slenderness of the plume. It should also be noted that through its effect on A_L and f, the assumed cross-sectional shape of the plume merely affects the coefficient in equation (3.13) and not the functional form of the relationship. In addition, since the turbulent entrainment coefficient, ϵ, like the interfacial friction factor, C_{fi}, is impossible to determine analytically, no precision would be gained by determining the values of A_L and f. For these two reasons, it makes more sense to lump these quantities together with the pipe diameter into a single experimental constant and recast equation (3.13) in its final form.

$$\frac{h}{D} = k\left[-\ell n\left(\frac{V_{inj}}{V_{crit}}\right)\right] \tag{3.14}$$

For each of the experimental values of the fluid fractional density difference, the backflow heights were plotted against the negative logarithm of the velocity ratio,

and the constants of proportionality were determined from a statistical analysis. The results of this procedure are shown in Figures 3.9-3.16 from which it will be seen that the plots are fairly linear with proportionality constants ranging from 2.73 to 3.75 and most of the R squared values in excess of .94. These values were then combined into a cumulative plot and subjected to the same statistical analysis. It can be seen from Figure 3.17 that the cumulative data is also quite linear, producing a proportionality constant of 3.45 and an R squared value of .93.

The agreement of the experimental results with equation (3.14) justifies the previous theoretical development. A further justification can be found in the fact that equation (3.14) predicts no penetration depth at the critical injection velocity and an infinite penetration depth for no injection velocity. Since this equation correctly predicts the extremes and is itself a smooth function, it should be expected to perform well at intermediate values.

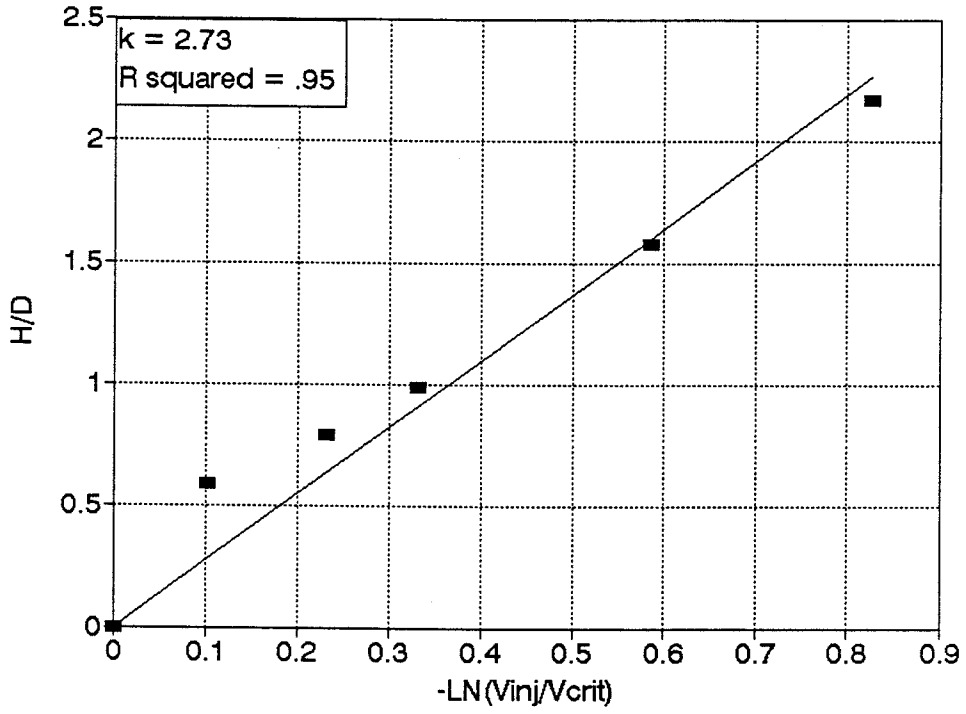

Figure 3.9 Comparison of Equation (3.14) with Experimental Data for $\Delta\rho/\rho = 0.02$. (Uncertainty in H/D is less than .1; Uncertainty in $\ln(V_{inj}/V_{crit})$ is less than .11.)

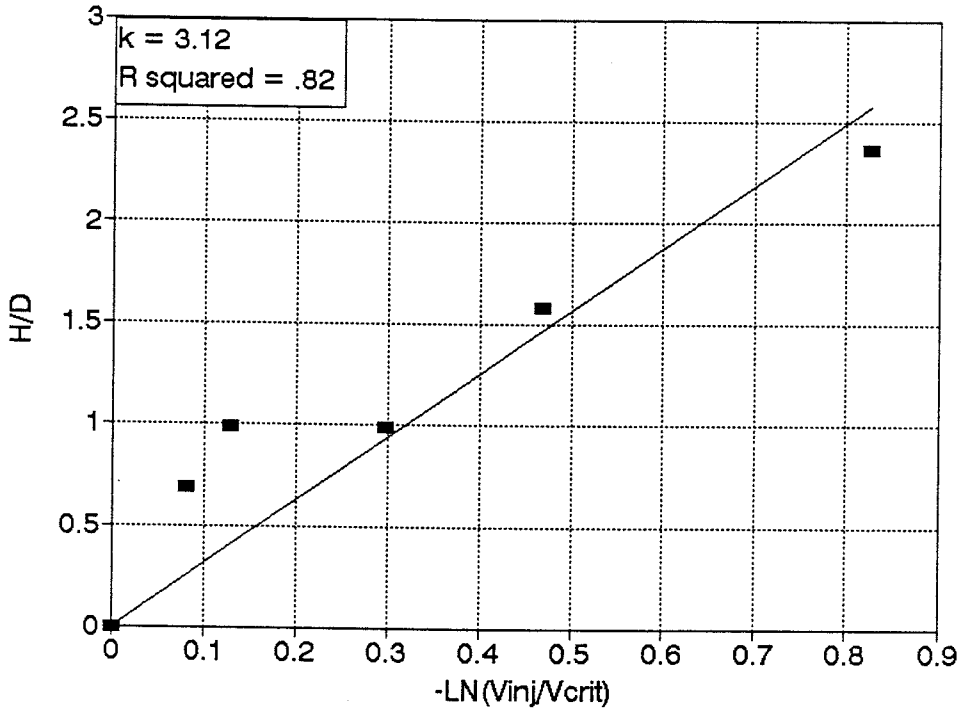

Figure 3.10 Comparison of Equation (3.14) with Experimental Data for $\Delta\rho/\rho = 0.04$. (Uncertainty in H/D is less than .1; Uncertainty in $\ln(V_{inj}/V_{crit})$ is less than .11.)

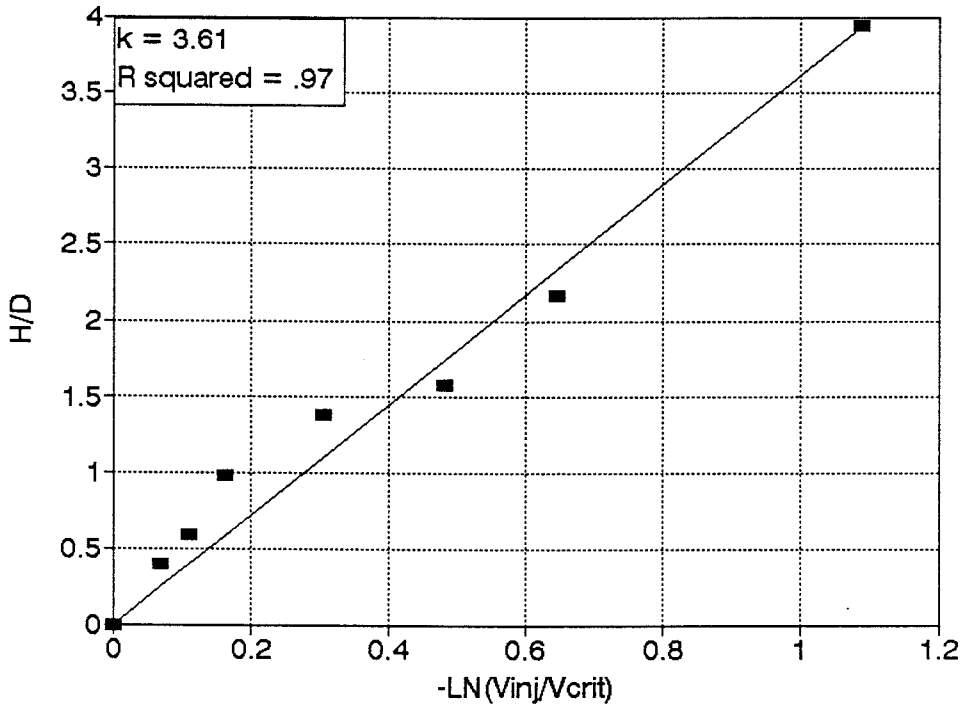

Figure 3.11 Comparison of Equation (3.14) with Experimental Data for $\Delta\rho/\rho = 0.06$. (Uncertainty in H/D is less than .1; Uncertainty in $\ln(V_{inj}/V_{crit})$ is less than .11.)

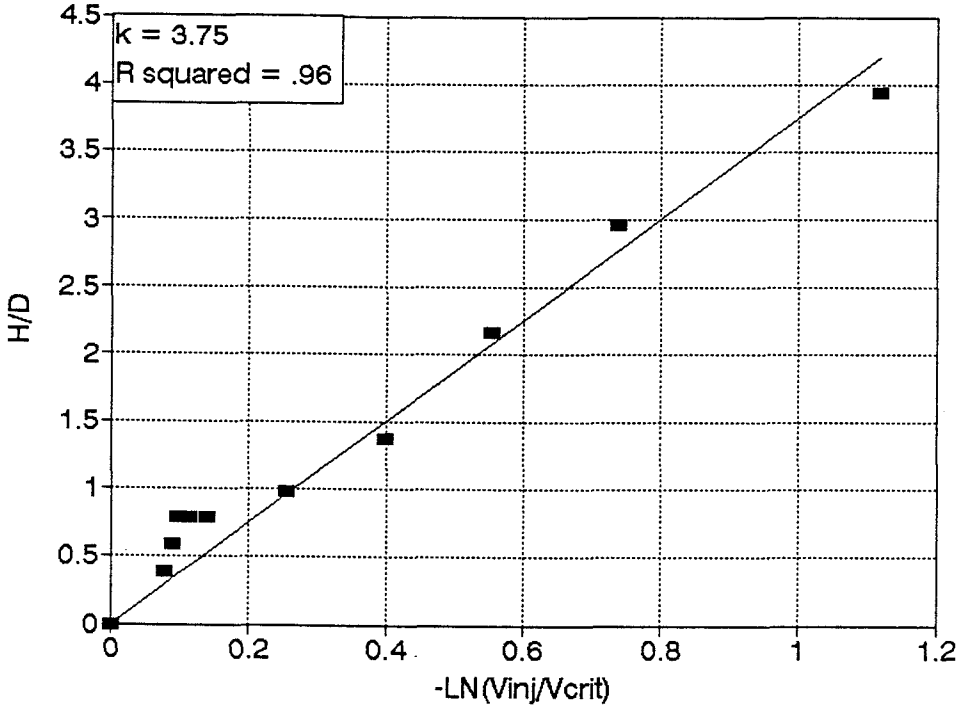

Figure 3.12 Comparison of Equation (3.14) with Experimental Data for $\Delta\rho/\rho = 0.08$. (Uncertainty in H/D is less than .1; Uncertainty in $\ln(V_{inj}/V_{crit})$ is less than .11.)

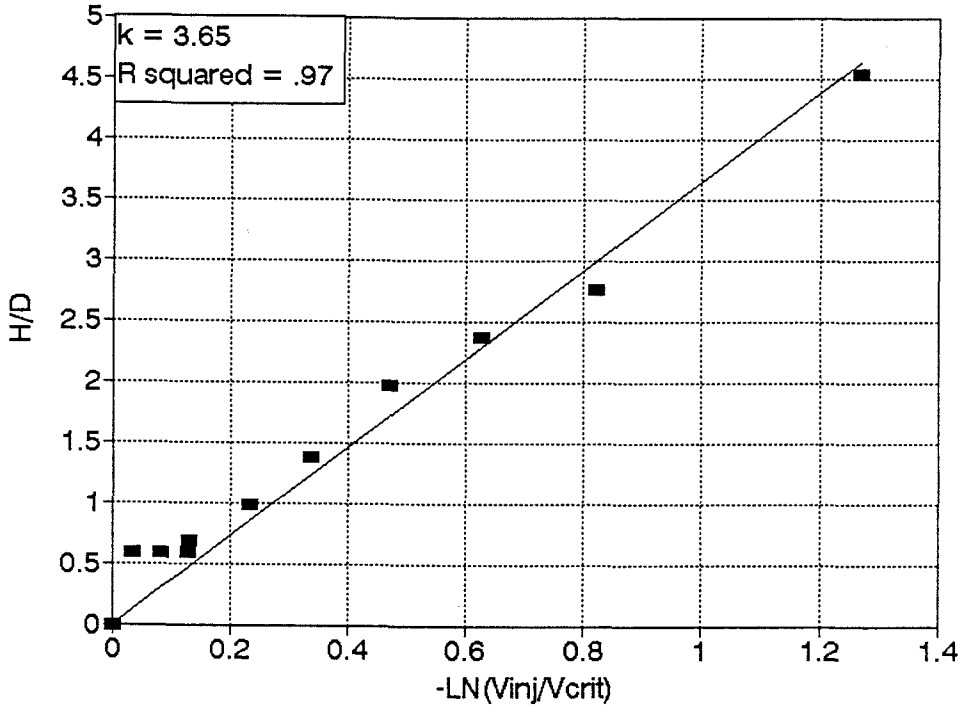

Figure 3.13 Comparison of Equation (3.14) with Experimental Data for $\Delta\rho/\rho = 0.10$. (Uncertainty in H/D is less than .1; Uncertainty in $\ln(V_{inj}/V_{crit})$ is less than .11.)

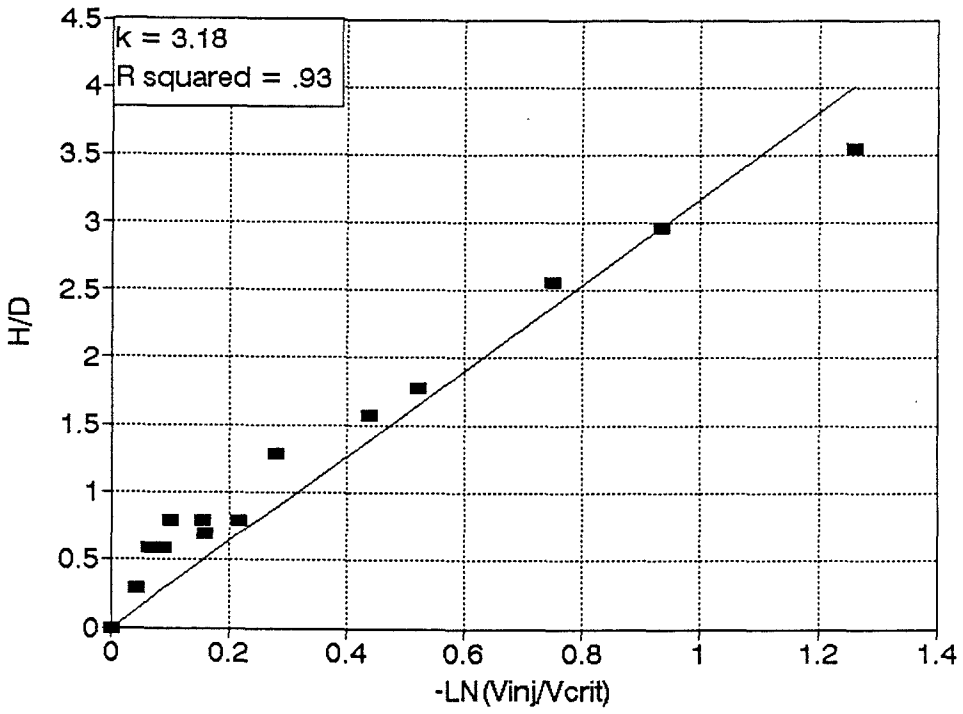

Figure 3.14 Comparison of Equation (3.14) with Experimental Data for $\Delta\rho/\rho = 0.12$. (Uncertainty in H/D is less than .1; Uncertainty in $\ln(V_{inj}/V_{crit})$ is less than .11.)

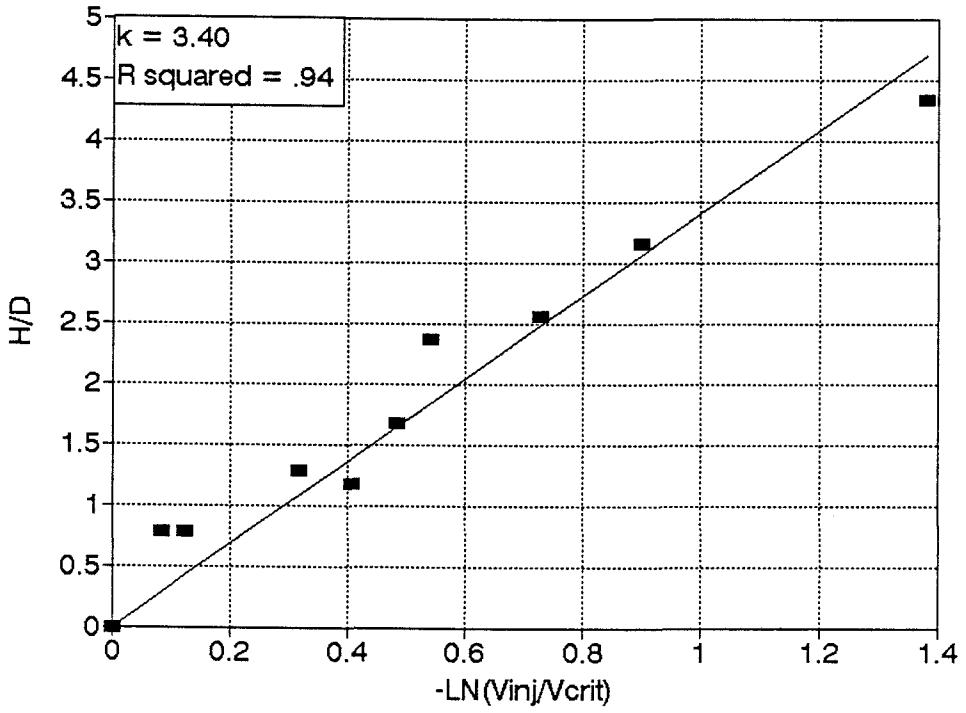

Figure 3.15 Comparison of Equation (3.14) with Experimental Data for $\Delta\rho/\rho = 0.14$. (Uncertainty in H/D is less than .1; Uncertainty in $\ln(V_{inj}/V_{crit})$ is less than .11.)

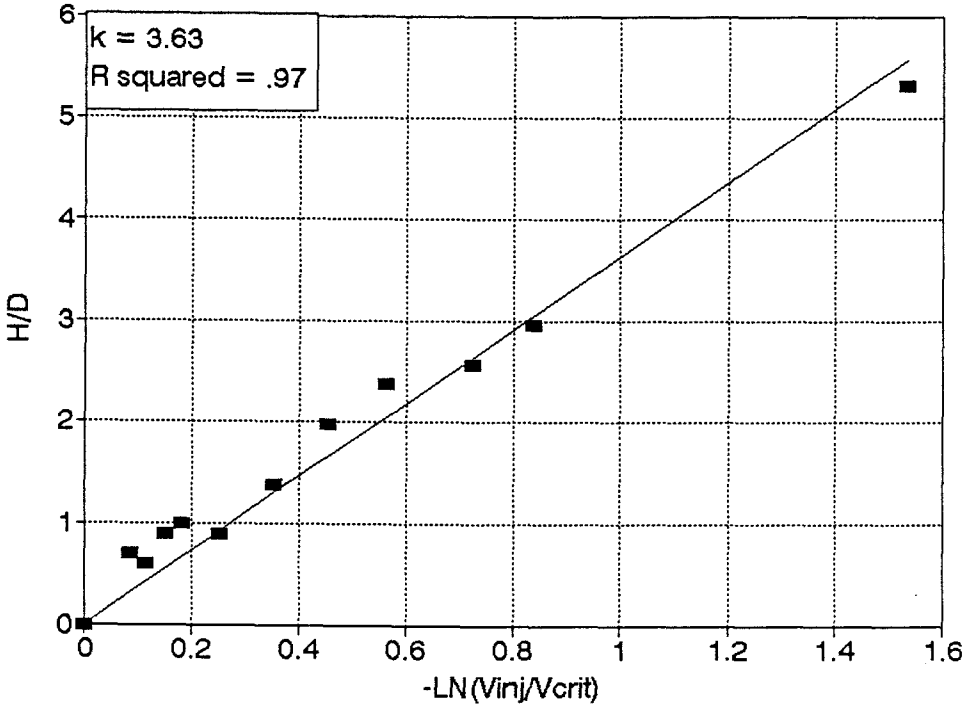

Figure 3.16 Comparison of Equation (3.14) with Experimental Data for $\Delta\rho/\rho = 0.16$. (Uncertainty in H/D is less than .1; Uncertainty in $\ln(V_{inj}/V_{crit})$ is less than .11.)

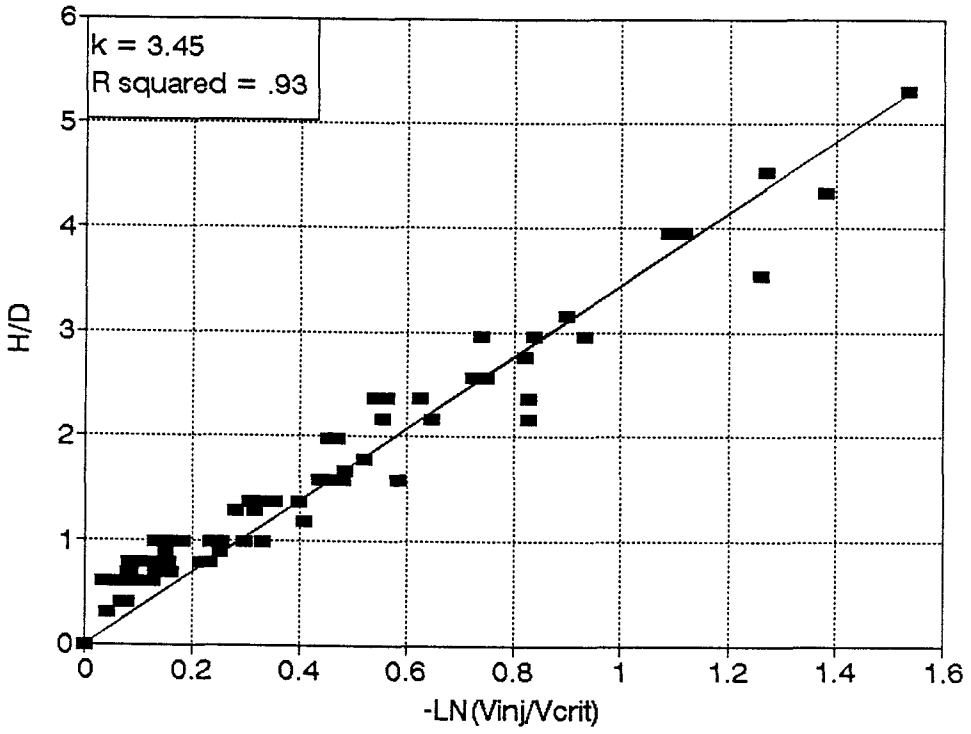

Figure 3.17 Comparison of Equation (3.14) with All the Experimental Data for $\Delta\rho/\rho$ = 0.02 to 0.16. (Uncertainty in H/D is less than .1; Uncertainty in $\ln(V_{inj}/V_{crit})$ is less than .11.)

CHAPTER 4

FULL SCALE ANALYSIS

4.1 Introduction

To evaluate the penetration behavior in the prototype, it remains to scale the results of chapters 2 and 3. From the discussions in sections 1.2 and 2.2, it would seem that this scaling should be performed in terms of a Froude number based on the pipe diameter. In contrast to this criteria, however, equation (3.2) expresses the critical conditions in terms of a Froude number based on a different length scale, A_L/f. Since these parameters differ in terms of the length scales involved, the comparative behavior of the two length scales may complicate the scaling analysis. As a consequence, a discussion of the length scales must precede the full scale evaluation.

4.2 Determination of the Scaling Length

The first step in addressing the length scale problem is to determine whether the scaling parameters produce divergent scaling requirements. Since proportionality between the length scales would eliminate distinctions between the scaling parameters, it is necessary to test the two scales for proportionality. In this regard it should be remembered from

chapter 3 that A_L/f is determined by the cross-sectional shape of the plume. Since the penetration is initiated by the Rayleigh Taylor instability, A_L/f is therefore determined by the Rayleigh Taylor wave lengths. By working out the details of a Rayleigh Taylor instability analysis[18], it may be shown that the wave lengths scale with the quantity, $(\sigma/\Delta\rho g)^{1/2}$, where σ is the surface tension between the two fluids. Since A_L/f must also scale with this quantity, it is not proportional to the pipe diameter.

Because the two length scales are not proportional, the resulting parameters will place conflicting demands on the scaling analysis. A possible way of resolving this conflict is to eliminate one of the scales on the basis of its comparative significance in the problem. In this regard the significance of A_L/f follows from the fact that it accounts for the cross-sectional shape of the plume. As a consequence, it must be retained in the analysis. In contrast to A_L/f, the physical significance of the pipe diameter is not evident. It entered the analysis as an arbitrary choice for the length scale in equation (1.9). The weakness of this choice is the implicit assumption that all physical effects in the problem scale with the pipe diameter. This is not necessarily true, especially in regard to the turbulent quantities. In spite of this weakness, however, diameter based Froude numbers have been successfully used to scale the critical conditions[4]. As a consequence of this empirical significance, the diameter must also be retained.

Since neither length scale may be eliminated from the problem, it is necessary to incorporate both in the scaling analysis. A possible method for this incorporation may be determined by analogy to the problem of reactor flooding. As shown in Figure 4.1, the central problem in reactor flooding is caused by a large break LOCA and involves the blockage of cold fluid from the reactor core by high velocity steam. In accordance with standard accident procedures, the cold fluid shown in the figure is introduced by the ECCS response to the system break. However, as a result of the rapid depressurization and the location of the break, the primary fluid flashes into steam and travels in reverse direction through the downcomer annulus. During the initial phase of the transient, the steam travels at high velocities, effectively blocking the cold fluid. As the steam velocity decreases, however, a point is eventually reached where the cold fluid penetrates against the upward flow of steam and begins to flood the core. Since this flooding is needed to cool the reactor, a considerable amount of research has been undertaken to determine the critical conditions for counter current penetration.

A significant result of this research is that the critical conditions have been demonstrated to switch from Wallis to Kutateladze scaling with increasing pipe diameters[19],[20]. To understand the significance of this transition, it is necessary to briefly consider these two parameters. The Wallis number is simply the square root of

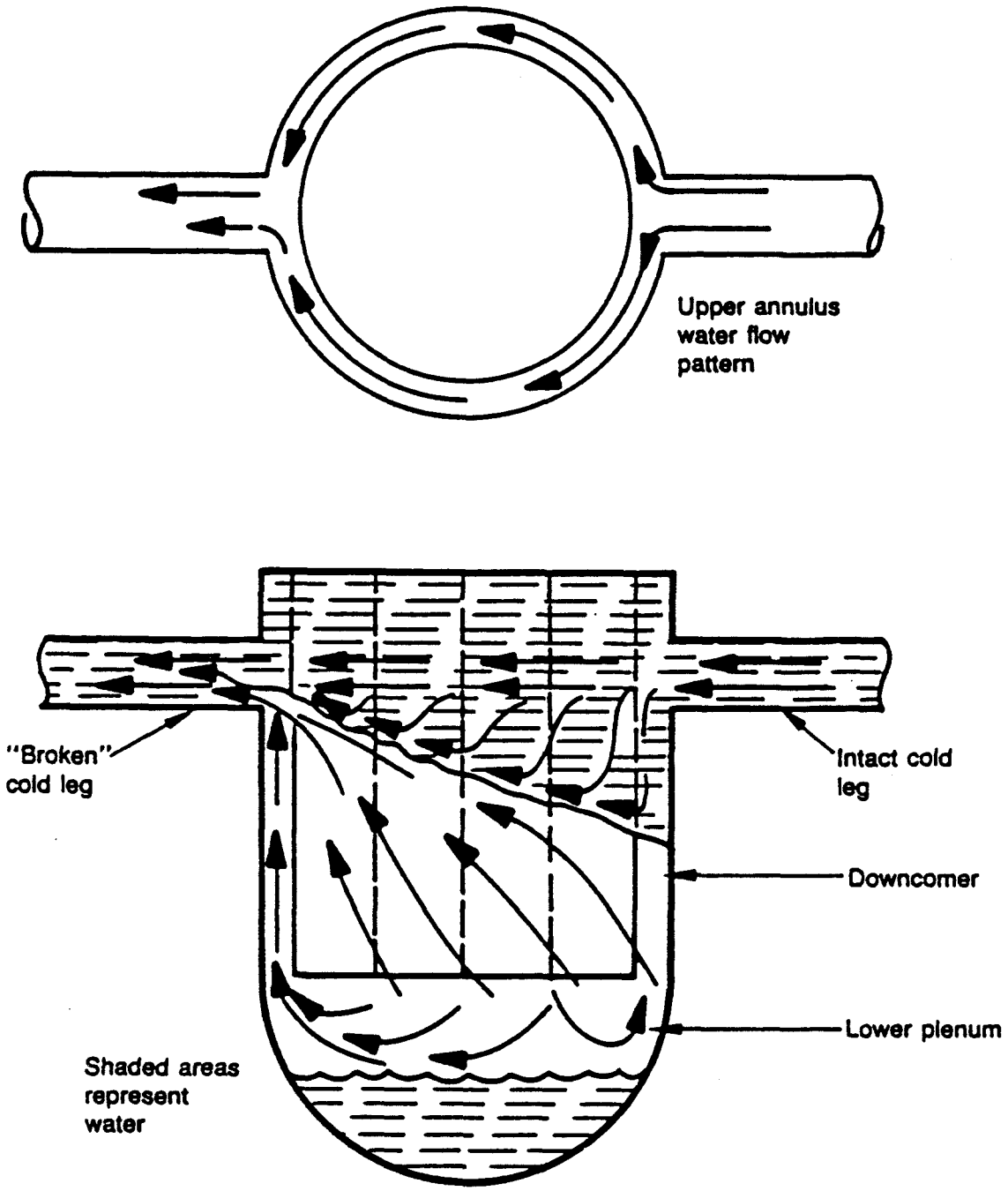

Figure 4.1 Description of the Flooding Problem in a PWR.

the Froude number and therefore depends on the pipe diameter. The Kutateladze number, on the other hand, is defined as

$$Ku = \frac{V\rho_H^{1/2}}{(g\sigma\Delta\rho)^{1/4}} \tag{4.1}$$

where σ, as previously, is the surface tension between the two fluids. As can be determined by direct substitution, the Kutateladze number is simply the square root of a Froude number based on a Rayleigh Taylor wave length scale, $(\sigma/\Delta\rho g)^{1/2}$[18],[20]. Since the only difference between the Wallis and Kutateladze numbers is the length scale involved, the change in scaling behavior necessarily results from a length scale transition with increasing pipe diameters. It is possible that such a transition may occur in the backflow problem as well.

To establish this fact it is necessary to demonstrate that flooding and backflow are truly analogous problems. To make this demonstration it must be shown that both problems involve identical length scales and scaling parameters. With respect to length scales, the flooding problem involves the pipe diameter and the Rayleigh Taylor wave length. The backflow problem, on the other hand, involves the pipe diameter and A_L/f. Because the diameter is already common to both problems, it is simply necessary to show that A_L/f is identical to the Rayleigh Taylor wavelength.

To prove this identity it must first be remembered that the plume is initiated by the Rayleigh Taylor instability. As a consequence, the cross-sectional area of the plume may be related to the Rayleigh Taylor wave lengths as shown in Figure 4.2. If the dimensions of this area are determined by Rayleigh Taylor wave lengths, λ_r and λ_θ, in the r and θ directions, A_L/f may be expressed as

$$\frac{A_L}{f} \simeq \frac{\lambda_r \lambda_\theta}{(2\lambda_r + \lambda_\theta)} \simeq \lambda_r \sim \left(\frac{\sigma}{\Delta\rho g}\right)^{1/2} \qquad (4.2)$$

where the simplification results from the thinness of the plume. Since A_L/f and the Rayleigh Taylor wave length are therefore identical, it is clear that the backflow and flooding problems involve identical length scales.

Having demonstrated the equivalence of the length scales, it is next necessary to show that identical scaling parameters govern each problem. With respect to the scaling parameters, the flooding problem involves the Wallis and Kutateladze numbers whereas the backflow problem involves the Froude number. Since the Froude number is simply the square of the Wallis number, it remains to show that the backflow problem involves a Kutateladze number equivalent.

In this regard it will first be shown that Kutateladze scaling is implied by equation (3.2). As mentioned previously, equation (3.2) is simply a Froude number

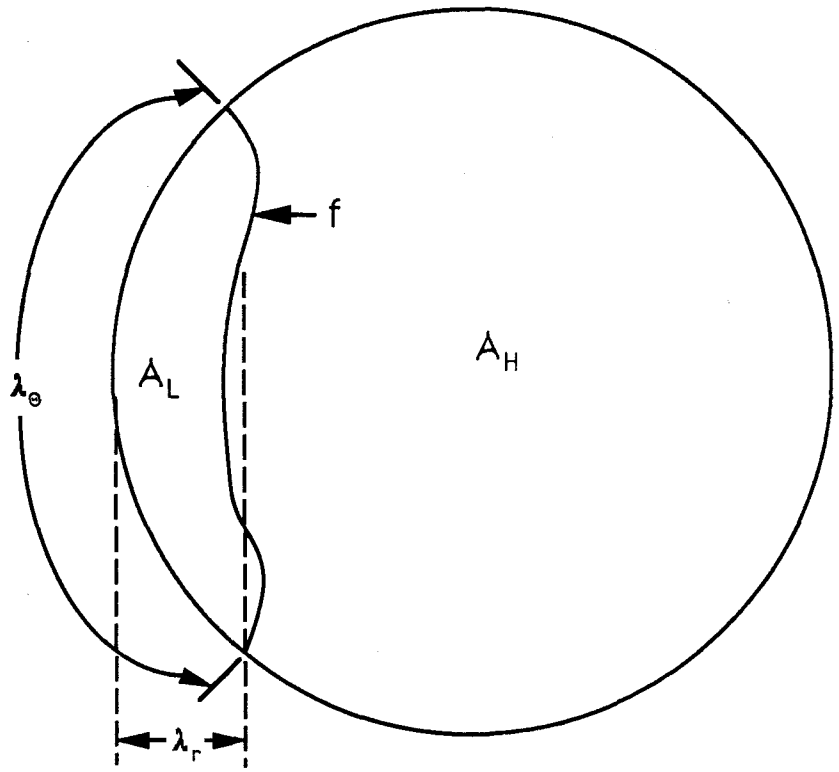

Figure 4.2 Schematic Showing the Relationship between the Plume Cross-Section and the Rayleigh Taylor Wave Lengths.

relationship based on the length scale, A_L/f. If the new expression for A_L/f from equation (4.2) is substituted into equation (3.2), the following result may be obtained for the critical conditions

$$Ku^2 = \frac{2}{C_{fi}} \tag{4.3}$$

In addition to this result, the Kutateladze number may be shown to emerge from the scaling analysis by changing the length scale in equation (1.9) from D to $(\sigma/\Delta\rho g)^{1/2}$. When this substitution is made, the resulting momentum expression becomes

$$\overline{V_{z*}}\frac{\partial \overline{V_{z*}}}{\partial z_*} = \frac{1}{Ku^2}\Delta\rho_* - \frac{1}{r_*}\frac{\partial (r_*\overline{V_{r*}'V_{z*}'})}{\partial r_*} - \frac{1}{r_*}\frac{\partial (\overline{V_{\theta*}'V_{z*}'})}{\partial \theta_*} \tag{4.4}$$

where the friction factor term has been neglected for the reasons discussed in section 2.2.1.

These results show that identical scaling parameters govern the backflow and flooding problems. Since the relevant length scales are also identical, the two problems are therefore analogous. As a consequence of this analogy, a length scale transition is expected in the backflow problem with increasing pipe diameters, making each length scale

significant within a separate scaling range.

4.3 Full Scale Behavior

Having resolved the length scale dilemma, the problem of full scale behavior may now be addressed. In this regard it should first be noted that the length scale transition divides the scaling range into separate and unrelated regimes. This division, in turn, subjects the scaling behavior to piecemeal constraints. As a consequence, the scaling may be subject to one of three separate conditions. For example, if the transition diameter exceeds the full scale diameter, the model and the prototype both lie in the Froude number scaling range, and Froude number scaling may be used. If, on the other hand, the transition diameter is less than that of the model, both systems lie in the Kutateladze scaling range, and Kutateladze scaling may be used. Finally, if the transition diameter lies between the model and prototype values, the systems lie in separate scaling ranges, making scaling impossible between them. As a consequence of these differing criteria, the determination of the scaling regime is a necessary precondition of the scaling analysis.

Unfortunately, since the transition diameter is unknown, it is impossible to determine the ranges in which the various criteria apply. As a consequence, the scaling criteria must be determined in a less precise fashion. To make this determination the critical conditions derived in chapter 3 may

first be compared to Theofanous'[5] results for a 1/2 scale system. If this comparison shows the two systems to scale on the basis of the Froude number; it may then be concluded that the transition occurs above 1/2 scale, making scaling to larger systems uncertain. If both systems scale on a Kutateladze basis, however, it may be concluded that the transition occurs below 1/5 scale, ensuring Kutateladze scaling over the complete range. Finally, if the two results do not scale, then the transition point lies between 1/5 and 1/2 scale, making Kutateladze scaling appropriate above 1/2 scale.

To determine which of the three cases exists, it is first necessary to obtain the critical Froude and Kutateladze numbers for both the 1/5 and 1/2 scale systems. With regard to the Froude numbers, equation (3.5) gives a critical value of .65 for the 1/5 scale system. For the 1/2 scale system a value of .5 was reported by Theofanous[5]. In addition, since the Kutateladze number is simply the square root of a Froude number based on a Rayleigh Taylor wave length, the critical Kutateladze numbers may be determined from the critical Froude numbers by the following equation.

$$Ku^2 = Fr\frac{D}{\lambda_{RT}} \qquad (4.5)$$

To apply this equation it is necessary to obtain the injection diameter and the Rayleigh Taylor wave length for each system.

The diameters of the 1/5 and 1/2 scale systems were 5.08 cm and 10.8 cm respectively. In addition, the Rayleigh Taylor wave lengths may be obtained from the quantity, $(\sigma/\Delta\rho g)^{1/2}$, as mentioned previously.

To evaluate this quantity it is necessary to obtain the surface tension between salt and fresh water as a function of the density difference. Unfortunately, since these two fluids are miscible, the interface between them is hard to define, and the surface tension can only be approximated. To obtain these approximate values the surface tension of salt water with respect to a third substance may be subtracted from the equivalent fresh water value. Since the Handbook of Chemistry and Physics[17] lists surface tensions between water and air as a function of salt concentration, these subtractions may be performed over the full range of salt concentrations and plotted against the density difference. When these calculations are performed, a linear relationship between the surface tension and the density difference is obtained as shown in Figure 4.3. Since the ratio of σ to $\Delta\rho$ is therefore constant, a single value of .221 cm may be obtained for the Rayleigh Taylor wave length, independent of the density difference between the two fluids and therefore identical in both systems. Using this number, the critical values of Ku^2 may be determined as 14.94 and 24.32 for the 1/5 and 1/2 scale systems respectively.

To determine the scaling criteria, the three conditions mentioned previously must each be tested with respect to the

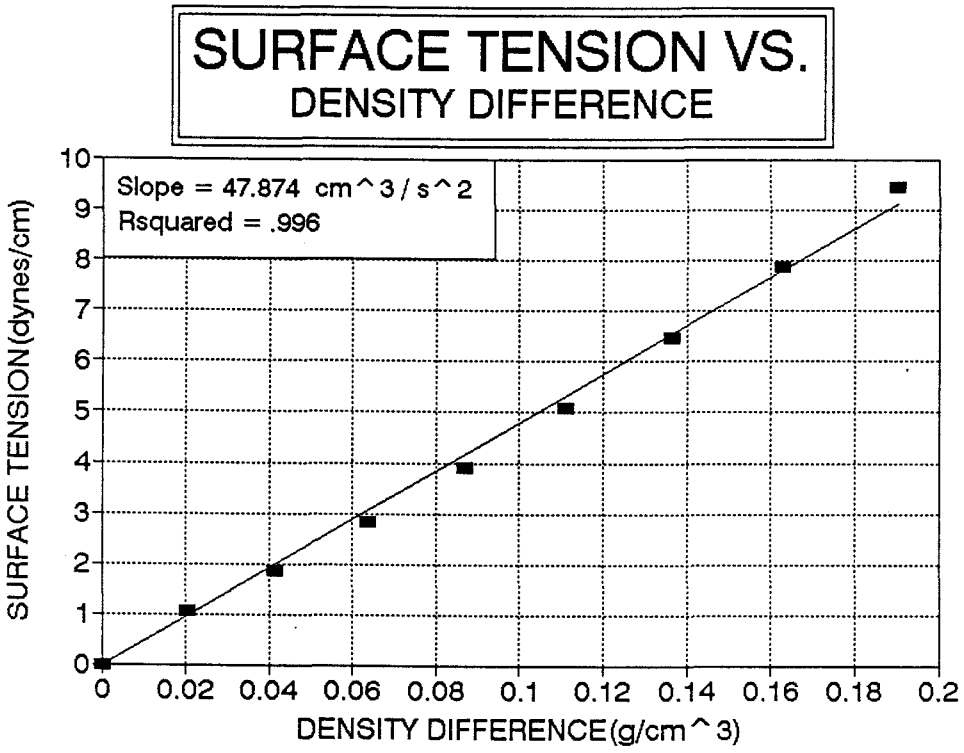

Figure 4.3 The Linear Dependence of the Surface Tension between Salt Water Solutions of Differing Concentration on the Density Difference.

experimental data. To make these comparisons the 1/5 and 1/2 scale data have been plotted as solid points in Figure 4.4. In addition, curves corresponding to the three scaling criteria have also been included. Of these curves the solid and dashed ones represent constant Froude number and Kutateladze scaling relationships based on the critical values of the 1/5 scale system. They are therefore defined by the relations; Fr = .65, and Ku^2 = 14.94; and necessarily pass through the first data point. The dotted curve, on the other hand, represents the possibility of a scaling transition between the two systems and is therefore based on the critical Kutateladze value of the 1/2 scale system. As a consequence, it is defined by the relation, Ku^2 = 24.32, and passes through the second data point. The cross hatched curve serves as a general example of higher value Kutateladze curve which will be used to illustrate a trend only. Its numerical value is therefore irrelevant.

By comparing the data points to these curves, the relevant scaling criteria may be determined. First, since the Froude numbers of the two systems are close in value, it is clear that Kutateladze scaling does not apply. As a consequence, the systems either scale on a Froude number basis, or a scaling transition occurs between them. If the latter condition holds, the critical conditions will first follow the horizontal line and then switch to the dotted curve at the intersection point (transition point) with increasing scale. If the former condition holds, however, two results

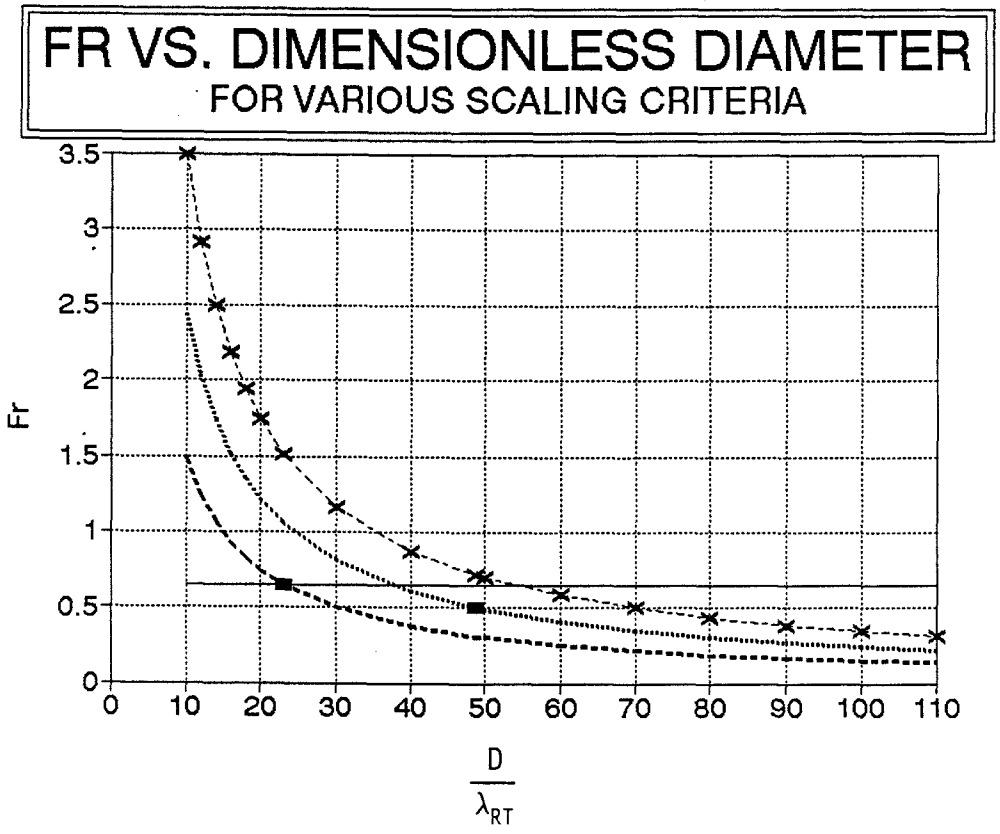

Figure 4.4 Comparison of 1/5 and 1/2 Scale Data with Several Scaling Criteria.

are possible. Either Froude number scaling will apply over the whole range, or a scaling transition will occur between 1/2 and full scale. In the first case the critical conditions will follow the horizontal line over the complete range. In the second, they will switch to a different curve at some intersection point above 1/2 scale. If this transition is represented by the cross hatched curve, it is clear that all transitions above 1/2 scale must fall between the horizontal line and dotted curve. As a consequence, the dotted curve may be taken as the lower bound for the critical conditions while the upper curve provides the most conservative estimate.

To determine the criticality of full scale injection flow rates, it is necessary to compare the injection Froude numbers to both of these curves. Unfortunately, due to the limited surface tension data available, the Rayleigh Taylor wave lengths cannot be obtained for reactor injection conditions. Since these wave lengths are needed to determine the dimensionless diameter, it impossible to plot the full scale injection data on this graph. In spite of this short coming, it may be seen from Table 2.2 that many of the full scale Froude numbers lie beneath the dotted curve and that all but one lie beneath the horizontal line. Thus, the reactor injection rates are subcritical over some or all of the transient, depending on the criteria used. To eliminate this ambiguity a single scaling criteria must be chosen. Since the horizontal line represents the most conservative scaling assumption, it forms the safest standard for comparison. On

this basis, therefore, the reactor injection rates should be considered subcritical throughout the duration of the transient.

Having shown full scale injection to be subcritical, it remains to evaluate the extent of penetration. In this regard, it was mentioned in section 3.4 that equation (3.14) properly predicts the extremes and intermediate trends of the backflow behavior. Given this result and its sound physical derivation, an equation of this form would be expected to hold for any pipe diameter with a probable change in the constant, k. The reason for the change in the constant may be determined by inspection from the expression for k.

$$k = \frac{A_L}{\epsilon f D} \tag{4.6}$$

As can be seen from this equation, k involves a ratio of A_L/f to the pipe diameter. Since it is known from the previous discussion that these two length scales are independent, it is obvious that k will vary as the diameter changes. For this reason the extent of full scale penetration cannot be determined without additional research.

CHAPTER 5

CONCLUSIONS

5.1 Research Results

To place the results of the preceding chapters within a proper context, it is necessary to review both the scope and the limitations of this research. In this regard, it was mentioned in chapter 1 that two plants had experienced injection line cracking as a result buoyant backflow in the HPI lines. Since the potential consequences of this cracking could have been serious, it was decided to determine whether backflow would pose a problem during a SBLOCA. For this reason it was the objective of this research to determine the critical conditions and the subcritical penetration behavior of buoyant backflow for turbulent injection flow rates. The analysis was simplified by assuming the cold leg to remain stagnant and by ignoring the material effects.

As a first step in this investigation, a series of reactor flow experiments was run on a 1/5 scale model of a reactor HPI, cold leg, and downcomer. In these experiments the injection velocity and fractional density difference, $\Delta\rho/\rho$, were independently and systematically varied to determine the effect of each on the penetration behavior. As a result of these tests, two significant trends were observed. First, buoyant backflow began below a critical injection

velocity which increased with $\Delta\rho/\rho$. Second, for subcritical velocities the depth of penetration increased with decreasing injection rates. The details of these experiments are described in chapter 2.

The experimental results were theoretically analyzed in chapter 3. First, the critical conditions were obtained through a friction-buoyancy balance on intruding plumes showing penetration to begin below a critical Froude number of .65. Next, the relationship between the penetration depth and the injection velocity was derived on the basis of mass conservation within the plume. As a result of this analysis, the penetration depth was shown to vary with the negative logarithm of the injection velocity in the subcritical range. In both of these cases, the theoretical relationships were derived in terms of experimental proportionality constants and matched to the experimental data. In each instance close agreement between theory and experiment was demonstrated.

Once the backflow behavior was theoretically modeled, an attempt was made in chapter 4 to scale the results to full size. In extending these results it was recognized that the presence of two dissimilar length scales in the problem would produce conflicting scaling criteria. To resolve this conflict an analogy was drawn between the problems of buoyant backflow and reactor flooding, showing the scaling of the critical conditions to switch from Froude number to Kutateladze scaling with increasing pipe diameters. Since the transition diameter was unknown, however, the correct choice

could not be determined.

To resolve this difficulty, the critical conditions obtained in the analysis were scaled on the basis of both criteria. By comparing these values to the full scale data and to one another, two results were obtained. First, the full scale injection rates were found to be subcritical with respect to both criteria, establishing the presence of backflow in certain reactor systems. In addition, the Froude number was shown to be the more conservative of the two scaling parameters. Because of this conservatism, the Froude number was adopted as the standard of comparison. On this basis full scale injection was shown to be subcritical over the complete range of flow rates for a certain class of reactor systems.

5.2 Suggestions for Future Research

Since full scale injection flow rates are subcritical in certain systems, buoyant backflow is present during high pressure injection. As a consequence of this result, further studies are needed to evaluate its significance. In performing these investigations initial studies should determine the effects of several parameters neglected in this analysis. Among these are the effects of scale, cross flow, and the injection angle. Moreover, as each of these effects is included, the backflow behavior should be examined in greater depth to reveal significant underlying effects.

Finally, if the results of these studies show backflow to be significant in full scale systems, the material effects should then be analyzed. The outlines of these studies will now be presented.

The first factor that should be investigated is the effect of scale on the penetration behavior. By analogy to the present study, the first step in this investigation should be to experimentally determine the effects of scale on both the critical conditions and the penetration depth. Once this data is obtained, the impact of scale on the critical conditions should be analyzed to determine the scaling transition point and to more accurately assess the criticality of full scale injection rates. If these injection rates are found to be subcritical, the effect of scale on the penetration depth should then be determined to evaluate the significance of the full scale penetrations.

If these studies show backflow to be significant at large scales, the effect of crossflow should next be studied. The purpose of these investigations should be to experimentally and theoretically determine the effect of increasing cross flow velocities on the penetration behavior. Based on the observations of Ernst[6], cross flow is expected to encourage backflow by bending the emerging jet and causing the injected fluid to prematurely separate from the upstream lip of the HPI. However, according to the same author, crossflow may have the opposite effect at high velocities and actually suppress penetration. If this suppression should prove

significant, buoyant backflow may be eliminated from a wide range of transients, greatly reducing its significance.

If backflow should remain significant, however, the effect of injection angle should then be determined. From the studies of Wilkinson[4], the effect of decreasing the injection angle should be to increase the penetration depth and possibly stabilize the penetration against the upper wall of the injection line. Depending on the degree of stabilization, this effect could have differing impacts on the HPI piping. If the resulting stabilization were absolute, a single penetration would simply maintain itself in steady state against the upper wall of the injection line. Since the cyclic nature of backflow would be eliminated, the resulting fatigue would be greatly reduced. If, on the other hand, the increase in stability were only marginal, the penetrations would persist longer, but their cyclic nature would remain unchanged. In this case the enhancement of both penetration depth and contact time would increase the heat transfer to the wall and, consequently, the damage per cycle. Since thermal fatigue increases with both the severity and frequency of the cycles, the net result of this effect might be to increase the damage in the injection line. For those reactors that inject at 45° and 60° angles, these effects should be investigated.

In conjunction with each of these studies, the penetration behavior in the pipe should be examined in detail. To make these detailed studies sensitive equipment should be employed so that in addition to the penetration depth; the

boundary layer thickness, the turbulent intensity, and the cross-sectional shape of the plume are also determined. Once these quantities have been obtained, they should then be interrelated with each other and the parameter being studied. As a result of this process, the effect of any given parameter on buoyant penetration may be more readily analyzed. For example, through this process the total effect of scale on the penetration depth could be analyzed in terms of its component effects on other related parameters. Obviously, in addition to scale, the effects of cross flow and the injection angle could also be more comprehensively investigated.

Of particular interest in these investigations, would be the effect of the boundary layer thickness on the depth of penetration. In this regard there are two possible reasons why the boundary layer may effect the penetration depth. First, the boundary layer thickness may determine the radial dimension of the plume and therefore directly determine its cross-sectional area. Second, if the boundary layer does not limit the radial dimension of the plume, the ratio of this dimension to the boundary layer thickness will then determine the degree of turbulence at the interface. Thus, boundary layer reduction may decrease the penetration depth by either reducing the cross-sectional area or increasing the interfacial turbulence. To devise effective methods of suppressing penetration, the correct relationship should be determined.

Finally, if these studies show full scale penetration to

be significant, the material effects should then be investigated. To perform such an investigation, a higher scale model should be constructed with conductivity probes imbedded in the glass and made to protrude at regular nodal points into the HPI. These probes may then be used to obtain the time varying concentrations at several grid points on the HPI wall. By transmitting these values to a data base, the time varying concentrations may be converted to equivalent temperatures to establish a time dependent, wall, temperature, boundary condition. From this boundary condition the internal temperatures of the piping may be determined through a heat transfer analysis to yield the thermal fatigue per unit time as a function of several flow parameters. To obtain the cumulative fatigue, this parameter would then be integrated over several reactor transients, and weighted by their probabilities of occurrence. The resulting value could then be compared to a yield value for the material to determine the significance of the material effects. Obviously, since salt cannot model the heat conduction at the wall, such an analysis would necessarily be approximate.

BIBLIOGRAPHY

1. Rossi, C.E., "Thermal Stresses in Piping Connected to Reactor Coolant Systems," NRC BULLETIN NO. 88-08, OMB NO.:3150-0011, 1988.

2. Rossi, C.E., "Thermal Stresses in Piping Connected to Reactor Coolant Systems," NRC BULLETIN NO. 88-08, SUPPLEMENT 1, OMB NO.:3150-0011, 1988.

3. Jörg, O. and Scorer R.S., "An Experimental Study of Cold Inflow into Chimneys," Atmos. Environ., Vol. 1, p 645, 1967.

4. Wilkinson, D.L., "Advance of Seawater Intrusion into Ports of Ocean Outfalls," J. Hydr. Engr., Vol. 114, p 1815, 1988.

5. Theofanous, T.G., Iyer, K., Nourbakhsh, N.H., and Gherson, P. Buoyancy Effects in Overcooling Transients Calculated for the NRC Pressurized Thermal Shock Study, NUREG/CR-3702, May 1986.

6. Ernst, G., "Cooling Towers, Design and Plume Behavior," Seminar of International Centre Heat and Mass Transfer, Dubrovnik, 1975.

7. Baer, E., Ernst, G., Wurz, D., "Untersuchung zur Schwadenströmung in den Kronen von Naturzugkühltürmen," VDI Kühlturmseminar, Düsseldorf, May 25, 1977, Inst. f. Technische Thermo., U. Karlsruhe.

8. Moore, F.K., and Torrance, K.L., "Air Flow in Dry Natural-Draft Cooling Towers Subject to Wind," Report to ERDA, Cornell University, Dec. 8, 1977.

9. Moore, F.K., "Cold Inflow and Its Implications for Dry Tower Design," Proceedings of the 2nd Conference on Waste Heat Management and Utilization, University of Miami, Miami Beach, Florida, Dec. 4-6, 1978.

10. Moore, F.K., and Garde, M.A., "Aerodynamic Losses of Highly Flared Natural Draft Cooling Towers," Proceedings of a Waste Heat Congress, University of Miami, Miami Beach, Florida, May 11-13, 1981.

11. Dayal, A., Theoretical and Experimental Study of Cold Inflow in Natural Draft Cooling Towers, M.S. Thesis, Cornell University, Ithaca, N.Y., 1981.

12. Wynne, M.J., Experimental Study of a Natural Draft Cooling Tower with Emphasis on Cold Inflow at Exit, M.S. Thesis, Cornell University, Ithaca, N.Y., 1979.

13. Modi, V., A Study of Laminar Separation in Buoyant Channel Flows, Ph.D. Thesis, Cornell University, Ithaca, N.Y., pp 175, 1984.

14. Trojan Nuclear Power Plant Final Safety Analysis Report, Volume 8., Portland General Electric Company, Docket No. 50-344, as amended, July, 1974.

15. Alberthal, G., "SI Flow Reduction Calculations," TNP-85-11, Portland General Electric Company, April, 1985.

16. Steam/ Its Generation and Use, Babcock and Wilcox Company, N.Y., N.Y., 1975.

17. Weast, R. C., Editor, CRC Handbook of Chemistry and Physics, 67th Edition, CRC Press Inc., Boca Raton, Fl. 1986

18. Chandrasekhar, S., Hydrodynamic and Hydromagnetic Stability, Dover Publications, Inc., New York, 1981.

19. Beckner, W.D., J.N. Reyes and R. Anderson, Analysis of Emergency Core Cooling Bypass Data, NUREG-0573, July 1979.

20. Delhaye, J.M., Giot, M., Riethmuller, M.L., Thermohydraulics of Two-Phase Systems for Industrial Design and Nuclear Engineering, Hemisphere Publishing Corporation, New York, 1981.

APPENDICES

APPENDIX I

NRC DOCUMENTS VERIFYING

INJECTION LINE CRACKING

OMB No.: 3150-0011
NRCB 88-08

UNITED STATES
NUCLEAR REGULATORY COMMISSION
OFFICE OF NUCLEAR REACTOR REGULATION
WASHINGTON, D.C. 20555

DUKE COCKFIELD

JUL 5 1988

June 22, 1988

NRC BULLETIN NO. 88-08: THERMAL STRESSES IN PIPING CONNECTED TO REACTOR COOLANT SYSTEMS

Addressees:

All holders of operating licenses or construction permits for light-water-cooled nuclear power reactors.

Purpose:

The purpose of this bulletin is to request that licensees (1) review their reactor coolant systems (RCSs) to identify any connected, unisolable piping that could be subjected to temperature distributions which would result in unacceptable thermal stresses and (2) take action, where such piping is identified, to ensure that the piping will not be subjected to unacceptable thermal stresses.

Description of Circumstances:

On December 9, 1987, while Farley 2 was operating at 33 percent power, the licensee noted increased moisture and radioactivity within containment. The unidentified leak rate was determined to be 0.7 gpm. The source of leakage was a circumferential crack extending through the wall of a short, unisolable section of emergency core cooling system (ECCS) piping that is connected to the cold leg of loop B in the RCS. This section of piping, consisting of a nozzle, two pipe spools, an elbow, and a check valve, is shown in Figure 1. The crack resulted from high-cycle thermal fatigue that was caused by relatively cold water leaking through a closed globe valve at a pressure sufficient to open the check valve. The leaking globe valve is in the bypass pipe around the boron injection tank (BIT) as shown in Figure 2. During normal operation this valve and others isolate the ECCS piping from the discharge pressure of the charging pumps. With a charging pump running and the valve leaking, temperature stratification occurred in the ECCS pipe as indicated in Figure 1. In addition, temperature fluctuations were found at the location of the failed weld with peak-to-peak amplitudes as large as 70 degrees F and with periods between 2 and 20 minutes.[1]

1/ The staff has learned recently of a problem discovered at Trojan in the pressurizer surge line which involved excessive stresses due to thermal stratification. The staff believes that common elements may exist between the Farley 2 event which necessitated this bulletin and the observations at Trojan. The need for an additional generic communication is being considered as part of our ongoing evaluation of the Trojan event.

Copies to: Cockfield, Yundt, Walt, Olmstead, Roller, Burton, Lehigh, Mazurkiewicz, LIS, Erickson, Hoag, Rupe, Lentsch, Sautter, R. Johnson, Bauer, Ward, TNP:GOV REL F:NRC CHRONO, TNP:GOV REL F:NRC Bulletin 88-08

PGE Action - A. N. Roller (Due - See below) NSRD Action - S. A. Bauer
Complete Action 1 by 9/2/88. Determine additional actions, if any required. by 9/2/88. Draft response by 9/15 to Walt. Walt Action-Submit by 10/3.

Discussion:

At Farley 2, dual-purpose pumps are used for charging the RCS with coolant from the chemical and volume control system during normal operation and injecting emergency core coolant at high pressure during a loss-of-coolant accident (LOCA). Separate runs of piping from these pumps are connected to separate nozzles on the RCS piping for normal charging flow, backup charging flow, and hot- and cold-leg ECCS injection and to a nozzle on the pressurizer for auxiliary pressurizer spray. All of these runs of piping, downstream from the last check valve in each pipe, are susceptible to the kind of failure that occurred in the ECCS piping connected to the cold leg of loop B.

In any light-water-cooled power reactor, thermal fatigue of unisolable piping connected to the RCS can occur when the connected piping is isolated by a leaking block valve, the pressure upstream from the block valve is higher than RCS pressure, and the temperature upstream is significantly cooler than RCS temperature. Because valves often leak, an unrecognized phenomenon and possibly unanalyzed condition may exist for those reactors that can be subjected to these conditions. Under these conditions, thermal fatigue of the unisolable piping can result in crack initiation as experienced at Farley 2. Cracking has occurred at other plants in Class 2 systems (see IE Bulletin 79-13, "Cracking in Feedwater System Piping," dated June 25, 1979 and Revisions 1 and 2 dated August 30 and October 16, 1979, respectively). Subjecting flawed piping to excessive stresses induced by a seismic event, waterhammer, or some other cause conceivably could result in failure of the pipe.

General Design Criterion 14 of Appendix A to Part 50 of Title 10 of the Code of Federal Regulations requires that the reactor coolant pressure boundary be designed so as to have an extremely low probability of abnormal leakage, of rapidly propagating failure, and of gross rupture. At Farley 2, the pressure boundary failed well within its design life.

Actions Requested:

1. Review systems connected to the RCS to determine whether unisolable sections of piping connected to the RCS can be subjected to stresses from temperature stratification or temperature oscillations that could be induced by leaking valves and that were not evaluated in the design analysis of the piping. For those addressees who determine that there are no unisolable sections of piping that can be subjected to such stresses, no additional actions are requested except for the report required below.

2. For any unisolable sections of piping connected to the RCS that may have been subjected to excessive thermal stresses, examine nondestructively. the welds, heat-affected zones and high stress locations, including geometric discontinuities, in that piping to provide assurance that there are no existing flaws.

3. Plan and implement a program to provide continuing assurance that unisolable sections of all piping connected to the RCS will not be subjected to combined cyclic and static thermal and other stresses that could cause fatigue failure during the remaining life of the unit. This assurance may be provided by (1) redesigning and modifying these sections of piping to withstand combined stresses caused by various loads including temporal and spatial distributions of temperature resulting from leakage across valve seats, (2) instrumenting this piping to detect adverse temperature distributions and establishing appropriate limits on temperature distributions, or (3) providing means for ensuring that pressure upstream from block valves which might leak is monitored and does not exceed RCS pressure.

4. For operating plants not in extended outages, Action 1 should be completed within 60 days of receipt of this bulletin, and Actions 2 and 3, if required, should be completed before the end of the next refueling outage. If the next refueling outage ends within 90 days after receipt of this bulletin, then Actions 2 and 3 may be completed before the end of the following refueling outage.

   For operating plants in extended outages and for plants under construction, Action 1 should be completed within 60 days of receipt of this bulletin or before achieving criticality, whichever is later, and Actions 2 and 3 should be completed before achieving criticality, unless criticality is scheduled to occur within 90 days of receipt of this bulletin. In that case, Actions 2 and 3 should be completed before the end of the next refueling outage.

Reporting Requirements:

1. Within 30 days of completion of Action 1, each addressee shall submit a letter confirming that the action has been completed and describing the results of the review. If the review performed under Action 1 indicates that a potential problem exists, the confirmatory letter shall include a schedule for completing Actions 2 and 3.

2. Those addressees who determine that there are unisolable sections of piping that can be subjected to stresses from temperature stratification or temperature oscillations that could be induced by leaking valves and that were not evaluated in the design analysis of the piping shall submit a letter within 30 days of completion of Actions 2 and 3. This letter should confirm that Actions 2 and 3 have been completed and describe the actions taken.

The written reports, required above, shall be addressed to the U.S. Nuclear Regulatory Commission, ATTN: Document Control Desk, Washington, D.C. 20555, under oath or affirmation under the provisions of Section 182a, Atomic Energy Act of 1954, as amended. In addition, a copy shall be submitted to the appropriate Regional Administrator.

This requirement for information was approved by the Office of Management and Budget under clearance number 3150-0011.

If you have any questions regarding this matter, please contact one of the technical contacts listed below or the Regional Administrator of the appropriate NRC regional office.

Charles E. Rossi, Director
Division of Operational Events Assessment
Office of Nuclear Reactor Regulation

Technical Contacts: Roger W. Woodruff, NRR
(301) 492-1180

Pao Kuo, NRR
(301) 492-0907

Attachments:
1. Figure 1 - Farley 2 Temperature Data
2. Figure 2 - Farley 2 ECCS
3. List of Recently Issued NRC Bulletins

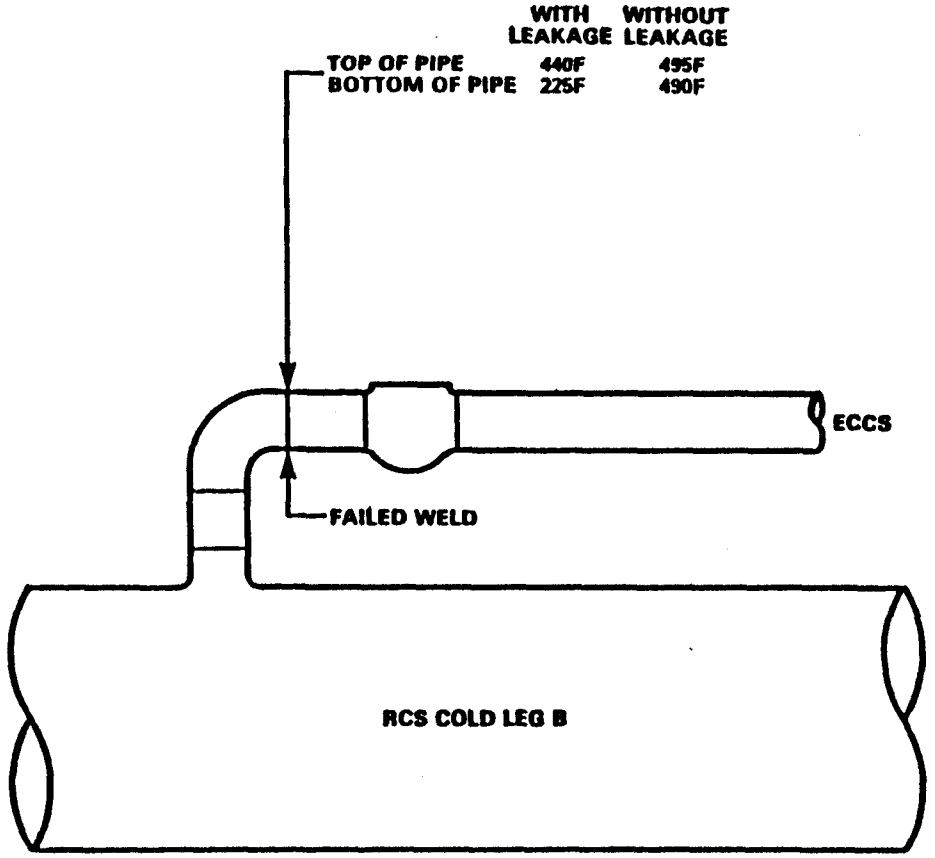

FARLEY 2 TEMPERATURE DATA

FIGURE 1

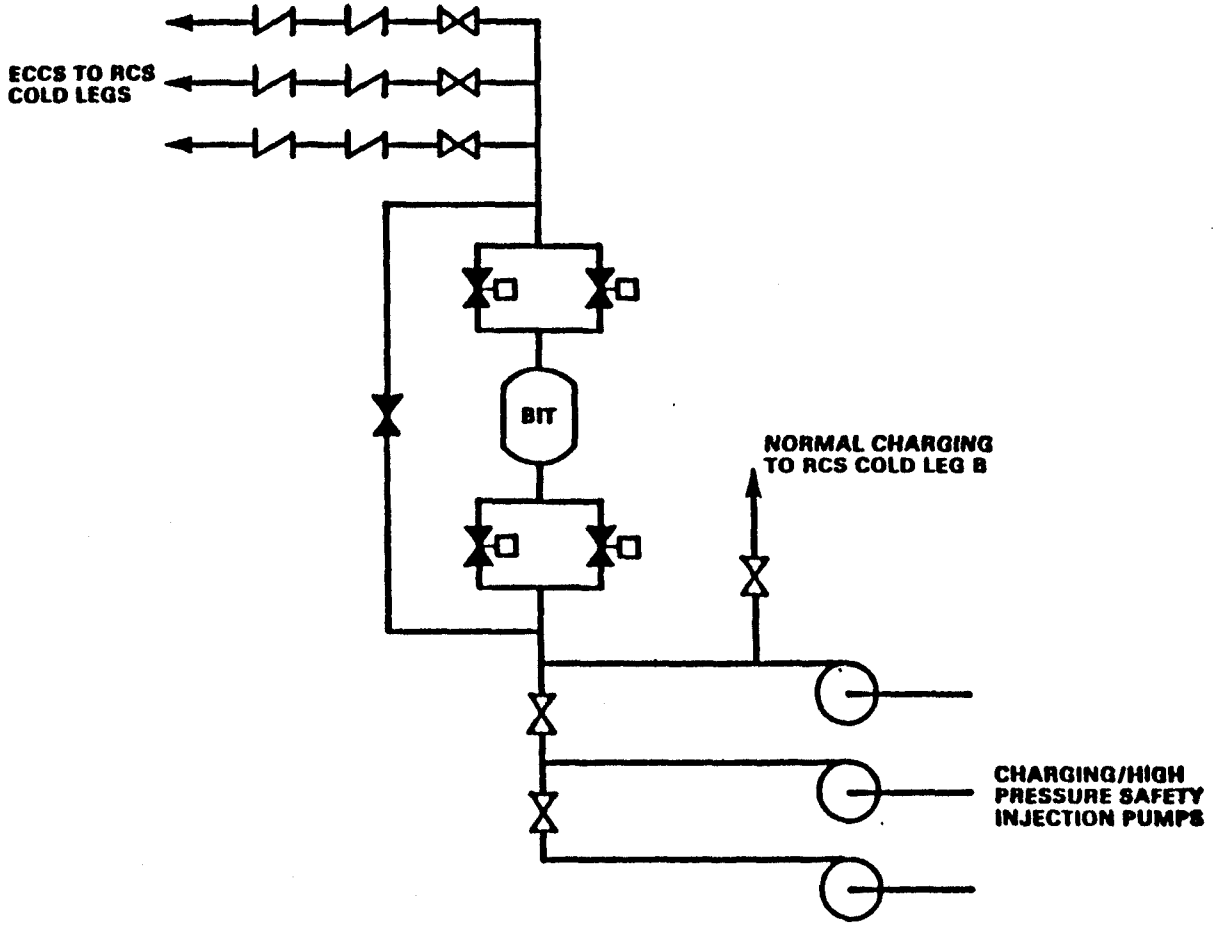

FARLEY 2 ECCS

FIGURE 2

OMB No.: 3150-0011
NRC 88-08, Supplement 1

UNITED STATES
NUCLEAR REGULATORY COMMISSION
OFFICE OF NUCLEAR REACTOR REGULATION
WASHINGTON, D. C. 20555

DUKE COCKFIELD

JUN 3 0 1988

June 24, 1988

NRC BULLETIN NO. 88-08, SUPPLEMENT 1: THERMAL STRESSES IN PIPING CONNECTED TO REACTOR COOLANT SYSTEMS

Addressees:

All holders of operating licenses or construction permits for light-water-cooled nuclear power reactors.

Purpose:

The purpose of this supplement is to 1) provide preliminary information to addressees about an event at Tihange 1 that appears to be similar to the Farley 2 event and 2) emphasize the need for sufficient examinations of unisolable piping connected to the reactor coolant system (RCS) to assure that there are no rejectable crack or flaw indications. No new requirements are included in this supplement.

Description of Circumstances:

Tihange 1 is an 870 MWe, Westinghouse-type, 3-loop, pressurized-water reactor located at Tihange, Belgium. On June 18, 1988, while the reactor was operating, a sudden leak occurred in a short, unisolable section of emergency core cooling system (ECCS) piping that is connected to the hot leg of loop 1 of the RCS. The operator noted increases in radioactivity and moisture within containment and a decrease of water level in the volume control tank. The leak rate was 6 gpm, and the source of leakage was a crack extending through the wall of the piping. The location of the crack and its orientation are shown in Figure 1.

The crack, which is in the base metal of the elbow wall and not in the weld or heat-affected zone, is 3.5 inches long on the inside surface of the elbow and 1.6 inches long on the outside surface. A crack indication also exists in the spool connecting the elbow to the nozzle in the RCS hot leg. That indication is in the heat-affected zone at the weld connecting the spool to the elbow. The indication is circumferential, extends 3.9 inches on the inner surface of the spool, and is 100 mils deep. Two smaller indications exist in the vicinity of the weld connecting the elbow to the check valve.

Farley 2 experienced one crack in a short, unisolable section of ECCS piping connected to an RCS cold leg as described in Information Notice 88-01, "Safety Injection Pipe Failure," and Bulletin 88-08. That crack, which leaked at 0.7 gpm or less, was in the heat-affected zone of the upstream elbow weld. The crack developed slowly rather than suddenly as at Tihange 1.

Copies to: Cockfield, Yundt, Walt, Olmstead, Roller, Burton, Lehigh, Mazurkiewicz, LIS, Erickson, Hoag, Rupe, Lentsch, Sautter, R. Johnson, Bauer, Ward, TNP:GOV REL F:NRC CHRONO, TNP:GOV REL F:NRC Bulletin 88-08, Suppl. 1

PGE Action - A. N. Roller (Due - See below)
Complete Action 1 (in Bulletin 88-08) by 9/2/88. Determine additional actions, if any required, by 9/2/88. Draft response by 9/15 to Walt.
Walt Action - Submit by 10/3/88.

NSRD Action - S. A. Bauer

Actions Requested:

Although the actions requested in NRC Bulletin 88-08 are unchanged, it should be noted that examinations of high stress locations would include the base metal, as appropriate.

Reporting Requirements:

The reporting requirements set forth in NRC Bulletin 88-08 remain unchanged.

If you have any questions regarding this matter, please contact one of the technical contacts listed below or the Regional Administrator of the appropriate NRC regional office.

Charles E. Rossi, Director
Division of Operational Events Assessment
Office of Nuclear Reactor Regulation

Technical Contacts: Roger W. Woodruff, NRR
(301) 492-1180

Pao Kuo, NRR
(301) 492-0907

Attachments:
1. Figure 1 - Tihange 1 Piping
2. List of Recently Issued NRC Bulletins

A - THROUGH-WALL CRACK, 3.5 INCHES LONG INSIDE, 1.6 INCHES LONG OUTSIDE

B - CRACK INDICATION, 3.9 INCHES LONG INSIDE, 100 MILS DEEP

C - TWO SMALLER INDICATIONS IN THE VICINITY OF THE WELD

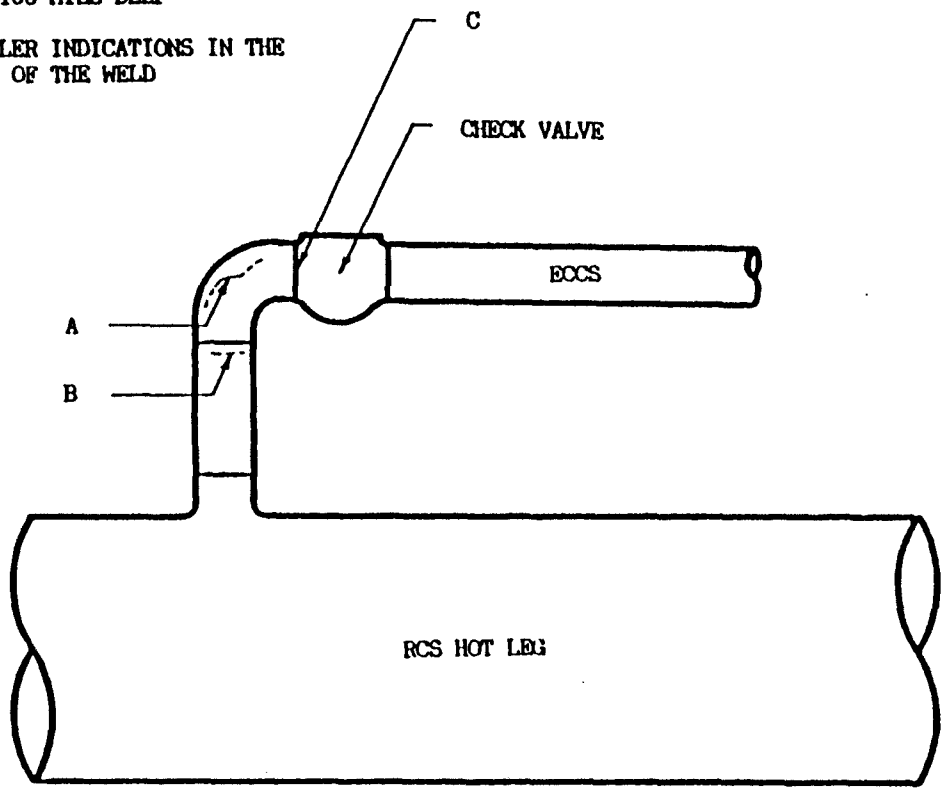

TIHANGE 1 PIPING

FIGURE 1

APPENDIX II

HISTOGRAMS OF PLUME HEIGHTS FOR THE

ONE MINUTE, CONSTANT VELOCITY TESTS

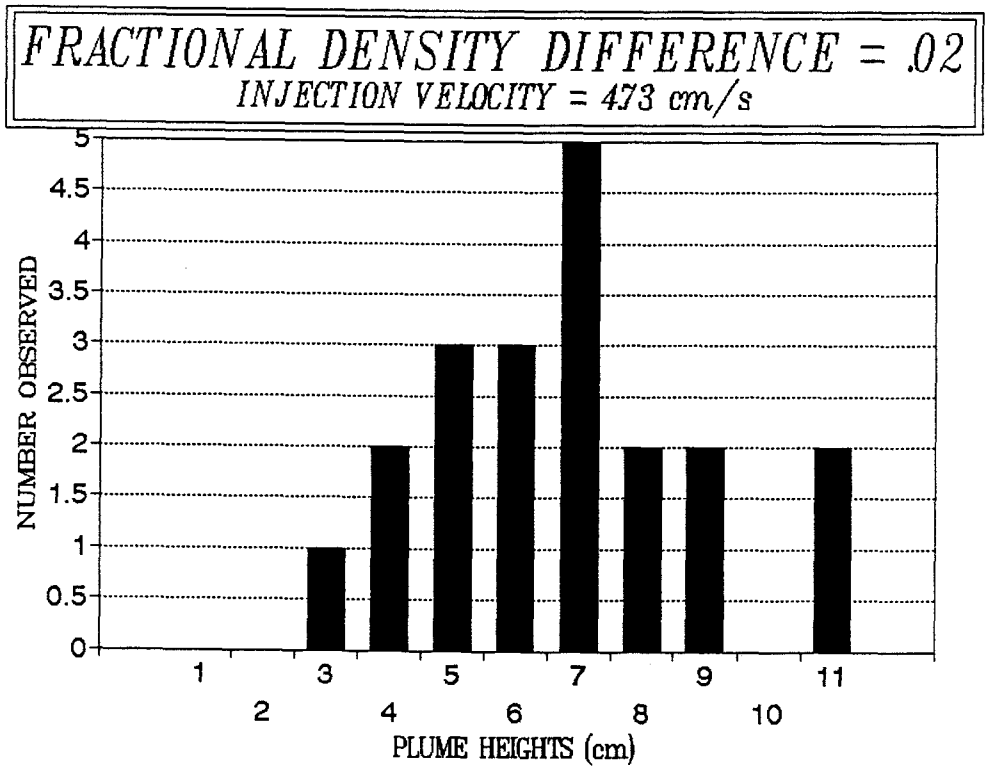
FRACTIONAL DENSITY DIFFERENCE = .02
INJECTION VELOCITY = 473 cm/s
NUMBER OBSERVED
0
0.5
1
1.5
2
2.5
3
3.5
4
4.5
5
1
2
3
4
5
6
7
8
9
10
11
PLUME HEIGHTS (cm)

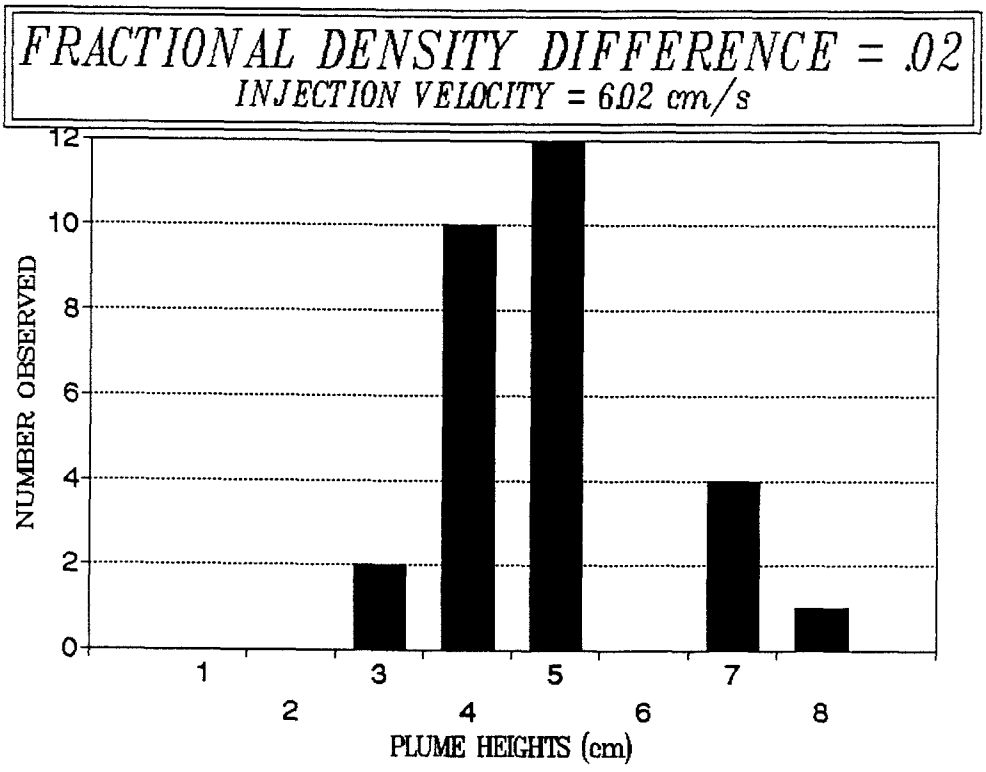
FRACTIONAL DENSITY DIFFERENCE = .02
INJECTION VELOCITY = 6.02 cm/s
NUMBER OBSERVED
0
2
4
6
8
10
12
1
2
3
4
5
6
7
8
PLUME HEIGHTS (cm)

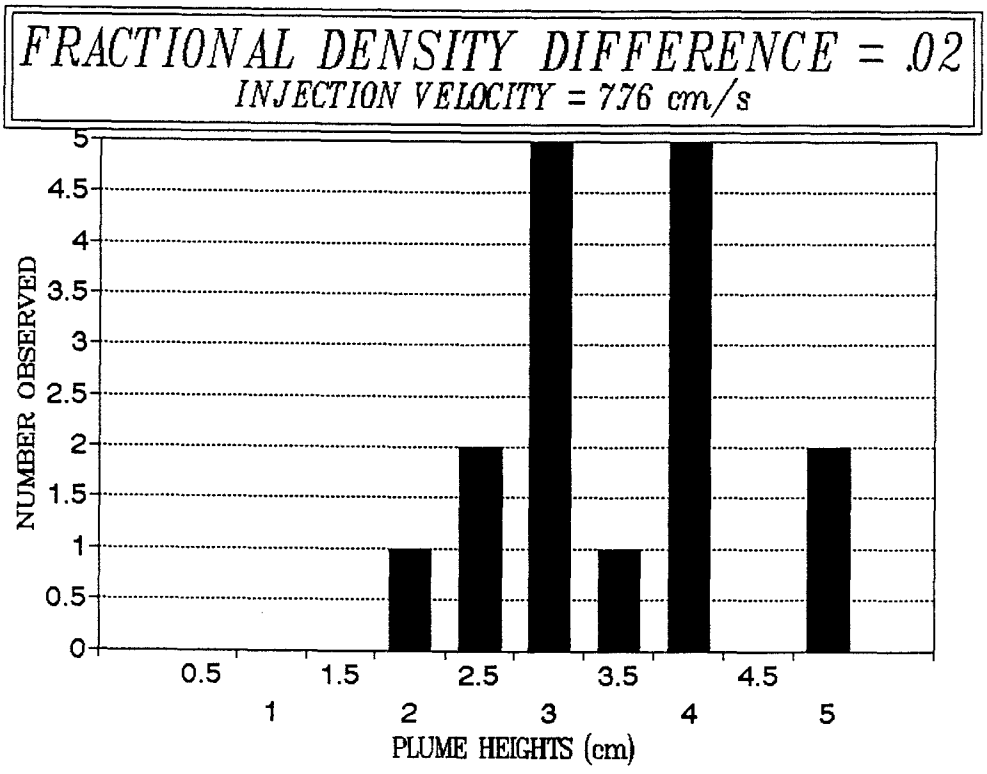
FRACTIONAL DENSITY DIFFERENCE = .02
INJECTION VELOCITY = 776 cm/s
NUMBER OBSERVED
0
0.5
1
1.5
2
2.5
3
3.5
4
4.5
5
0.5
1
1.5
2
2.5
3
3.5
4
4.5
5
PLUME HEIGHTS (cm)

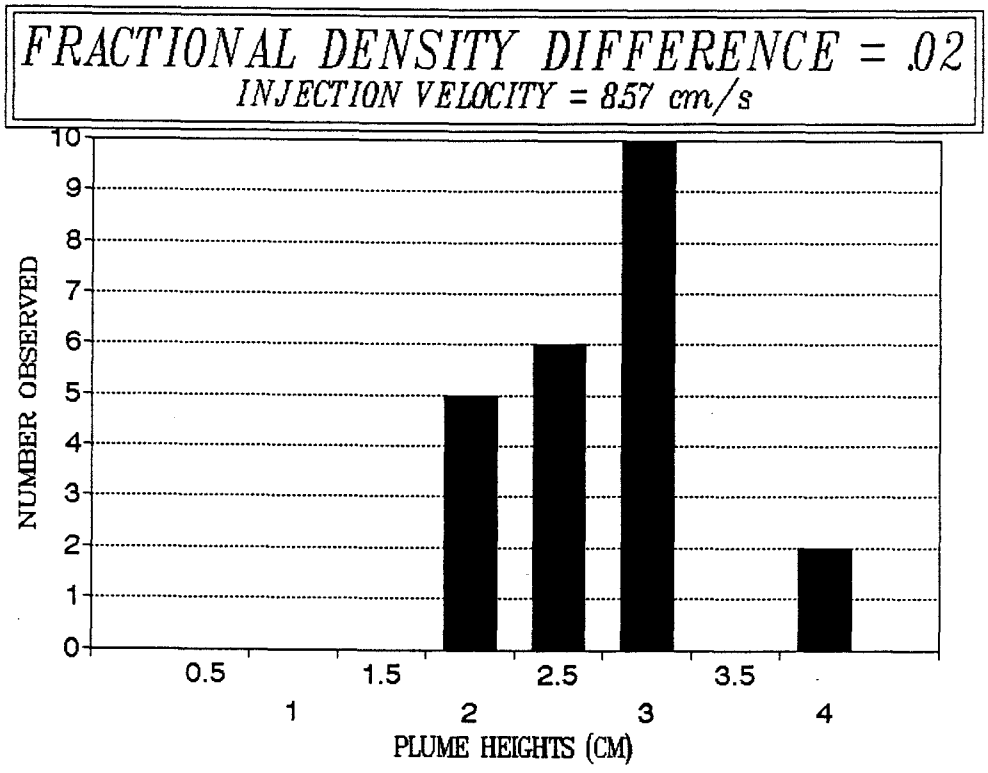
FRACTIONAL DENSITY DIFFERENCE = .02
INJECTION VELOCITY = 857 cm/s
NUMBER OBSERVED
0
1
2
3
4
5
6
7
8
9
10
0.5
1
1.5
2
2.5
3
3.5
4
PLUME HEIGHTS (CM)

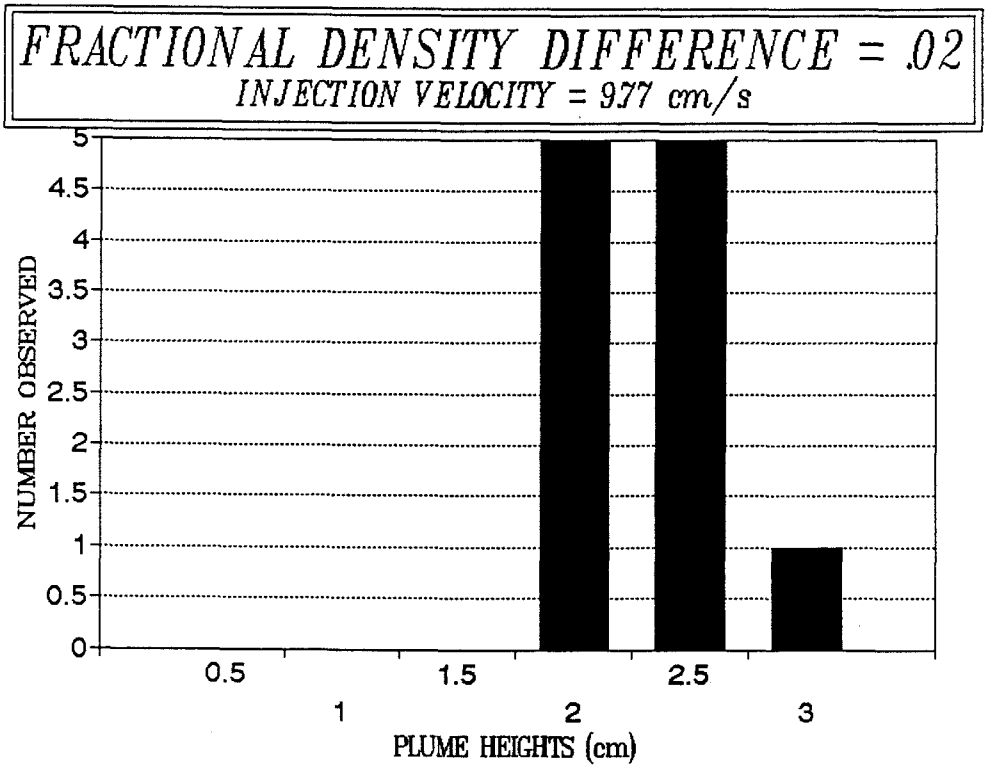
FRACTIONAL DENSITY DIFFERENCE = .02
INJECTION VELOCITY = 9.77 cm/s
NUMBER OBSERVED
0
0.5
1
1.5
2
2.5
3
3.5
4
4.5
5
0.5
1
1.5
2
2.5
3
PLUME HEIGHTS (cm)

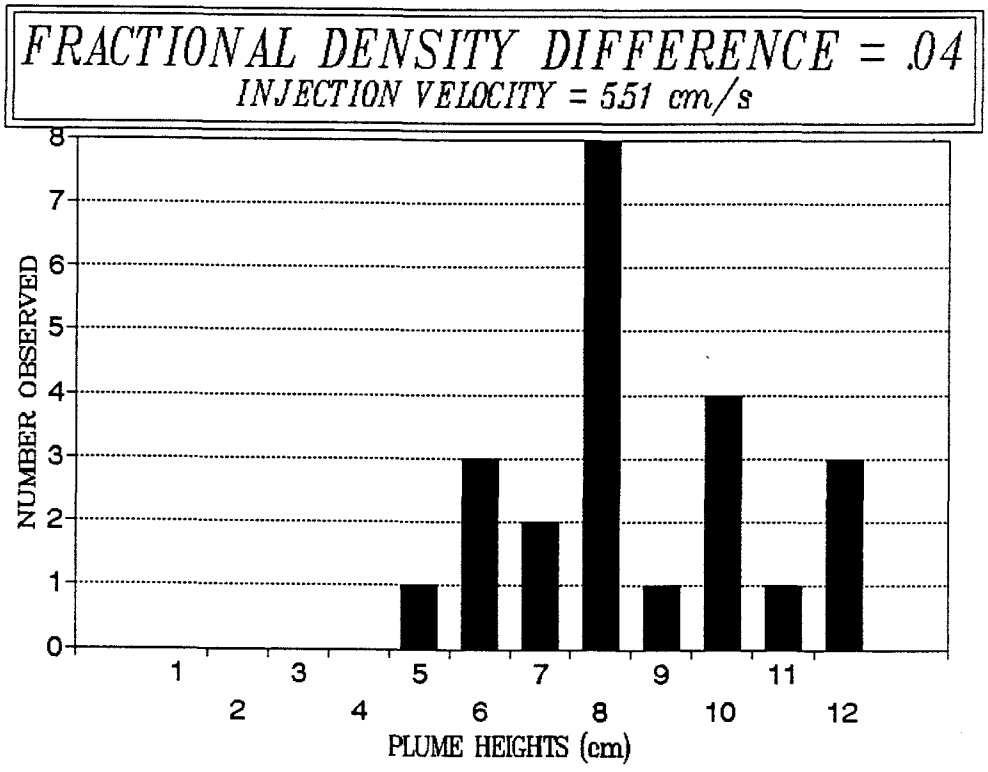
FRACTIONAL DENSITY DIFFERENCE = .04
INJECTION VELOCITY = 5.51 cm/s
NUMBER OBSERVED
0
1
2
3
4
5
6
7
8
1
2
3
4
5
6
7
8
9
10
11
12
PLUME HEIGHTS (cm)

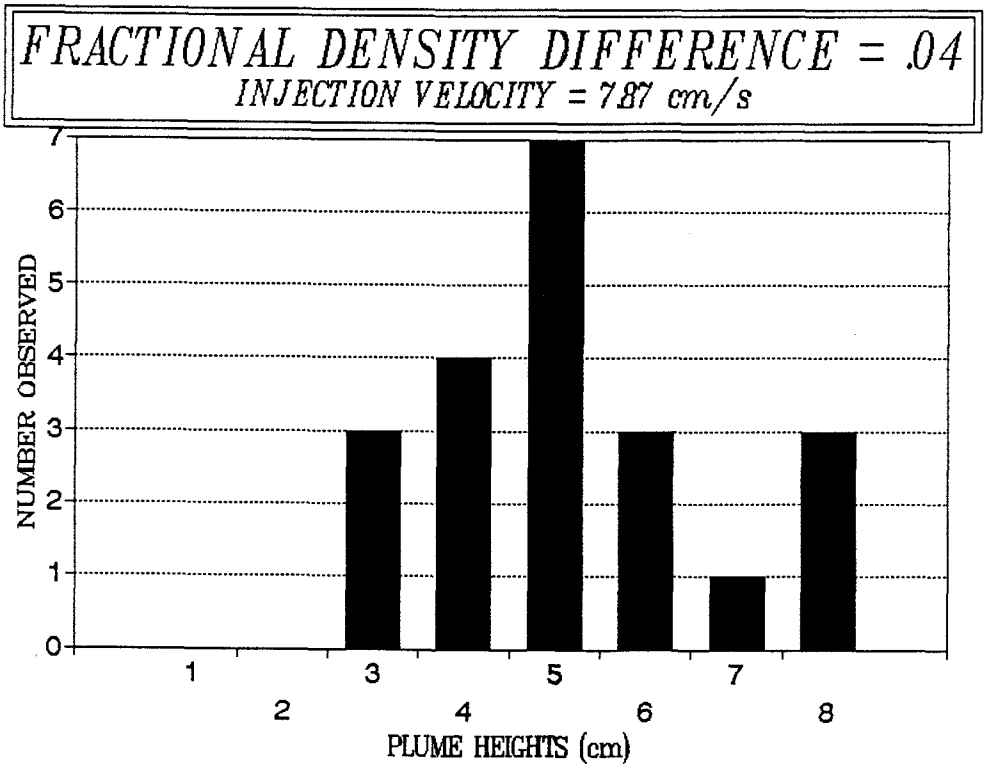
FRACTIONAL DENSITY DIFFERENCE = .04
INJECTION VELOCITY = 7.87 cm/s
NUMBER OBSERVED
0
1
2
3
4
5
6
7
1
2
3
4
5
6
7
8
PLUME HEIGHTS (cm)

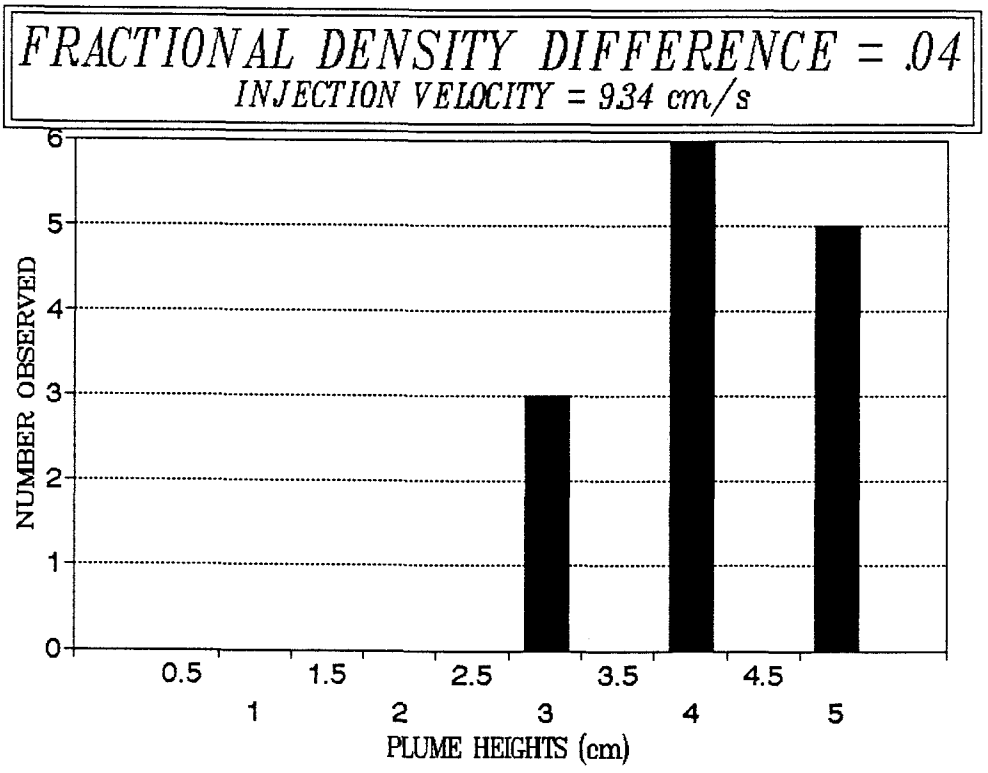
FRACTIONAL DENSITY DIFFERENCE = .04
INJECTION VELOCITY = 9.34 cm/s
NUMBER OBSERVED
0
1
2
3
4
5
6
0.5
1
1.5
2
2.5
3
3.5
4
4.5
5
PLUME HEIGHTS (cm)

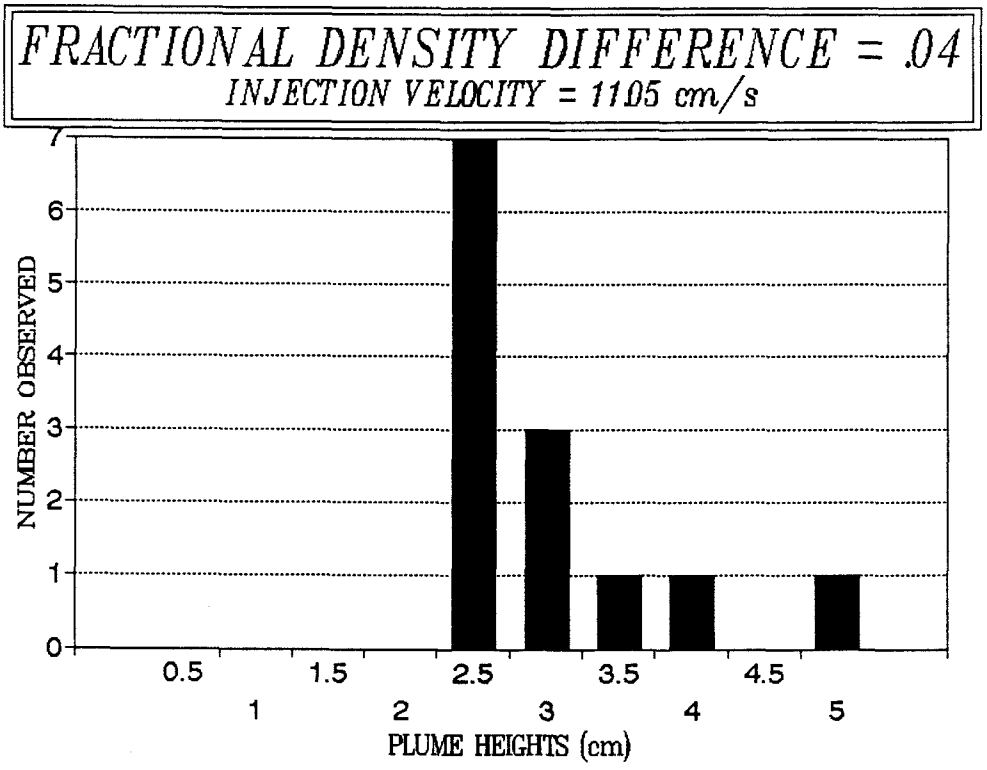
FRACTIONAL DENSITY DIFFERENCE = .04
INJECTION VELOCITY = 1105 cm/s
NUMBER OBSERVED
0
1
2
3
4
5
6
7
0.5
1
1.5
2
2.5
3
3.5
4
4.5
5
PLUME HEIGHTS (cm)

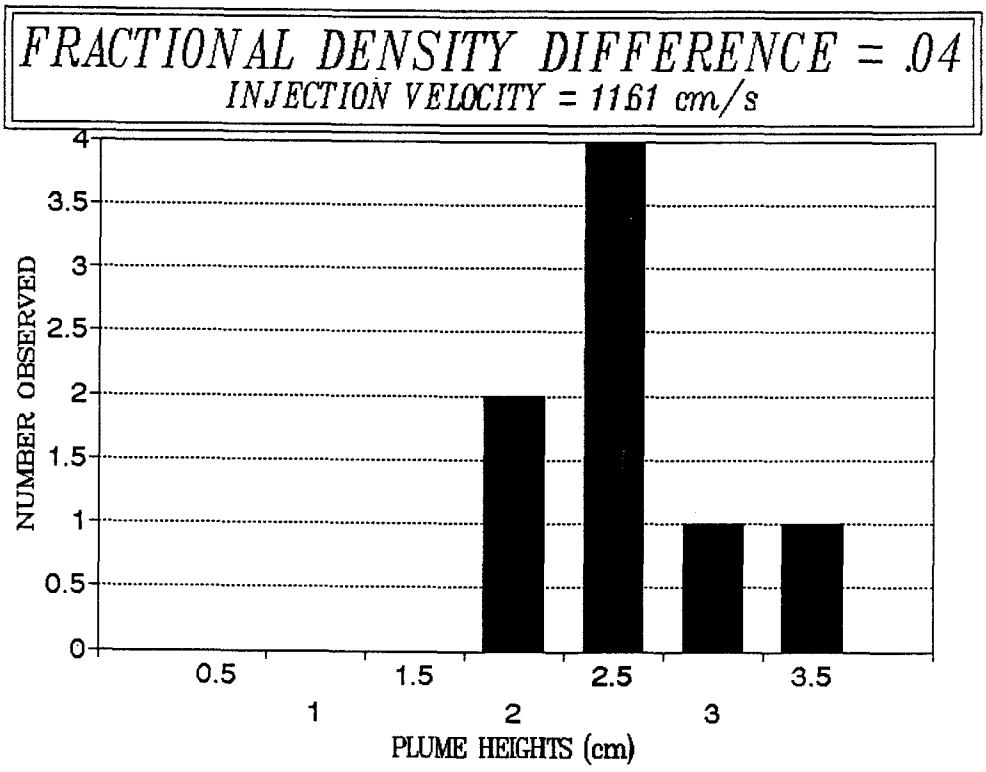
FRACTIONAL DENSITY DIFFERENCE = .04
INJECTION VELOCITY = 1161 cm/s
NUMBER OBSERVED
0
0.5
1
1.5
2
2.5
3
3.5
4
0.5
1
1.5
2
2.5
3
3.5
PLUME HEIGHTS (cm)

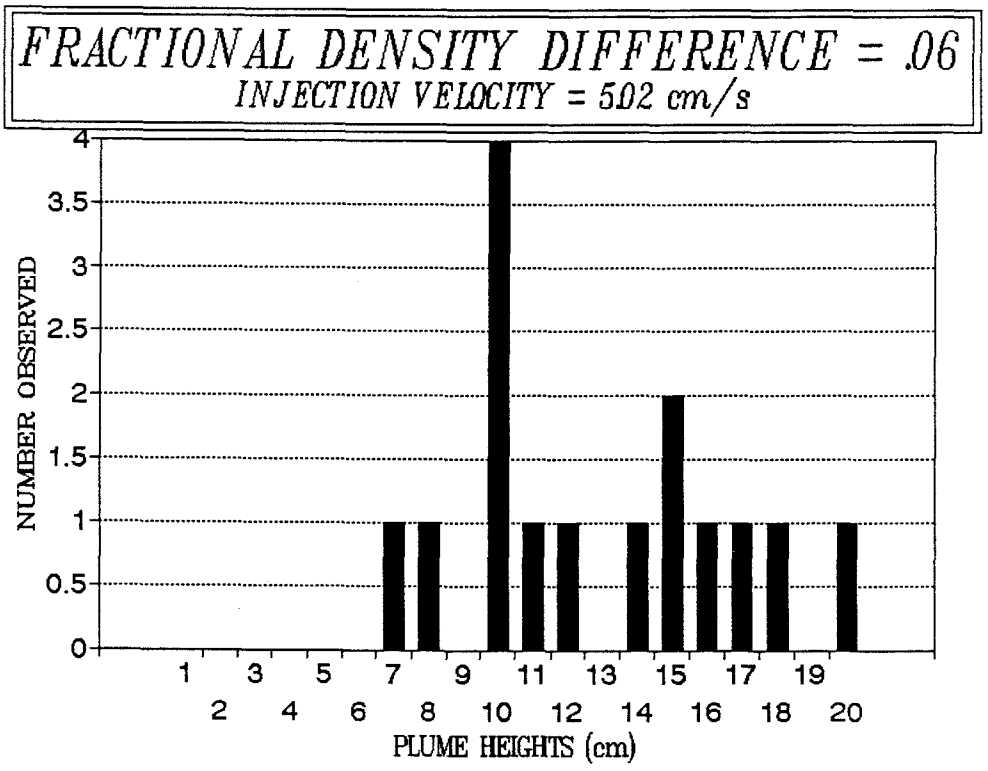
FRACTIONAL DENSITY DIFFERENCE = .06
INJECTION VELOCITY = 5.02 cm/s
NUMBER OBSERVED
0
0.5
1
1.5
2
2.5
3
3.5
4
1 2 3 4 5 6 7 8 9 10 11 12 13 14 15 16 17 18 19 20
PLUME HEIGHTS (cm)

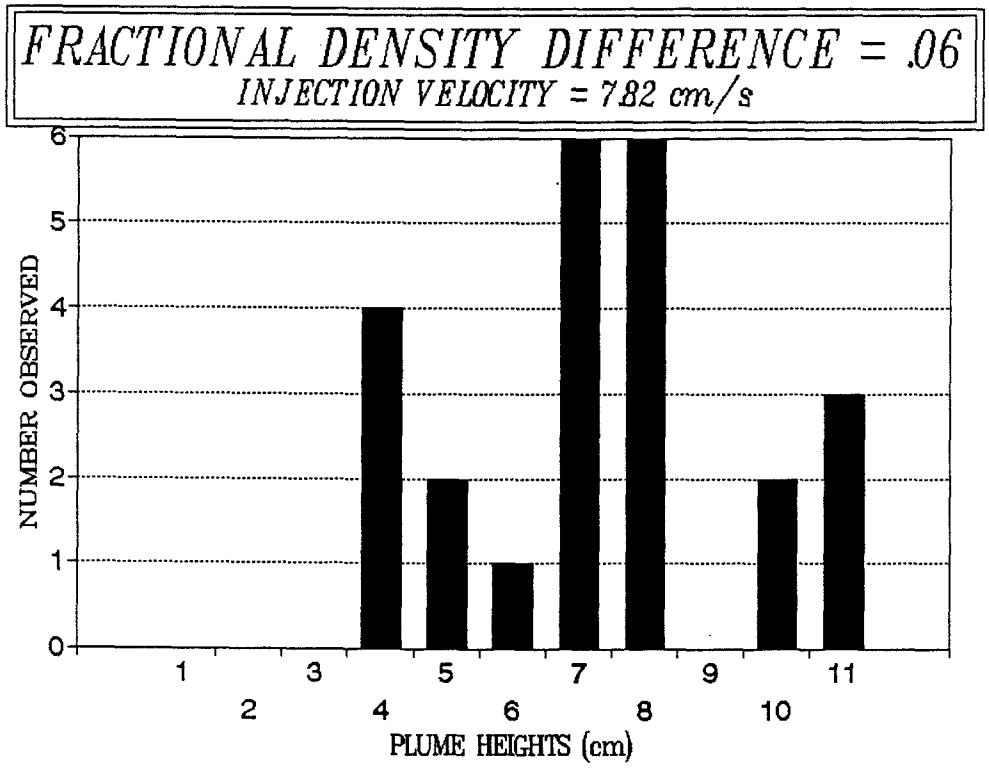
FRACTIONAL DENSITY DIFFERENCE = .06
INJECTION VELOCITY = 7.82 cm/s
NUMBER OBSERVED
0
1
2
3
4
5
6
1
2
3
4
5
6
7
8
9
10
11
PLUME HEIGHTS (cm)

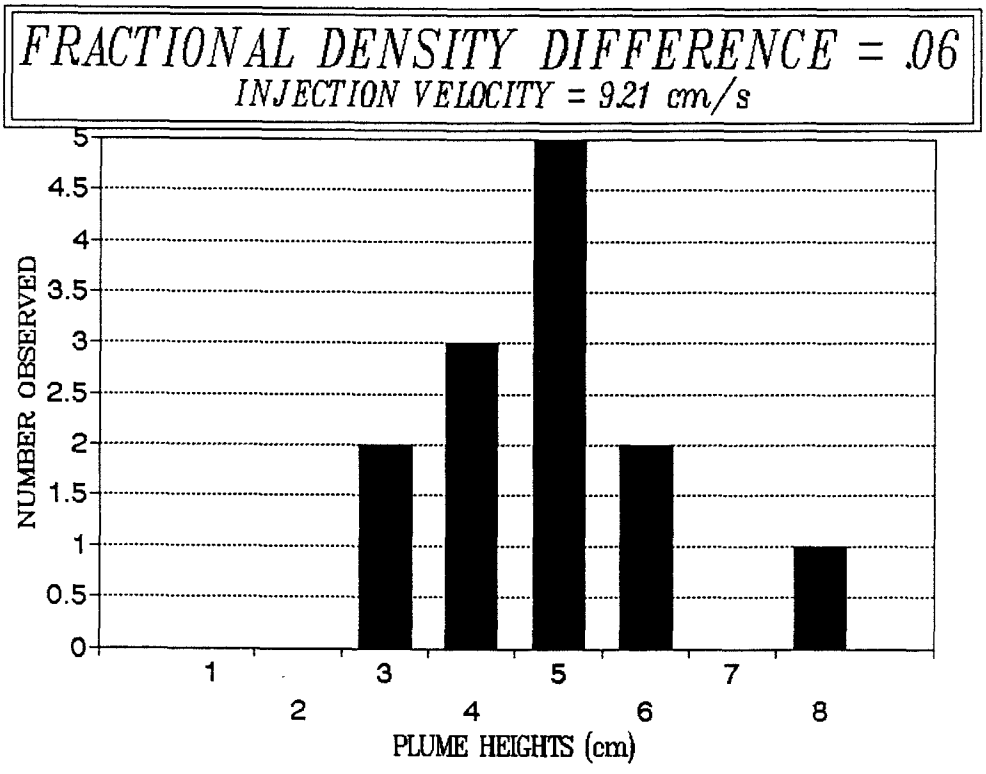
FRACTIONAL DENSITY DIFFERENCE = .06
INJECTION VELOCITY = 9.21 cm/s
NUMBER OBSERVED
0
0.5
1
1.5
2
2.5
3
3.5
4
4.5
5
1
2
3
4
5
6
7
8
PLUME HEIGHTS (cm)

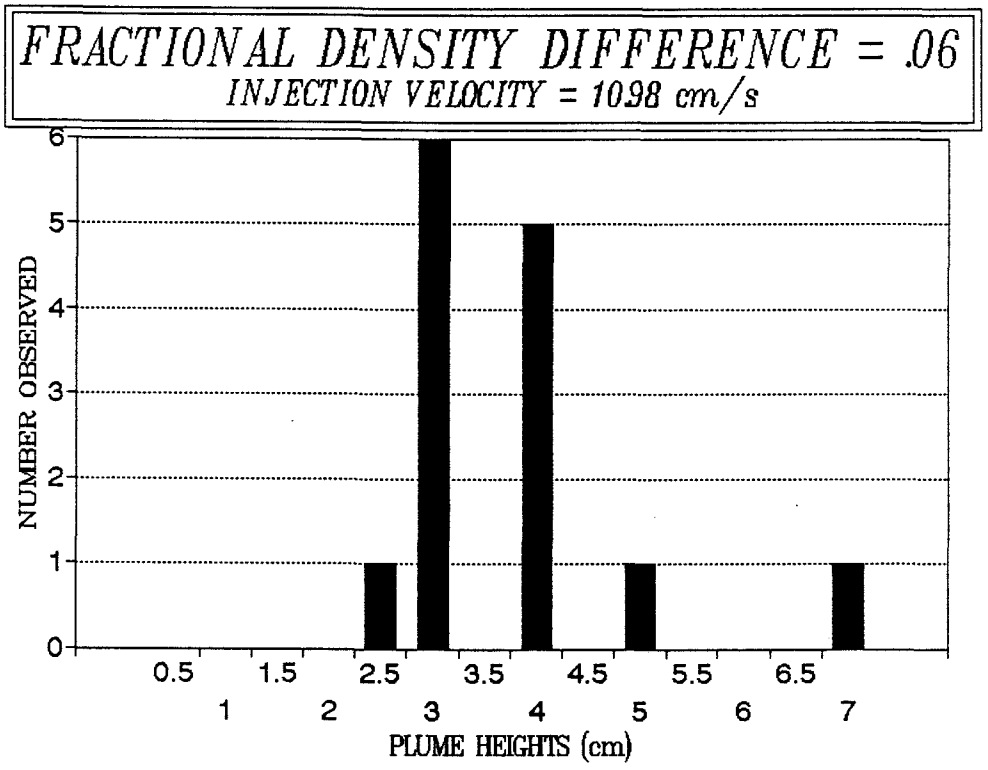
FRACTIONAL DENSITY DIFFERENCE = .06
INJECTION VELOCITY = 1098 cm/s
NUMBER OBSERVED
0
1
2
3
4
5
6
0.5
1.5
2.5
3.5
4.5
5.5
6.5
1
2
3
4
5
6
7
PLUME HEIGHTS (cm)

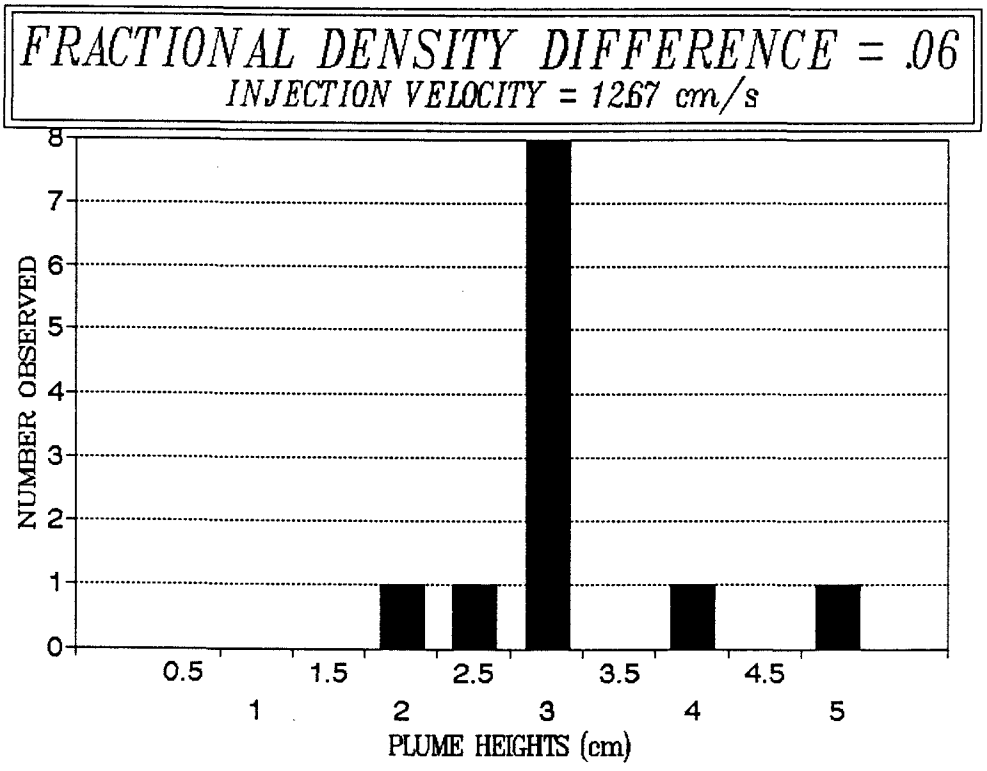
FRACTIONAL DENSITY DIFFERENCE = .06
INJECTION VELOCITY = 1267 cm/s
NUMBER OBSERVED
0
1
2
3
4
5
6
7
8
0.5
1
1.5
2
2.5
3
3.5
4
4.5
5
PLUME HEIGHTS (cm)

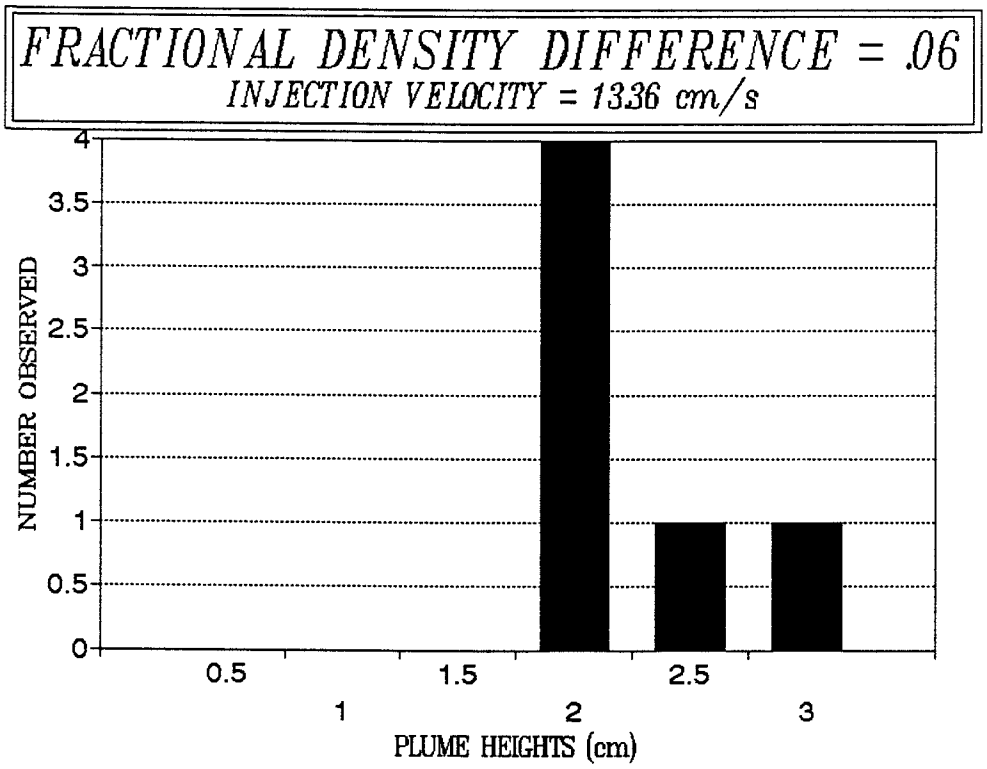
FRACTIONAL DENSITY DIFFERENCE = .06
INJECTION VELOCITY = 1336 cm/s
NUMBER OBSERVED
0
0.5
1
1.5
2
2.5
3
3.5
4
0.5
1
1.5
2
2.5
3
PLUME HEIGHTS (cm)

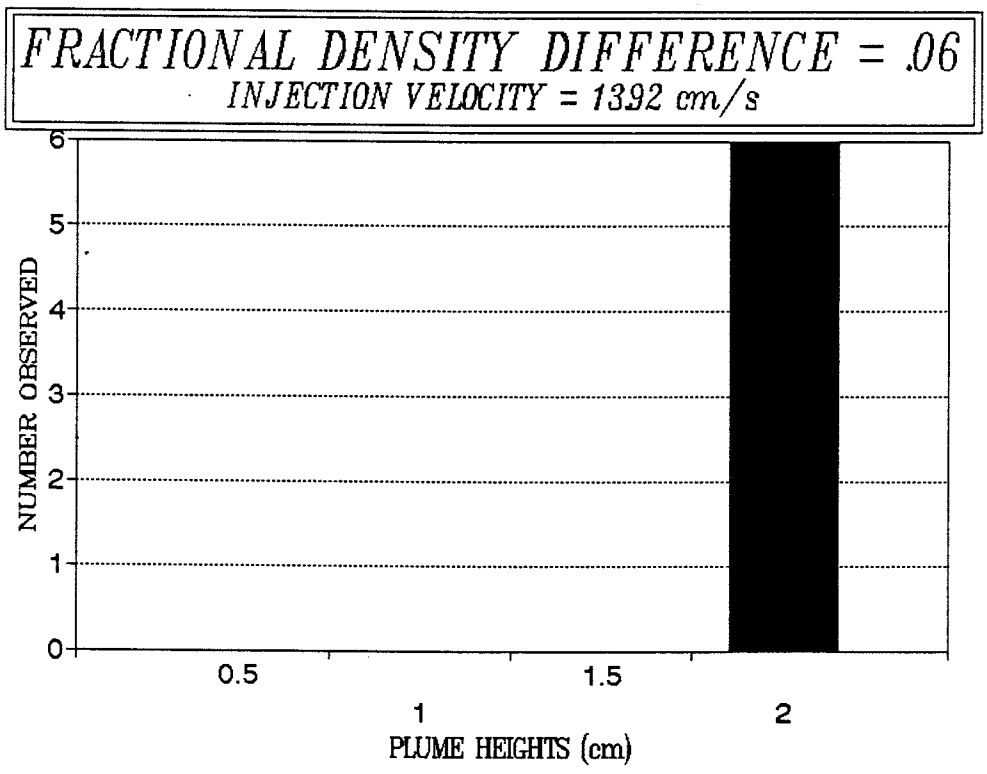
FRACTIONAL DENSITY DIFFERENCE = .06
INJECTION VELOCITY = 1392 cm/s
NUMBER OBSERVED
0
1
2
3
4
5
6
0.5
1
1.5
2
PLUME HEIGHTS (cm)

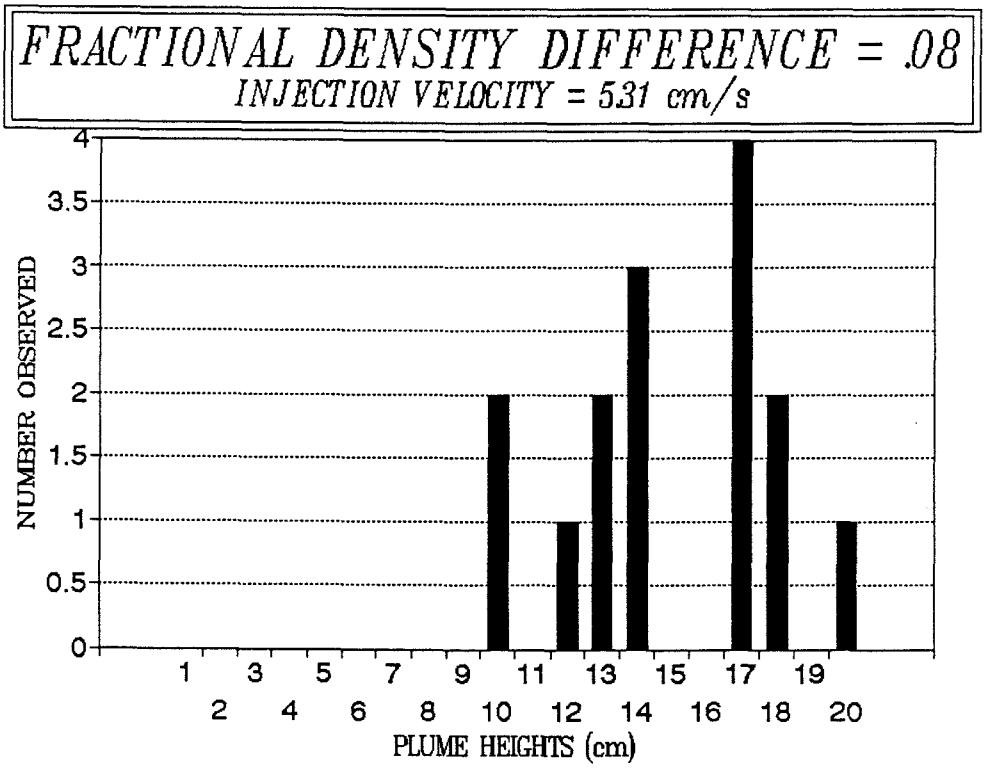
FRACTIONAL DENSITY DIFFERENCE = .08
INJECTION VELOCITY = 5.31 cm/s
NUMBER OBSERVED
0
0.5
1
1.5
2
2.5
3
3.5
4
1 2 3 4 5 6 7 8 9 10 11 12 13 14 15 16 17 18 19 20
PLUME HEIGHTS (cm)

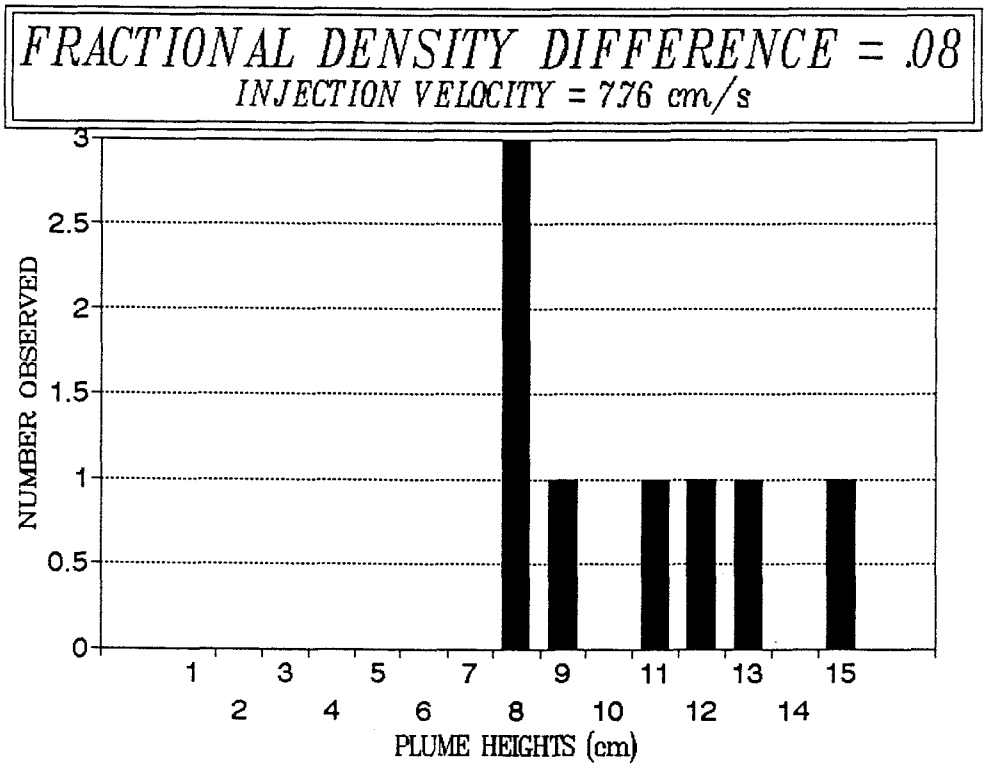
FRACTIONAL DENSITY DIFFERENCE = .08
INJECTION VELOCITY = 7.76 cm/s
NUMBER OBSERVED
0
0.5
1
1.5
2
2.5
3
1
2
3
4
5
6
7
8
9
10
11
12
13
14
15
PLUME HEIGHTS (cm)

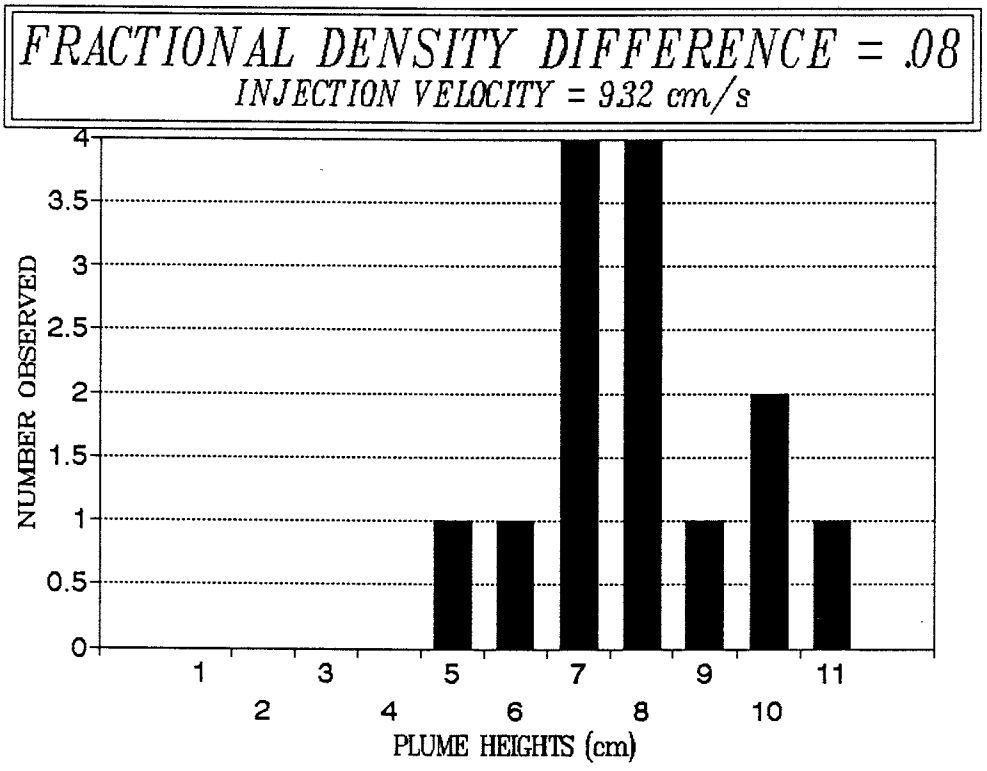
FRACTIONAL DENSITY DIFFERENCE = .08
INJECTION VELOCITY = 9.32 cm/s
NUMBER OBSERVED
0
0.5
1
1.5
2
2.5
3
3.5
4
1
2
3
4
5
6
7
8
9
10
11
PLUME HEIGHTS (cm)

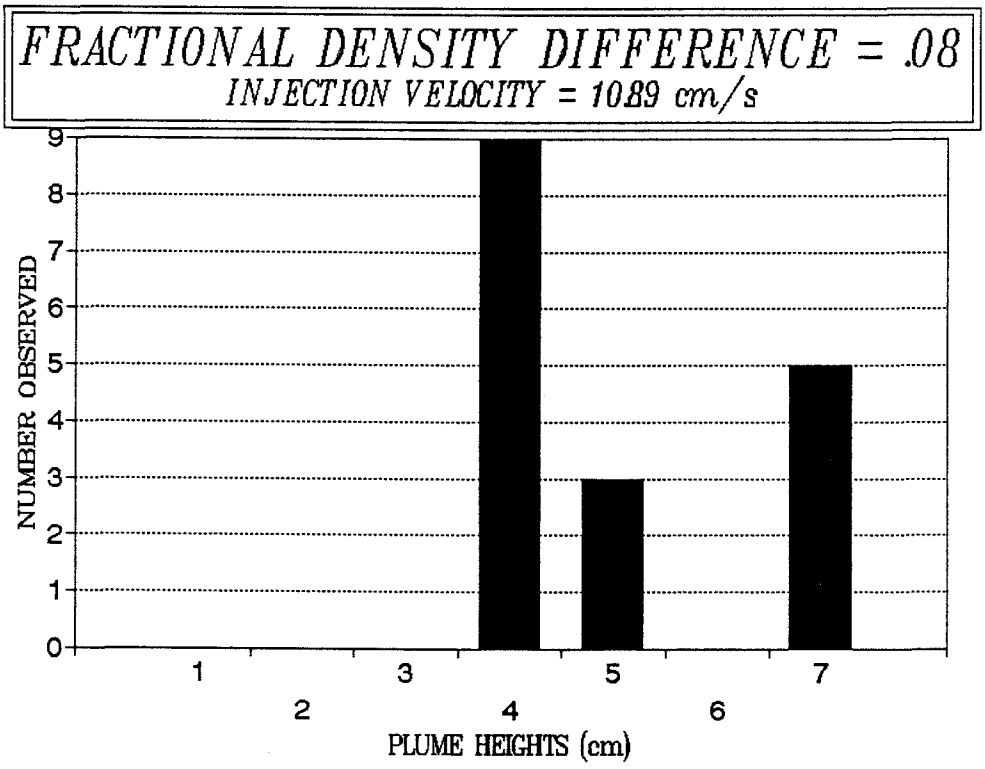
FRACTIONAL DENSITY DIFFERENCE = .08
INJECTION VELOCITY = 1089 cm/s
NUMBER OBSERVED
0
1
2
3
4
5
6
7
8
9
1
2
3
4
5
6
7
PLUME HEIGHTS (cm)

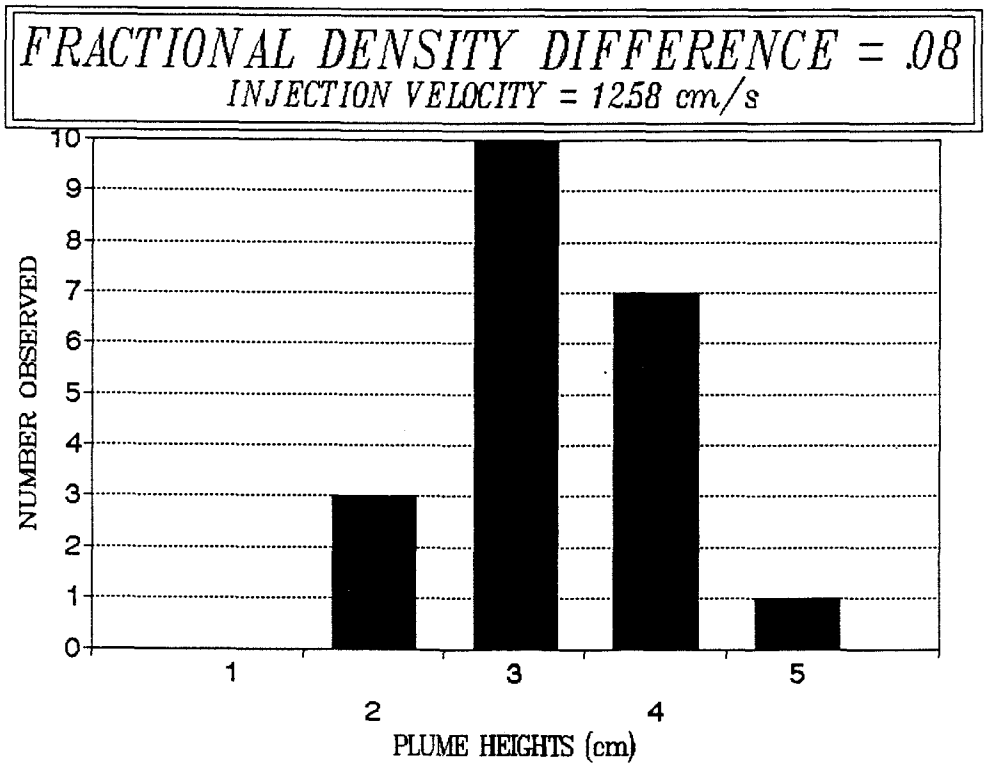
FRACTIONAL DENSITY DIFFERENCE = .08
INJECTION VELOCITY = 1258 cm/s
NUMBER OBSERVED
0
1
2
3
4
5
6
7
8
9
10
1
2
3
4
5
PLUME HEIGHTS (cm)

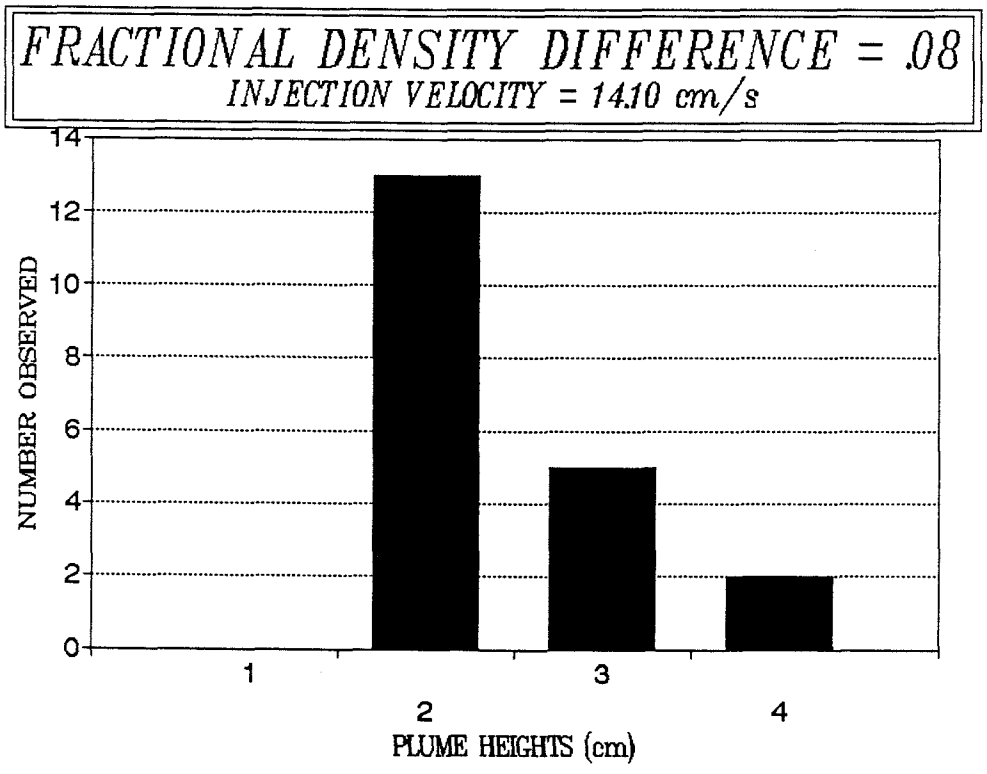
FRACTIONAL DENSITY DIFFERENCE = .08
INJECTION VELOCITY = 14.10 cm/s
NUMBER OBSERVED
0
2
4
6
8
10
12
14
1
2
3
4
PLUME HEIGHTS (cm)

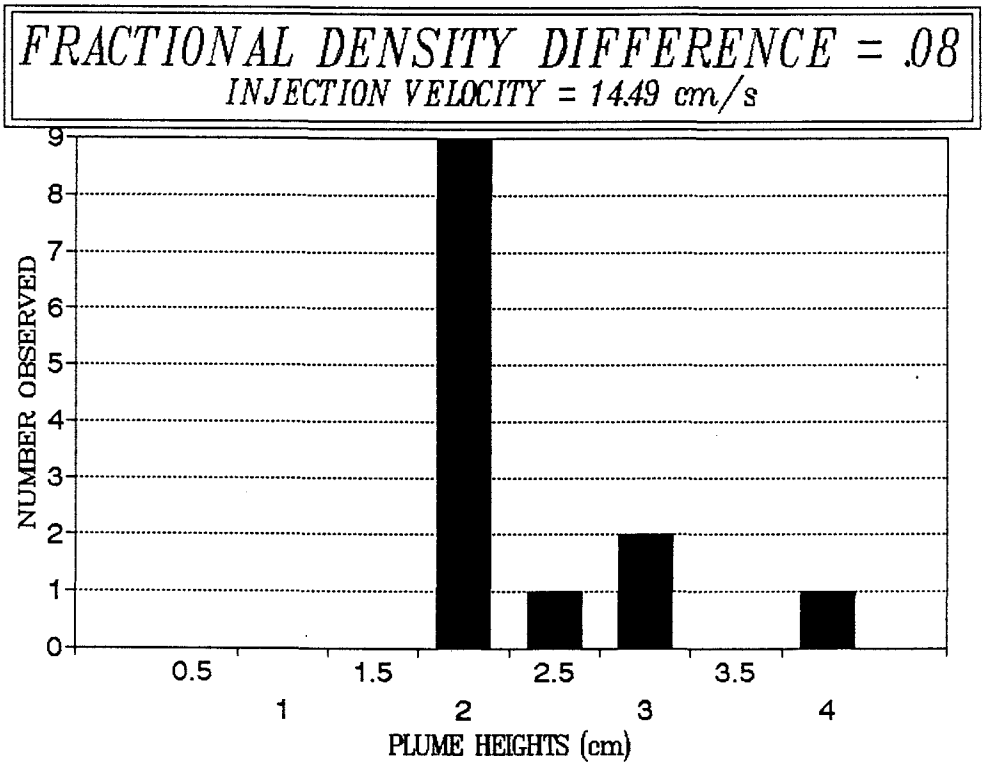
FRACTIONAL DENSITY DIFFERENCE = .08
INJECTION VELOCITY = 14.49 cm/s
NUMBER OBSERVED
0
1
2
3
4
5
6
7
8
9
0.5
1
1.5
2
2.5
3
3.5
4
PLUME HEIGHTS (cm)

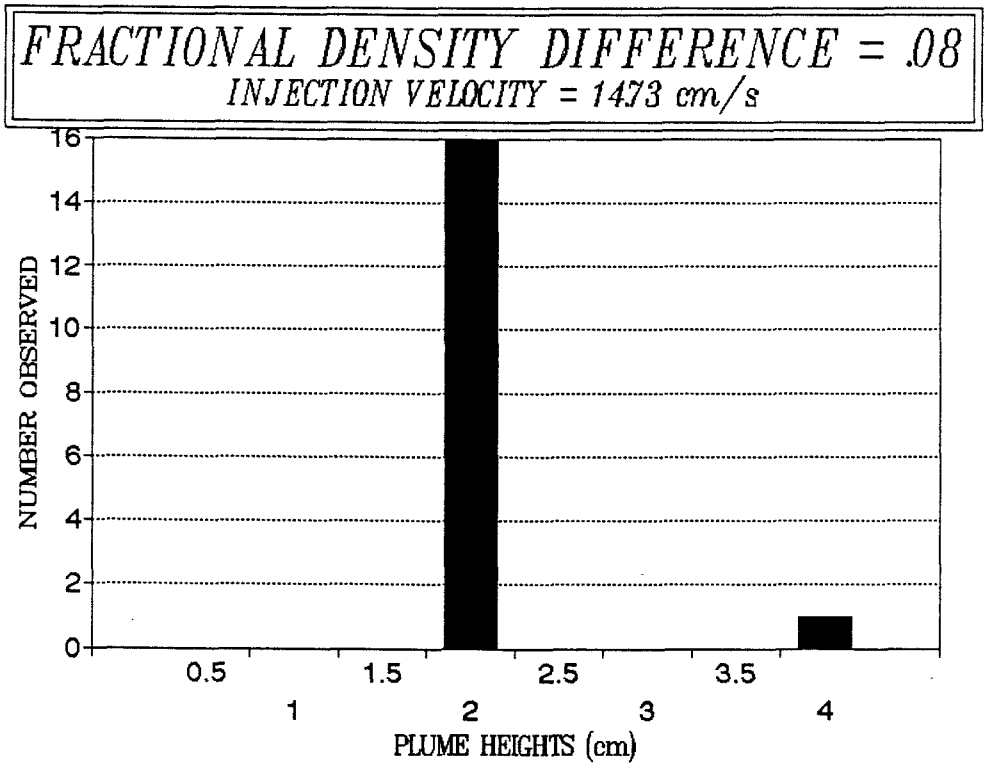
FRACTIONAL DENSITY DIFFERENCE = .08
INJECTION VELOCITY = 1473 cm/s
NUMBER OBSERVED
16
14
12
10
8
6
4
2
0
0.5
1
1.5
2
2.5
3
3.5
4
PLUME HEIGHTS (cm)

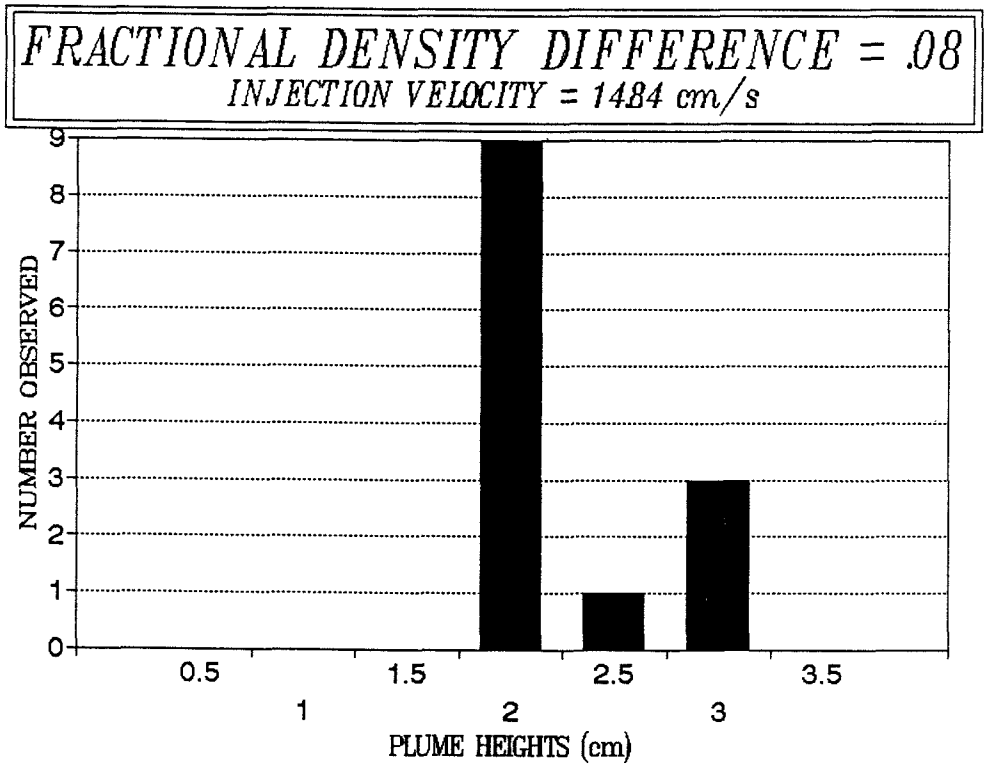
FRACTIONAL DENSITY DIFFERENCE = .08
INJECTION VELOCITY = 1484 cm/s
NUMBER OBSERVED
0
1
2
3
4
5
6
7
8
9
0.5
1
1.5
2
2.5
3
3.5
PLUME HEIGHTS (cm)

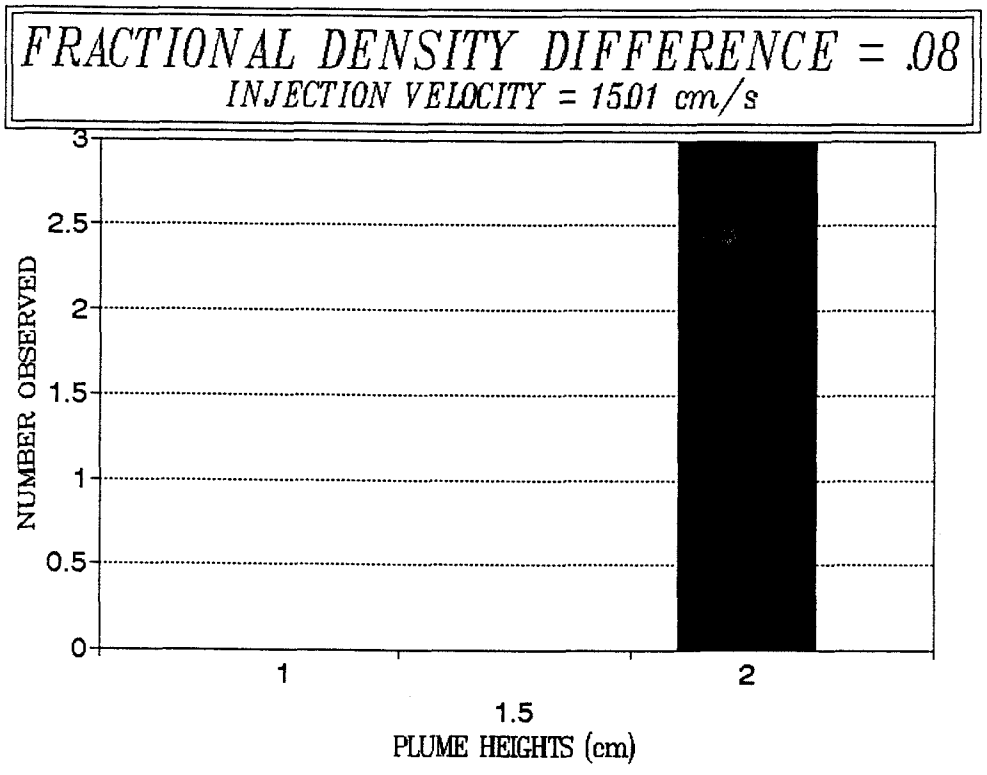
FRACTIONAL DENSITY DIFFERENCE = .08
INJECTION VELOCITY = 1501 cm/s
NUMBER OBSERVED
3
2.5
2
1.5
1
0.5
0
1
2
1.5
PLUME HEIGHTS (cm)

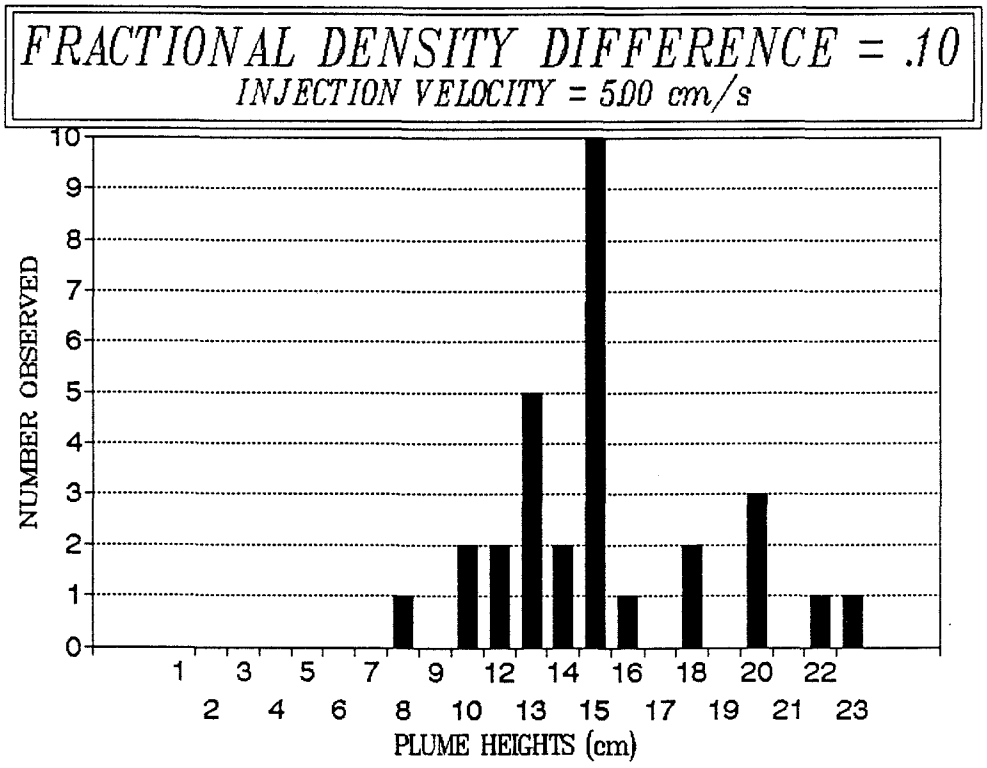
FRACTIONAL DENSITY DIFFERENCE = .10
INJECTION VELOCITY = 500 cm/s
NUMBER OBSERVED
0
1
2
3
4
5
6
7
8
9
10
1 2 3 4 5 6 7 8 9 10 12 13 14 15 16 17 18 19 20 21 22 23
PLUME HEIGHTS (cm)

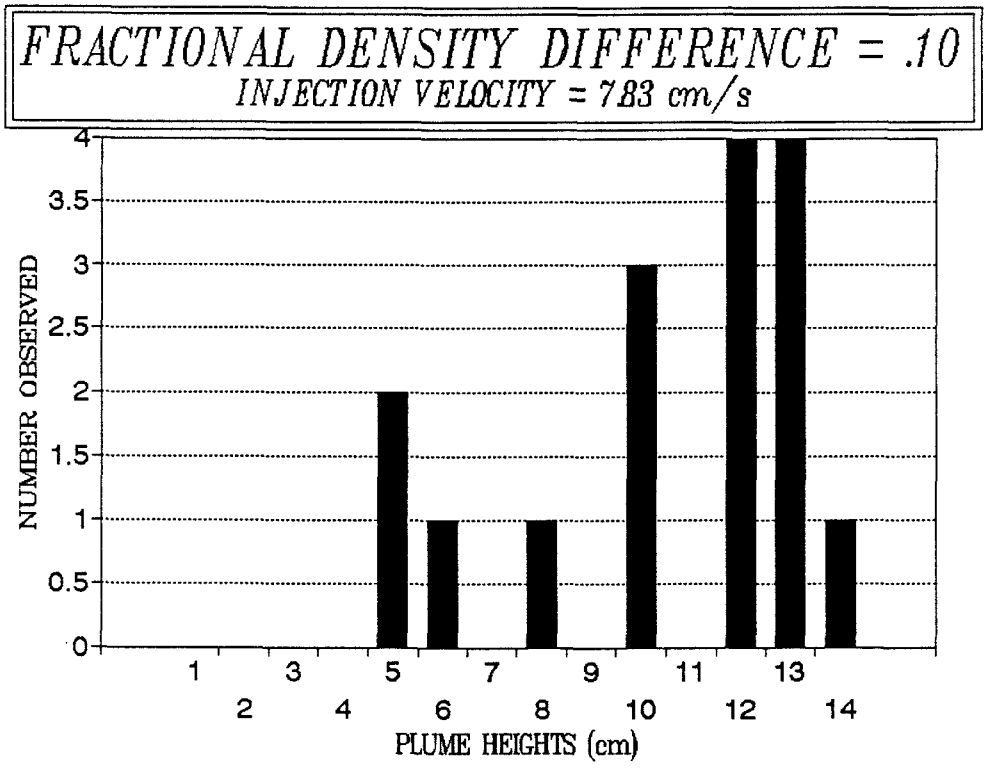
FRACTIONAL DENSITY DIFFERENCE = .10
INJECTION VELOCITY = 7.83 cm/s
NUMBER OBSERVED
0
0.5
1
1.5
2
2.5
3
3.5
4
1
2
3
4
5
6
7
8
9
10
11
12
13
14
PLUME HEIGHTS (cm)

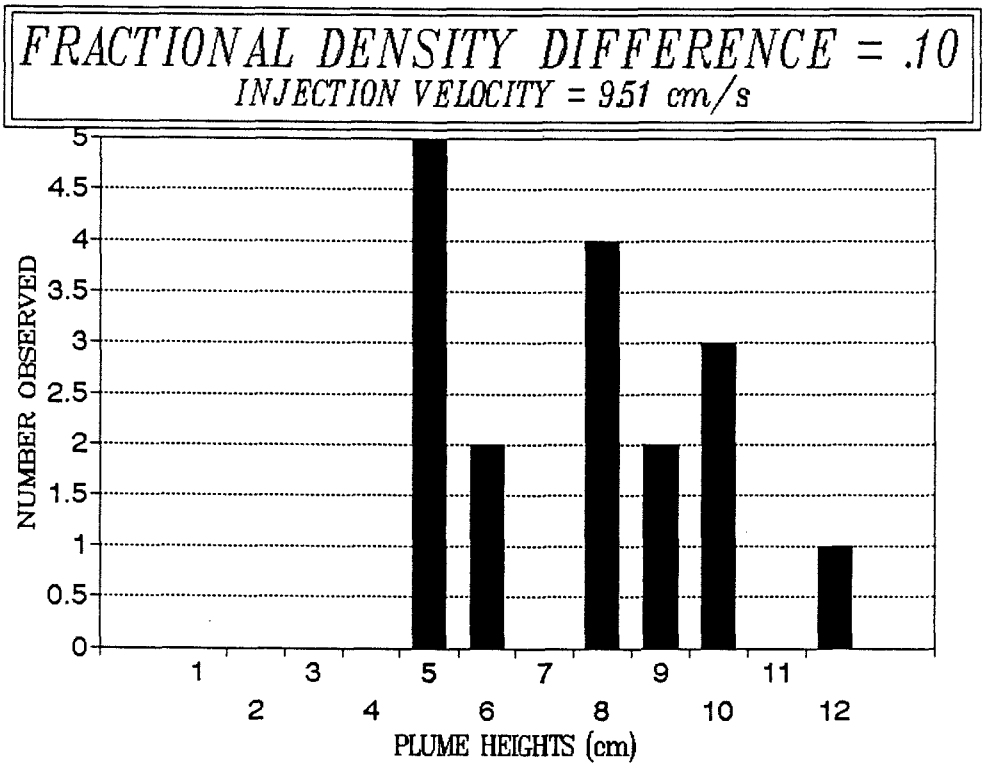
FRACTIONAL DENSITY DIFFERENCE = .10
INJECTION VELOCITY = 9.51 cm/s
NUMBER OBSERVED
0
0.5
1
1.5
2
2.5
3
3.5
4
4.5
5
1
2
3
4
5
6
7
8
9
10
11
12
PLUME HEIGHTS (cm)

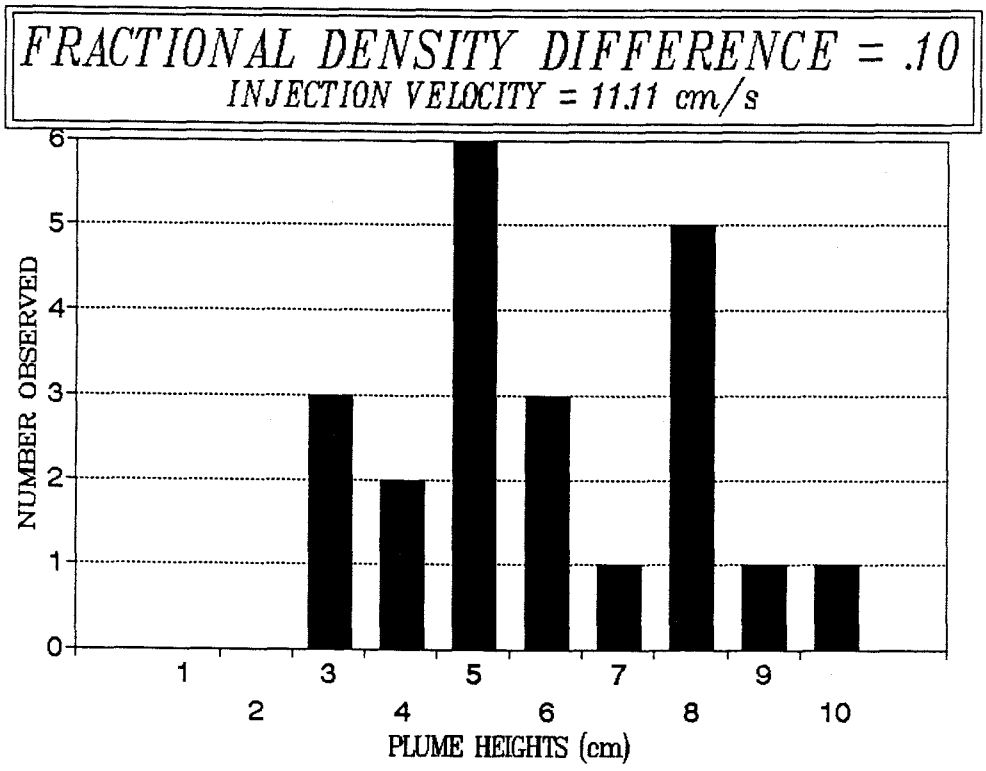
FRACTIONAL DENSITY DIFFERENCE = .10
INJECTION VELOCITY = 11.11 cm/s
NUMBER OBSERVED
0
1
2
3
4
5
6
1
2
3
4
5
6
7
8
9
10
PLUME HEIGHTS (cm)

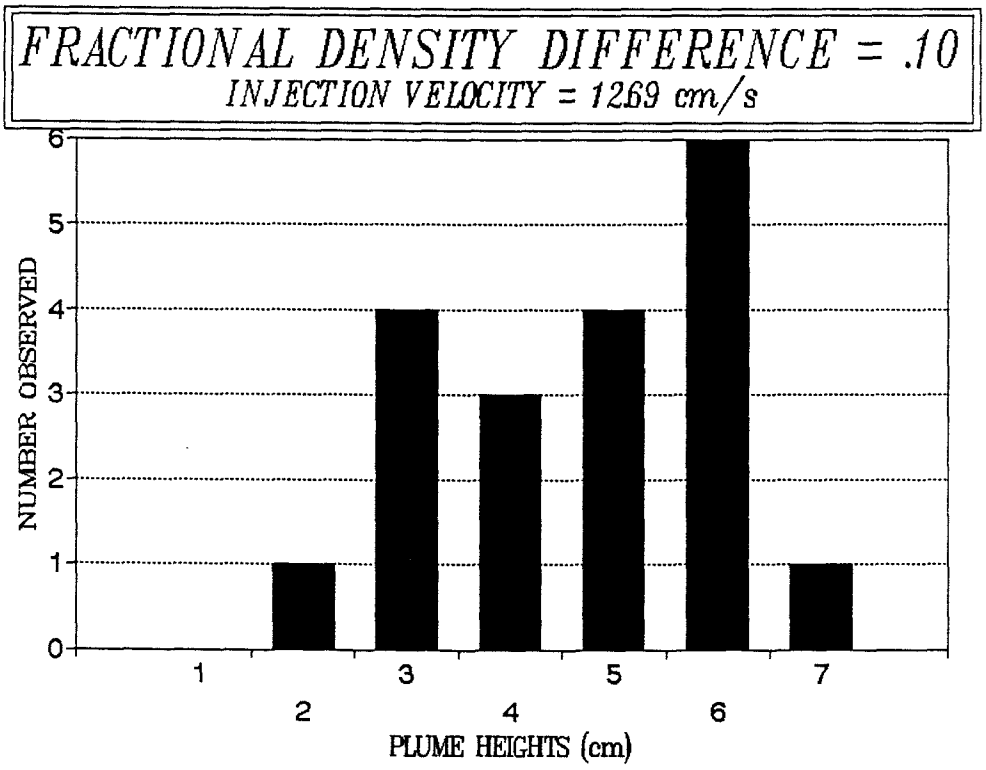
FRACTIONAL DENSITY DIFFERENCE = .10
INJECTION VELOCITY = 1269 cm/s
NUMBER OBSERVED
0
1
2
3
4
5
6
1
2
3
4
5
6
7
PLUME HEIGHTS (cm)

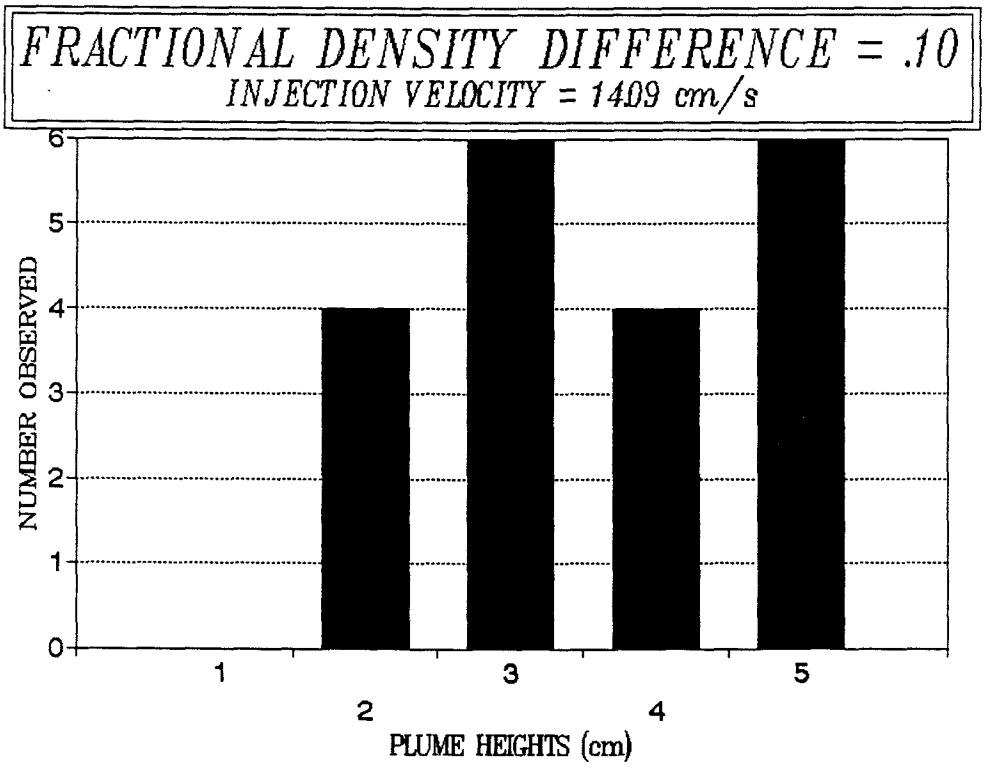
FRACTIONAL DENSITY DIFFERENCE = .10
INJECTION VELOCITY = 1409 cm/s
NUMBER OBSERVED
0
1
2
3
4
5
6
1
2
3
4
5
PLUME HEIGHTS (cm)

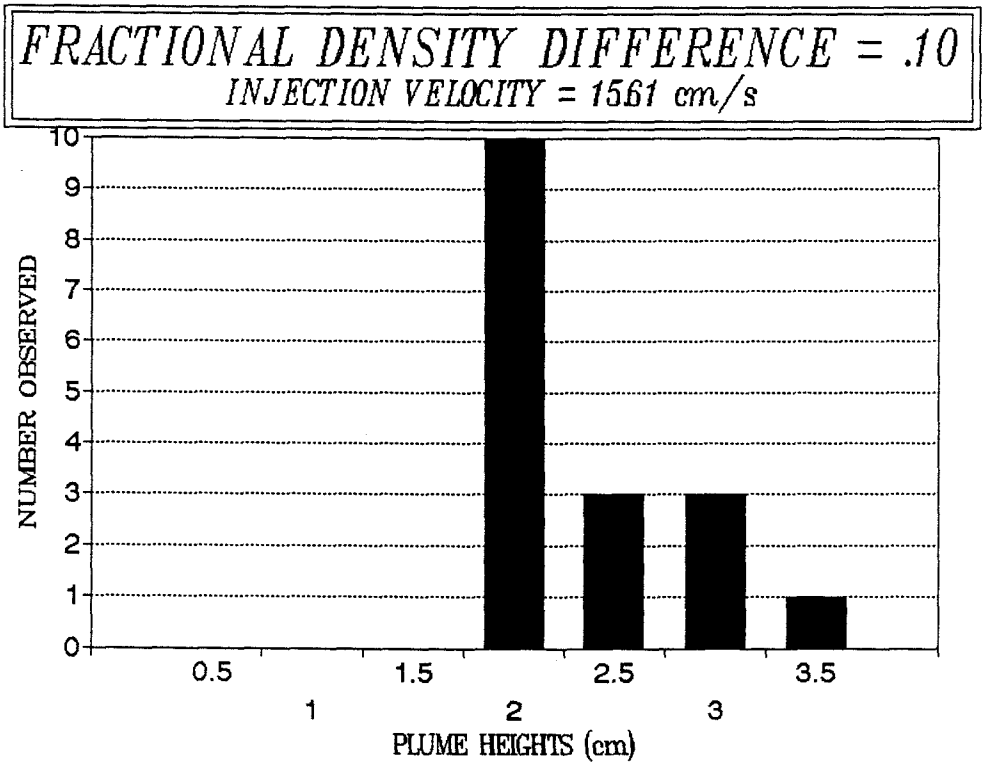
FRACTIONAL DENSITY DIFFERENCE = .10
INJECTION VELOCITY = 1561 cm/s
NUMBER OBSERVED
0
1
2
3
4
5
6
7
8
9
10
0.5
1
1.5
2
2.5
3
3.5
PLUME HEIGHTS (cm)

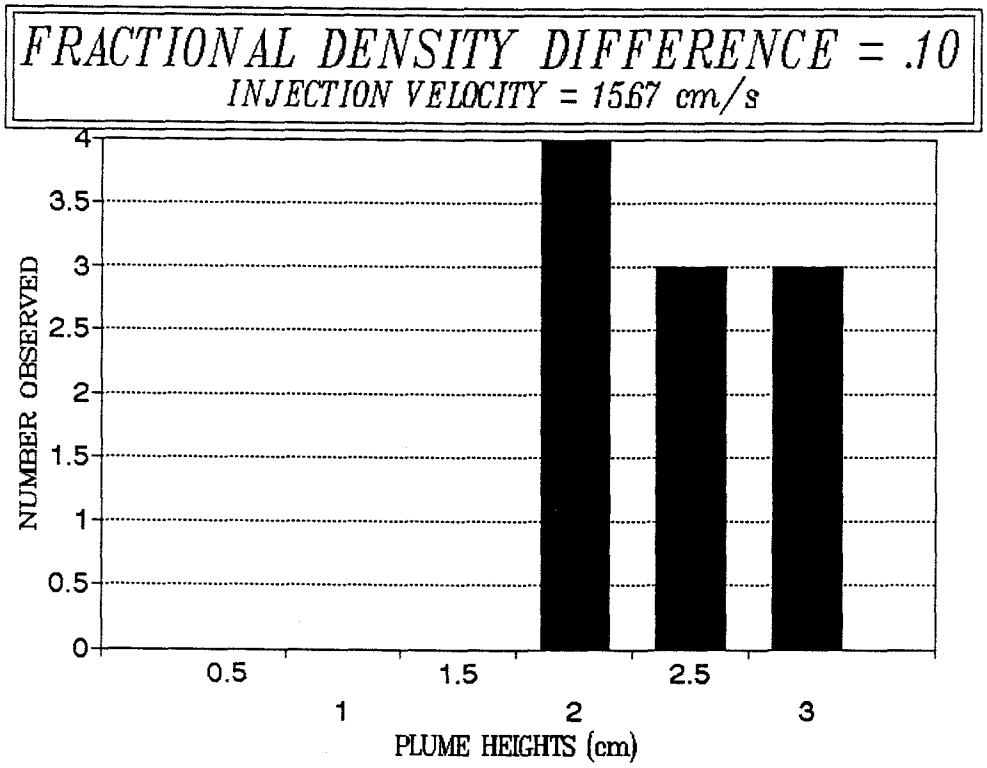
FRACTIONAL DENSITY DIFFERENCE = .10
INJECTION VELOCITY = 1567 cm/s
NUMBER OBSERVED
0
0.5
1
1.5
2
2.5
3
3.5
4
0.5
1
1.5
2
2.5
3
PLUME HEIGHTS (cm)

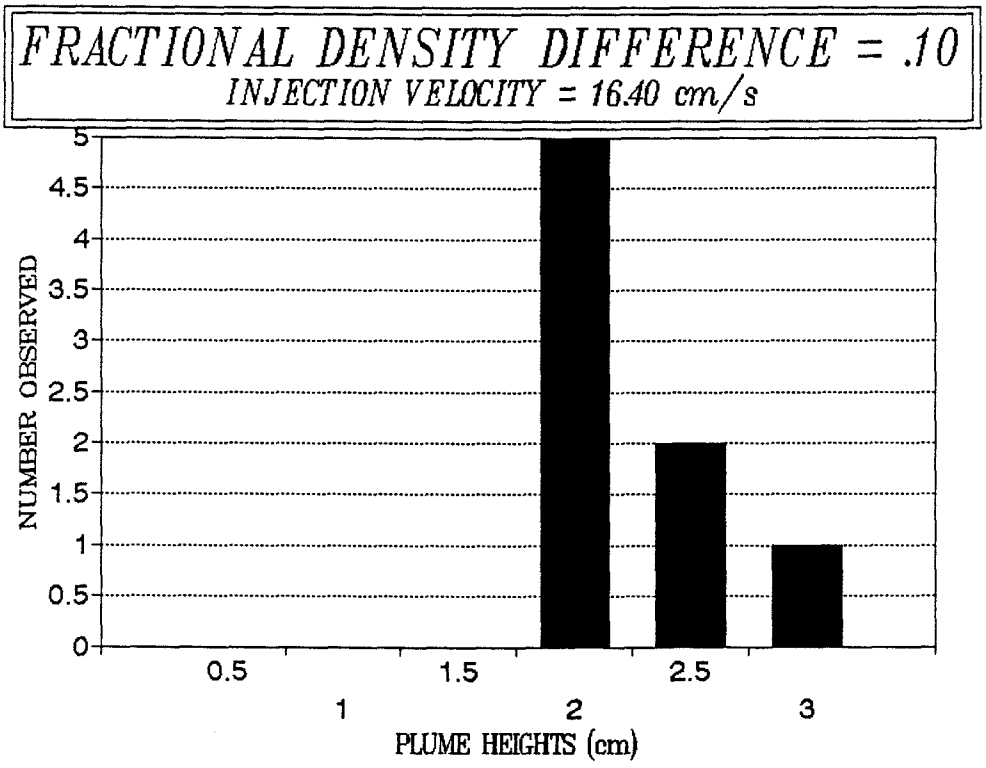
FRACTIONAL DENSITY DIFFERENCE = .10
INJECTION VELOCITY = 16.40 cm/s
NUMBER OBSERVED
0
0.5
1
1.5
2
2.5
3
3.5
4
4.5
5
0.5
1
1.5
2
2.5
3
PLUME HEIGHTS (cm)

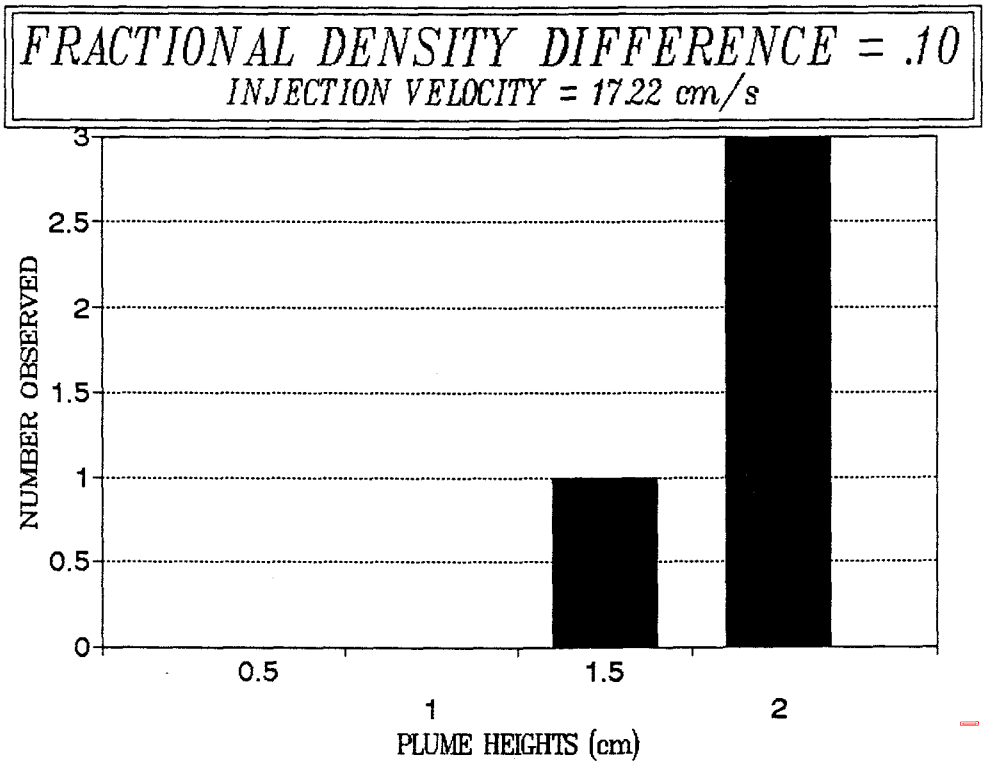
FRACTIONAL DENSITY DIFFERENCE = .10
INJECTION VELOCITY = 17.22 cm/s
NUMBER OBSERVED
3
2.5
2
1.5
1
0.5
0
0.5
1
1.5
2
PLUME HEIGHTS (cm)

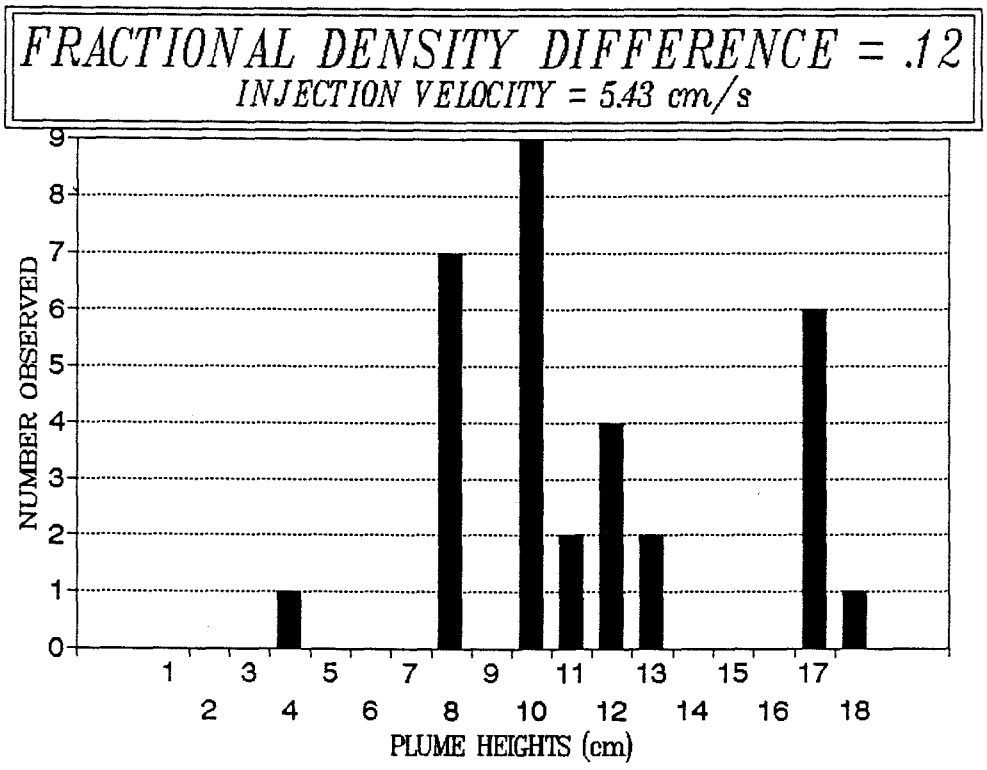
FRACTIONAL DENSITY DIFFERENCE = .12
INJECTION VELOCITY = 5.43 cm/s
NUMBER OBSERVED
0
1
2
3
4
5
6
7
8
9
1
2
3
4
5
6
7
8
9
10
11
12
13
14
15
16
17
18
PLUME HEIGHTS (cm)

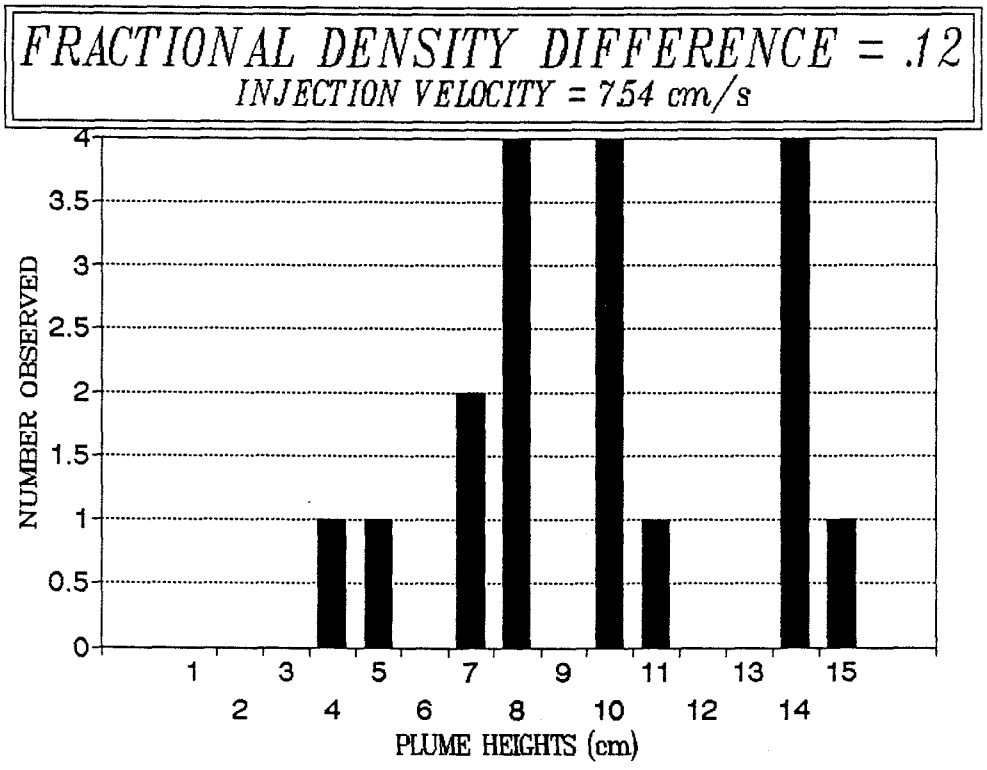
FRACTIONAL DENSITY DIFFERENCE = .12
INJECTION VELOCITY = 7.54 cm/s
NUMBER OBSERVED
0
0.5
1
1.5
2
2.5
3
3.5
4
1
2
3
4
5
6
7
8
9
10
11
12
13
14
15
PLUME HEIGHTS (cm)

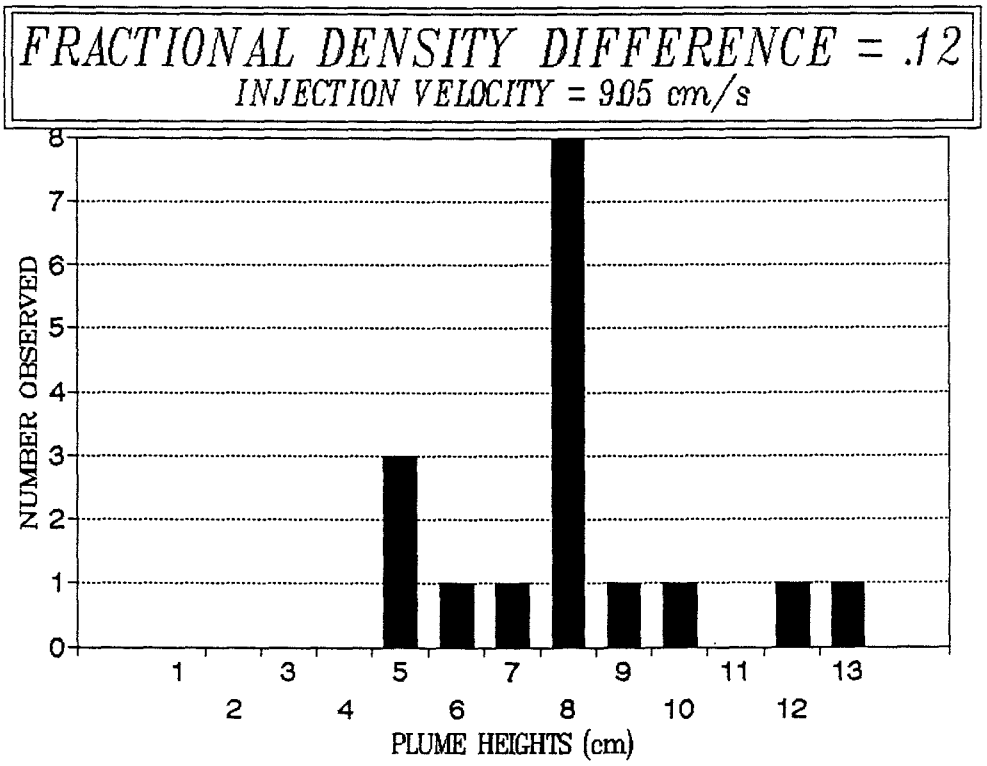
FRACTIONAL DENSITY DIFFERENCE = .12
INJECTION VELOCITY = 9.05 cm/s
NUMBER OBSERVED
0
1
2
3
4
5
6
7
8
1
2
3
4
5
6
7
8
9
10
11
12
13
PLUME HEIGHTS (cm)

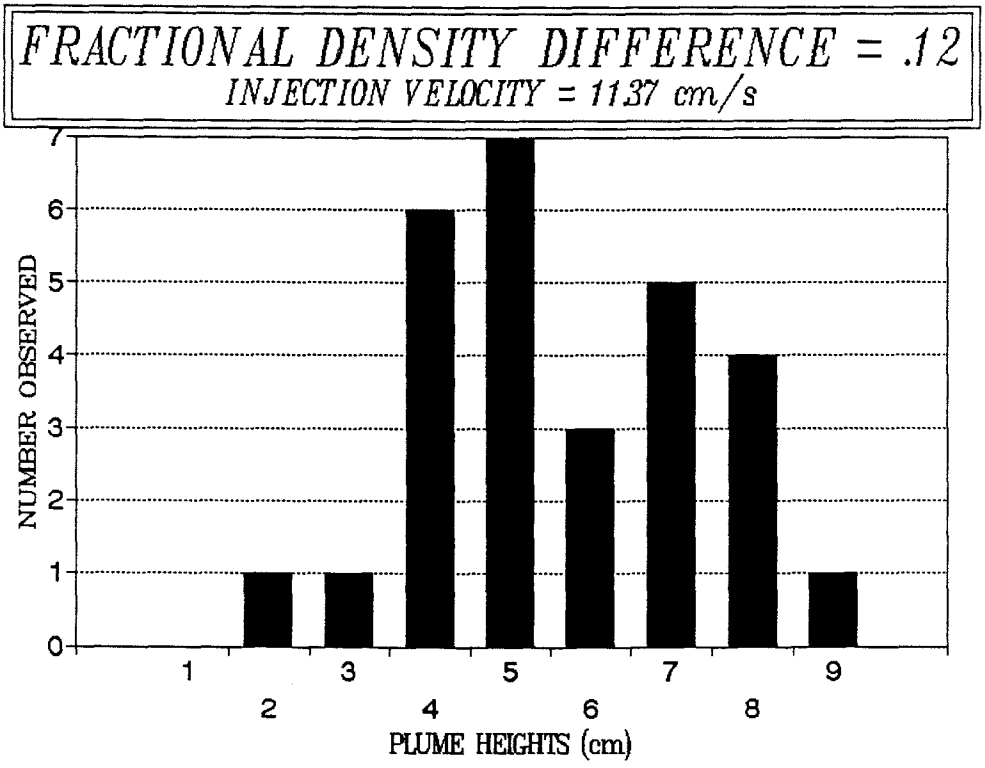
FRACTIONAL DENSITY DIFFERENCE = .12
INJECTION VELOCITY = 1137 cm/s
NUMBER OBSERVED
0
1
2
3
4
5
6
7
1
2
3
4
5
6
7
8
9
PLUME HEIGHTS (cm)

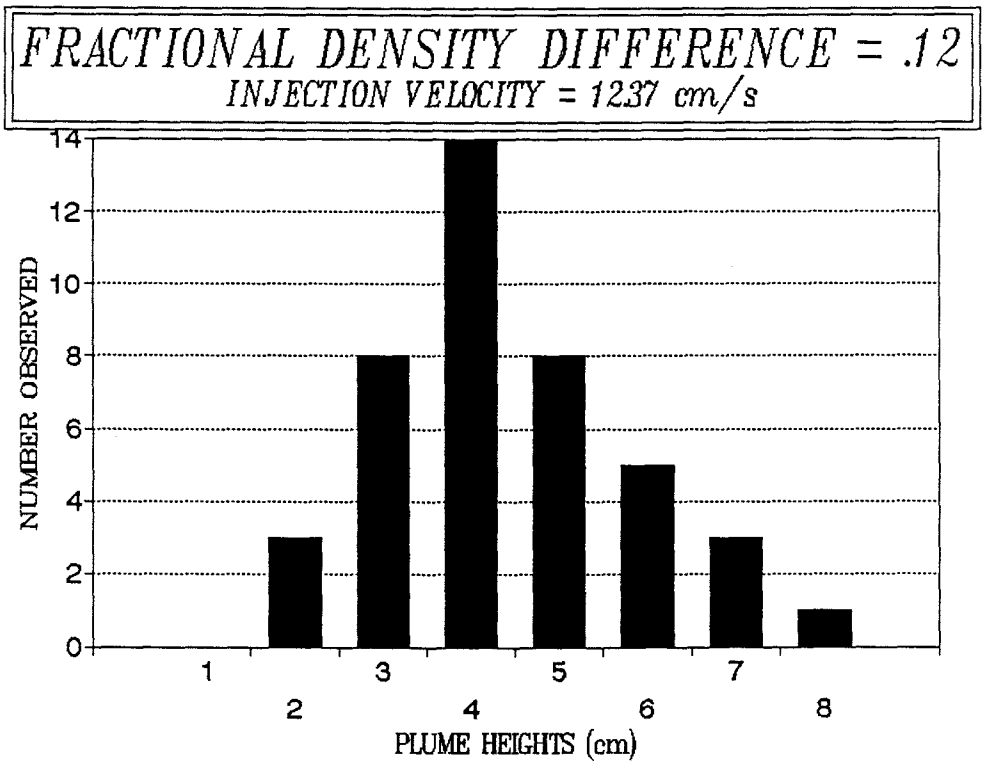
FRACTIONAL DENSITY DIFFERENCE = .12
INJECTION VELOCITY = 1237 cm/s
NUMBER OBSERVED
0
2
4
6
8
10
12
14
1
2
3
4
5
6
7
8
PLUME HEIGHTS (cm)

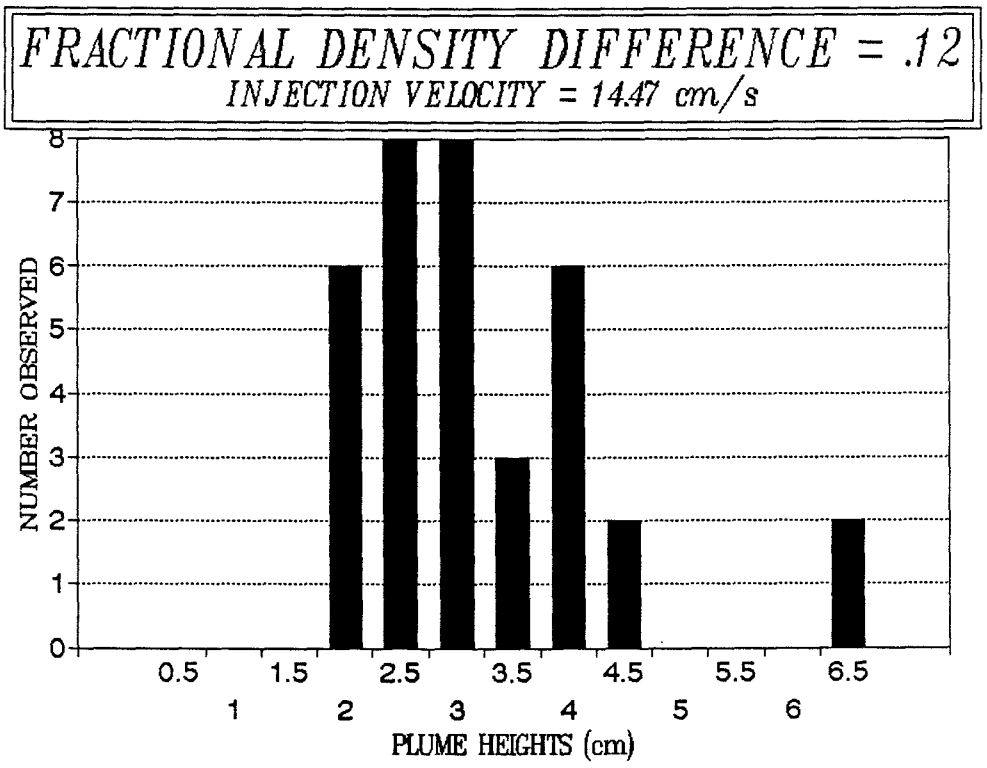
FRACTIONAL DENSITY DIFFERENCE = .12
INJECTION VELOCITY = 14.47 cm/s
NUMBER OBSERVED
0
1
2
3
4
5
6
7
8
0.5
1.5
2.5
3.5
4.5
5.5
6.5
1
2
3
4
5
6
PLUME HEIGHTS (cm)

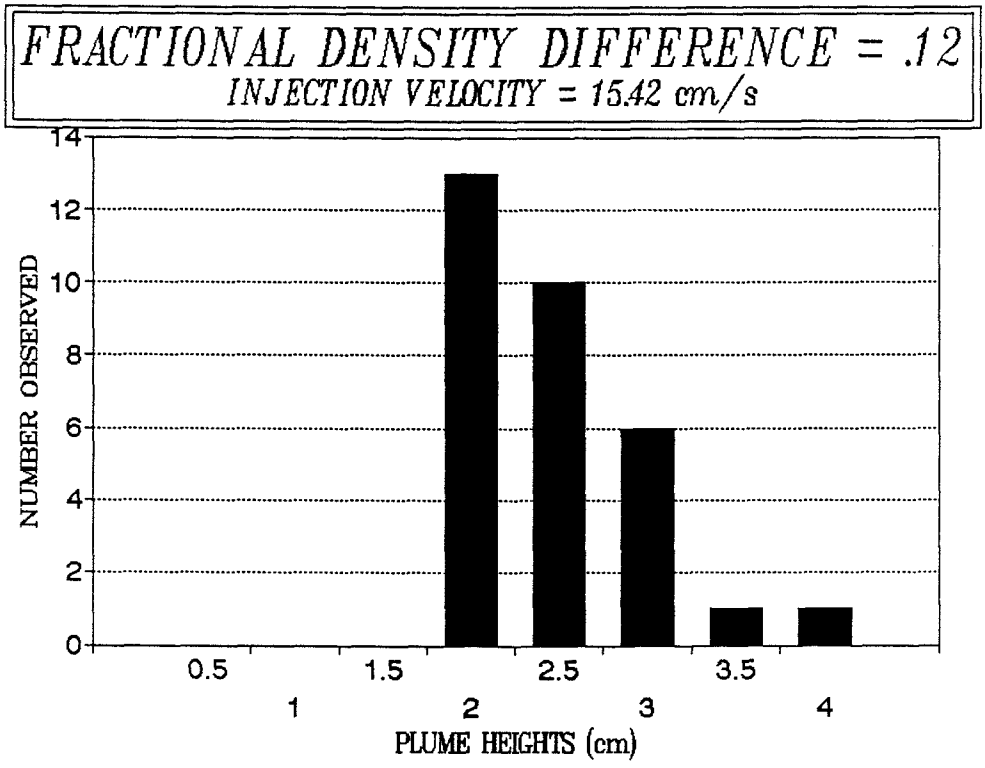
FRACTIONAL DENSITY DIFFERENCE = .12
INJECTION VELOCITY = 15.42 cm/s
NUMBER OBSERVED
0
2
4
6
8
10
12
14
0.5
1
1.5
2
2.5
3
3.5
4
PLUME HEIGHTS (cm)

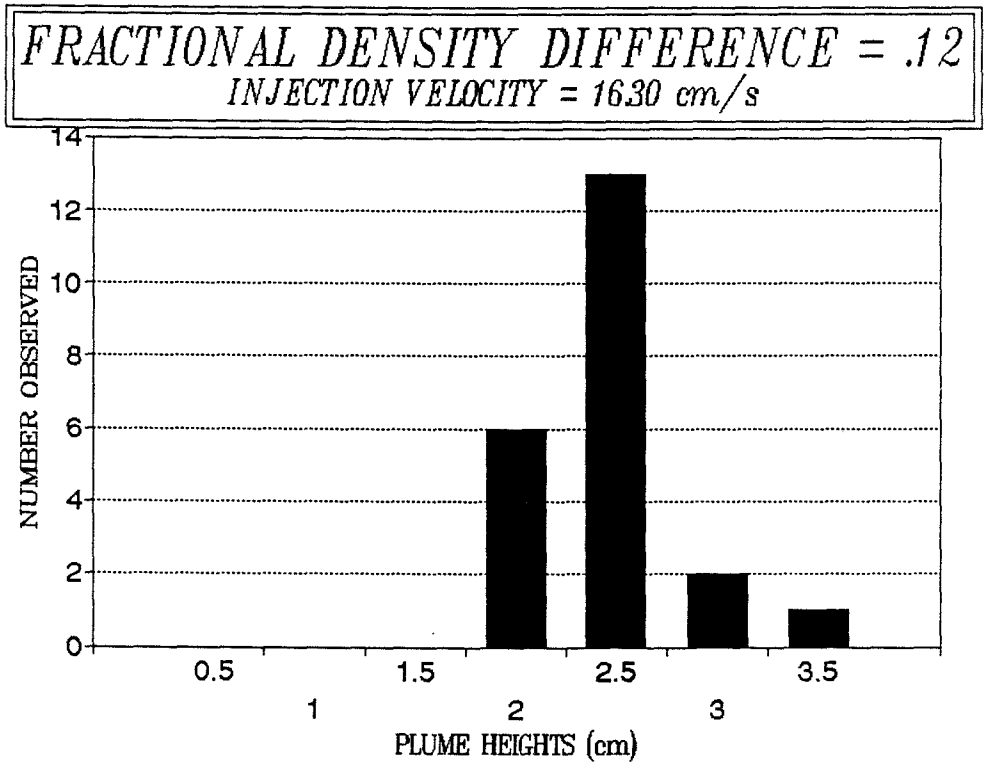
FRACTIONAL DENSITY DIFFERENCE = .12
INJECTION VELOCITY = 1630 cm/s
NUMBER OBSERVED
14
12
10
8
6
4
2
0
0.5
1.5
2.5
3.5
1
2
3
PLUME HEIGHTS (cm)

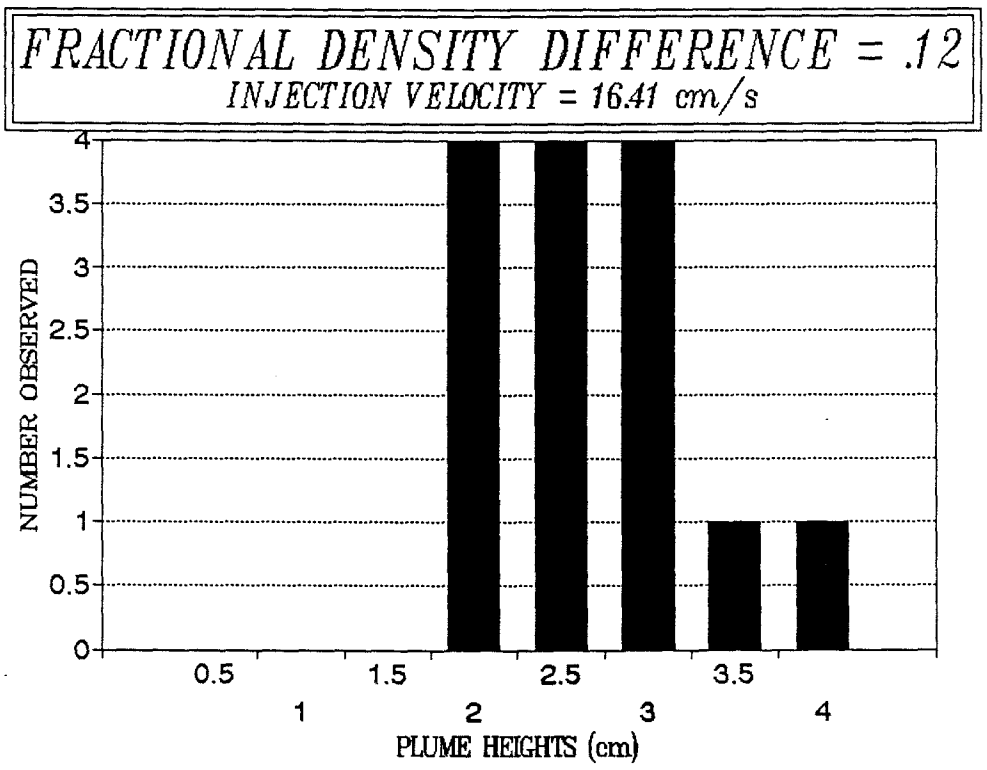
FRACTIONAL DENSITY DIFFERENCE = .12
INJECTION VELOCITY = 16.41 cm/s
NUMBER OBSERVED
0
0.5
1
1.5
2
2.5
3
3.5
4
0.5
1
1.5
2
2.5
3
3.5
4
PLUME HEIGHTS (cm)

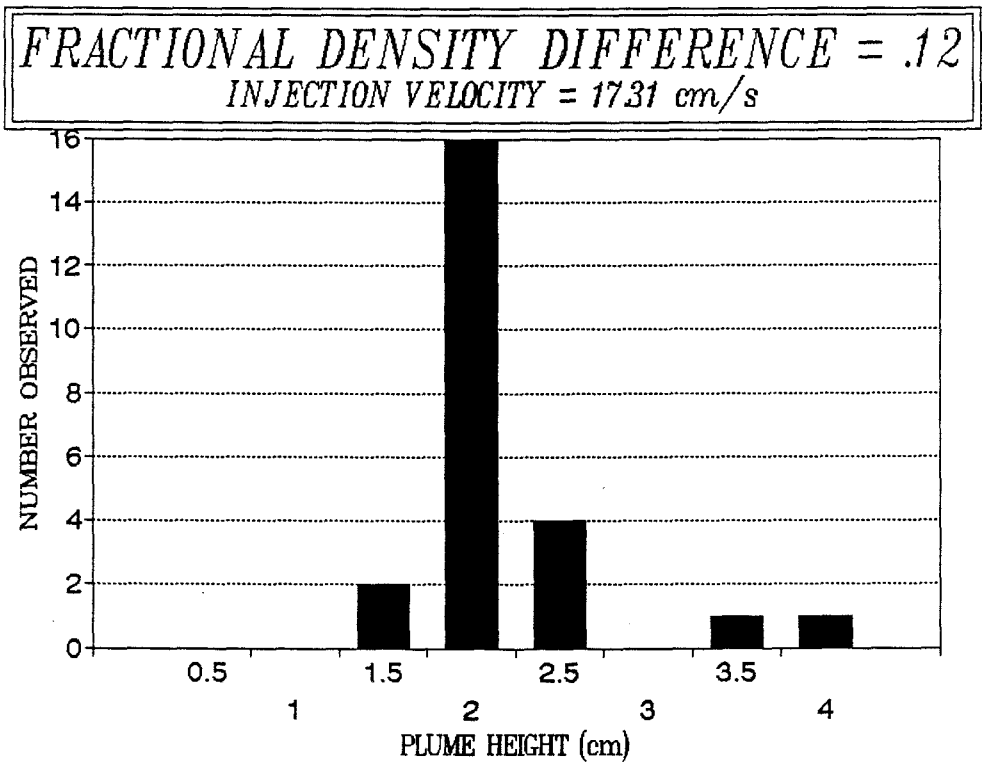
FRACTIONAL DENSITY DIFFERENCE = .12
INJECTION VELOCITY = 1731 cm/s
NUMBER OBSERVED
16
14
12
10
8
6
4
2
0
0.5
1.5
2.5
3.5
1
2
3
4
PLUME HEIGHT (cm)

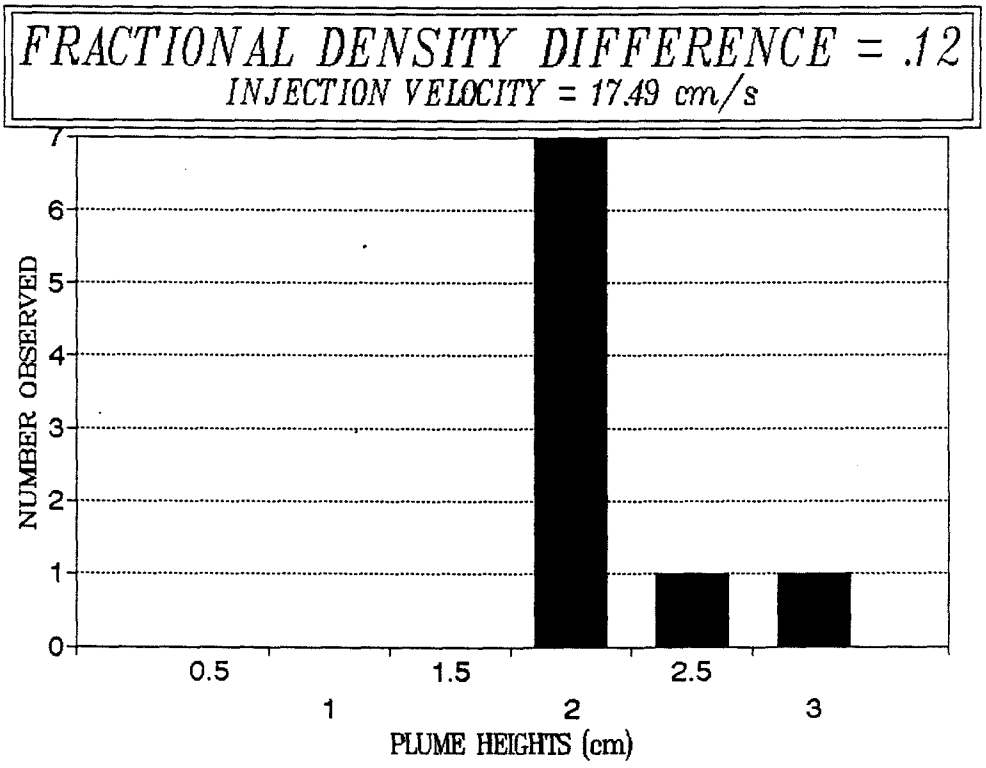
FRACTIONAL DENSITY DIFFERENCE = .12
INJECTION VELOCITY = 17.49 cm/s
NUMBER OBSERVED
0
1
2
3
4
5
6
7
0.5
1
1.5
2
2.5
3
PLUME HEIGHTS (cm)

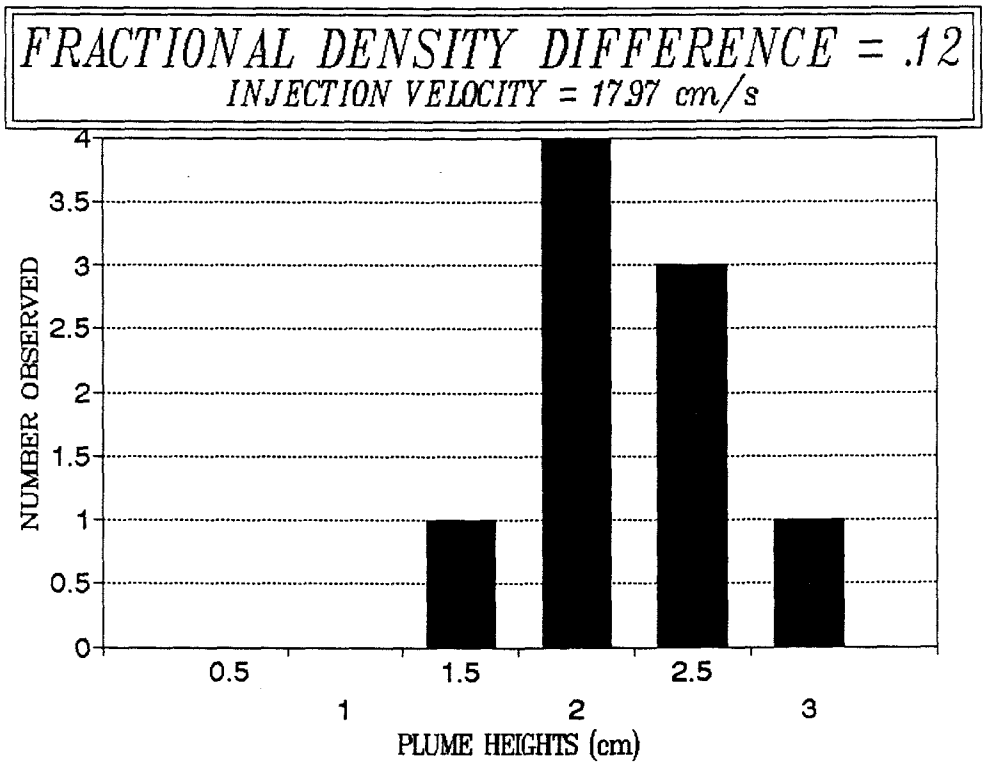
FRACTIONAL DENSITY DIFFERENCE = .12
INJECTION VELOCITY = 17.97 cm/s
NUMBER OBSERVED
0
0.5
1
1.5
2
2.5
3
3.5
4
0.5
1
1.5
2
2.5
3
PLUME HEIGHTS (cm)

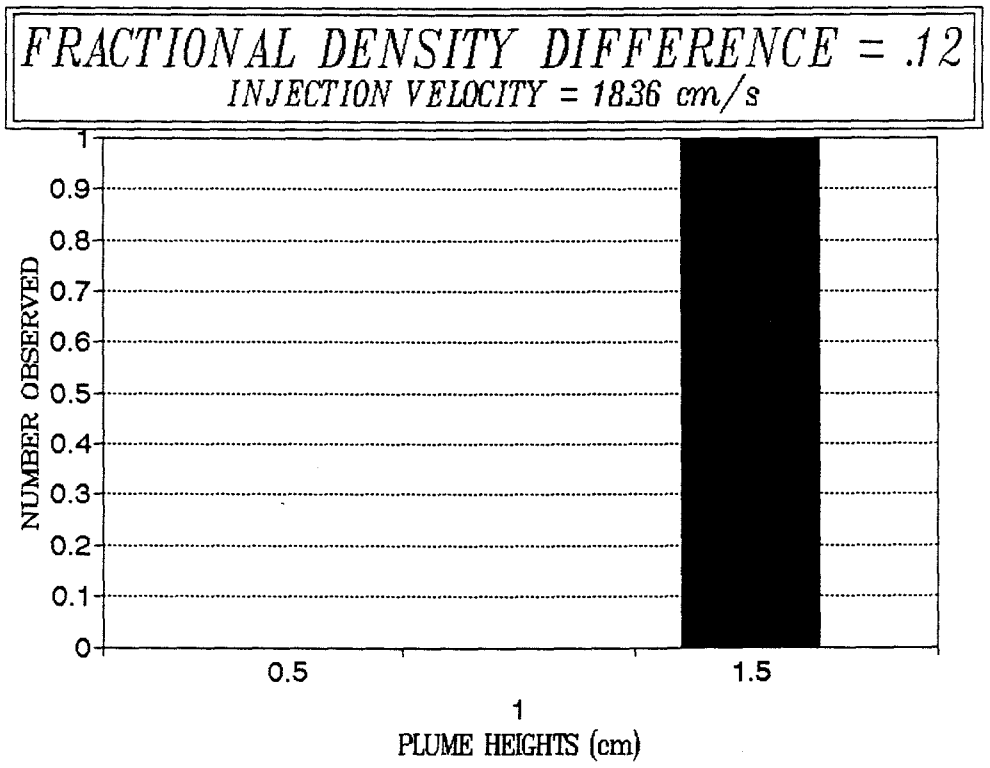
FRACTIONAL DENSITY DIFFERENCE = .12
INJECTION VELOCITY = 1836 cm/s
NUMBER OBSERVED
1
0.9
0.8
0.7
0.6
0.5
0.4
0.3
0.2
0.1
0
0.5
1.5
1
PLUME HEIGHTS (cm)

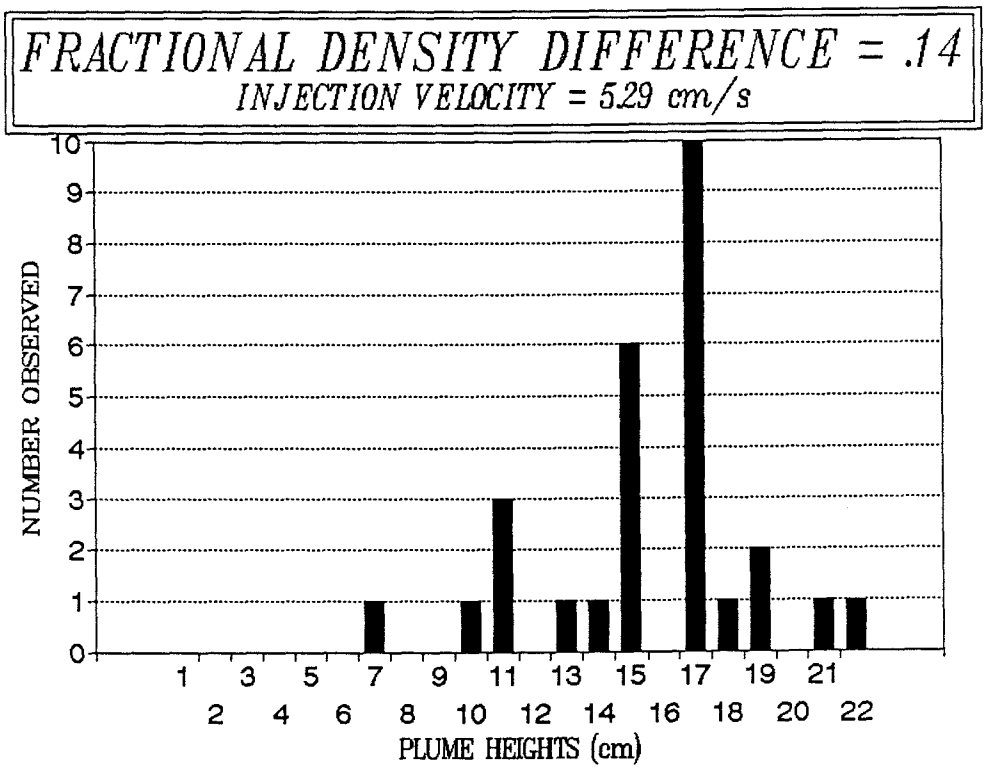
FRACTIONAL DENSITY DIFFERENCE = .14
INJECTION VELOCITY = 5.29 cm/s
NUMBER OBSERVED
0
1
2
3
4
5
6
7
8
9
10
1 2 3 4 5 6 7 8 9 10 11 12 13 14 15 16 17 18 19 20 21 22
PLUME HEIGHTS (cm)

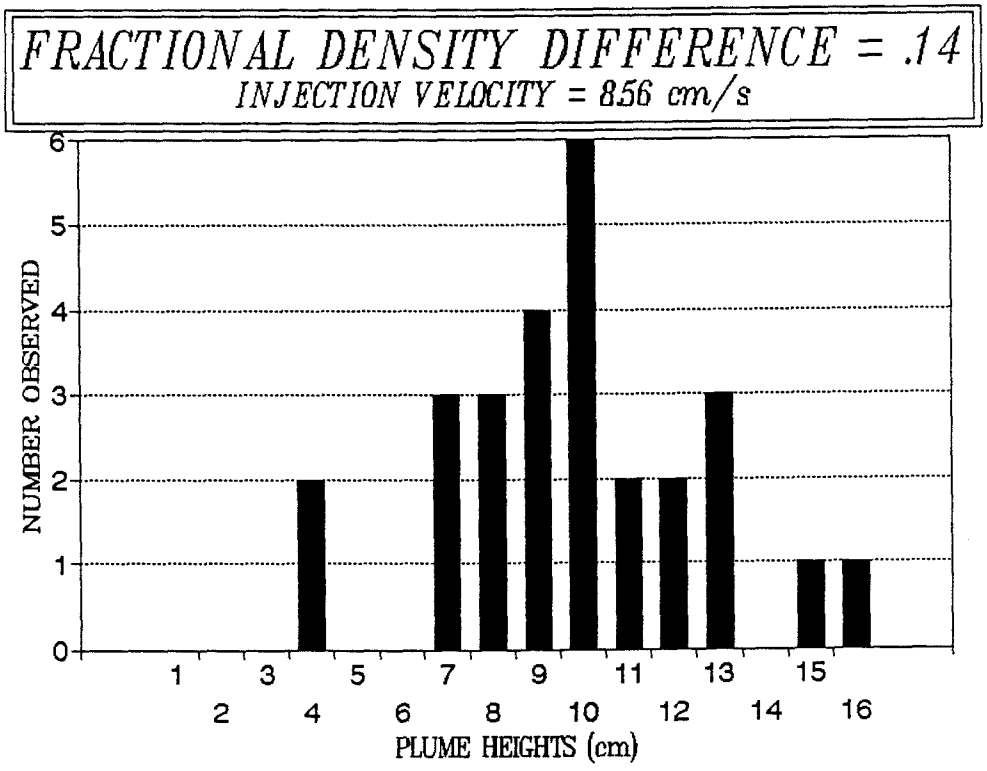
FRACTIONAL DENSITY DIFFERENCE = .14
INJECTION VELOCITY = 8.56 cm/s
NUMBER OBSERVED
0
1
2
3
4
5
6
1
2
3
4
5
6
7
8
9
10
11
12
13
14
15
16
PLUME HEIGHTS (cm)

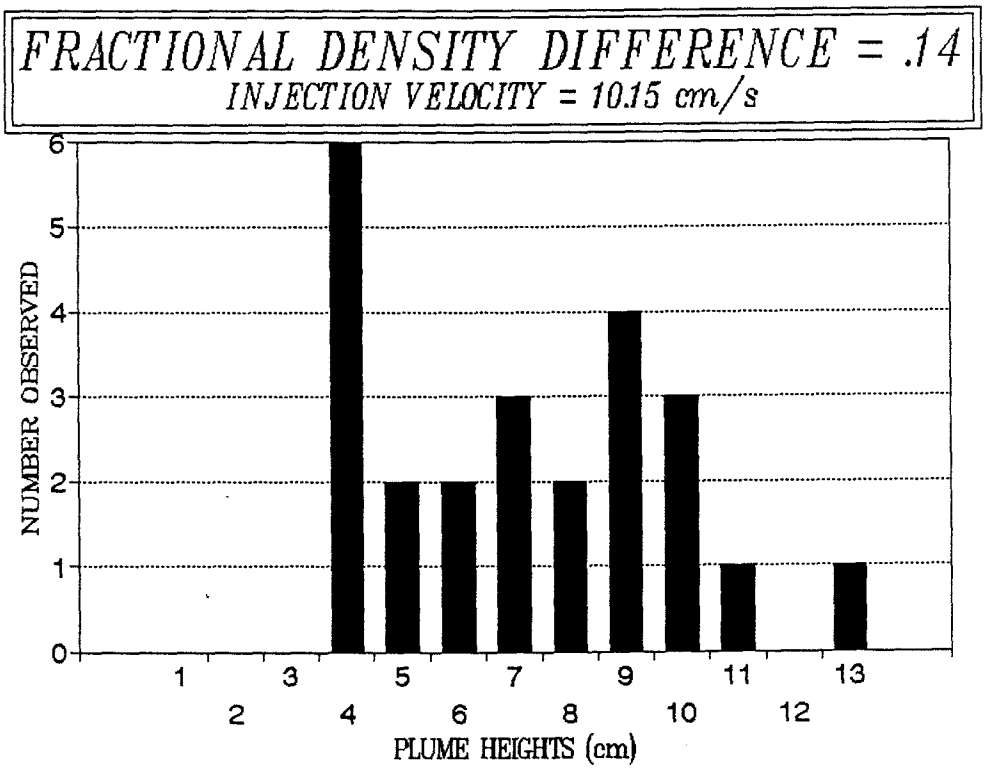
FRACTIONAL DENSITY DIFFERENCE = .14
INJECTION VELOCITY = 10.15 cm/s
NUMBER OBSERVED
0
1
2
3
4
5
6
1
2
3
4
5
6
7
8
9
10
11
12
13
PLUME HEIGHTS (cm)

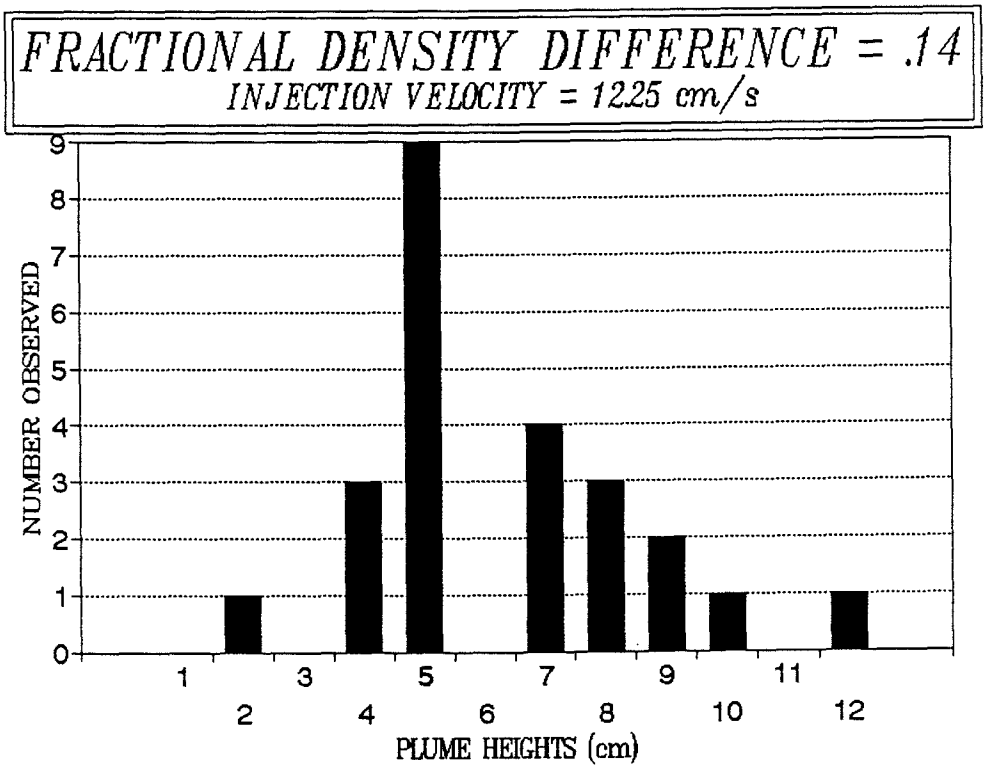
FRACTIONAL DENSITY DIFFERENCE = .14
INJECTION VELOCITY = 12.25 cm/s
NUMBER OBSERVED
0
1
2
3
4
5
6
7
8
9
1
2
3
4
5
6
7
8
9
10
11
12
PLUME HEIGHTS (cm)

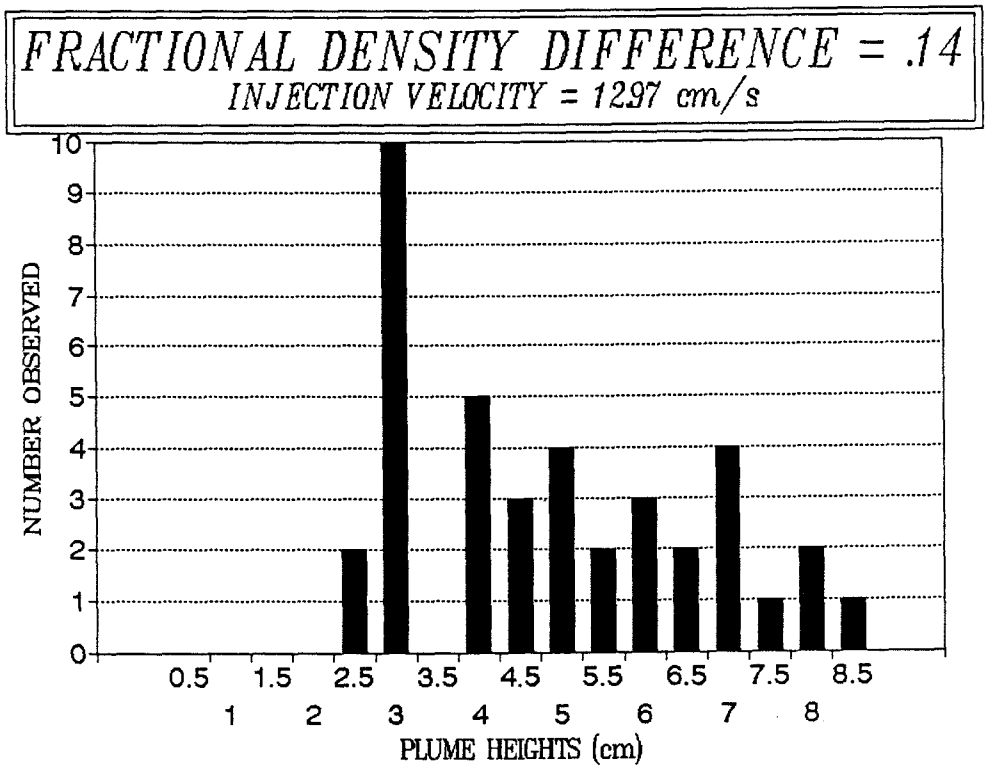
FRACTIONAL DENSITY DIFFERENCE = .14
INJECTION VELOCITY = 1297 cm/s
NUMBER OBSERVED
0
1
2
3
4
5
6
7
8
9
10
0.5
1.5
2.5
3.5
4.5
5.5
6.5
7.5
8.5
1
2
3
4
5
6
7
8
PLUME HEIGHTS (cm)

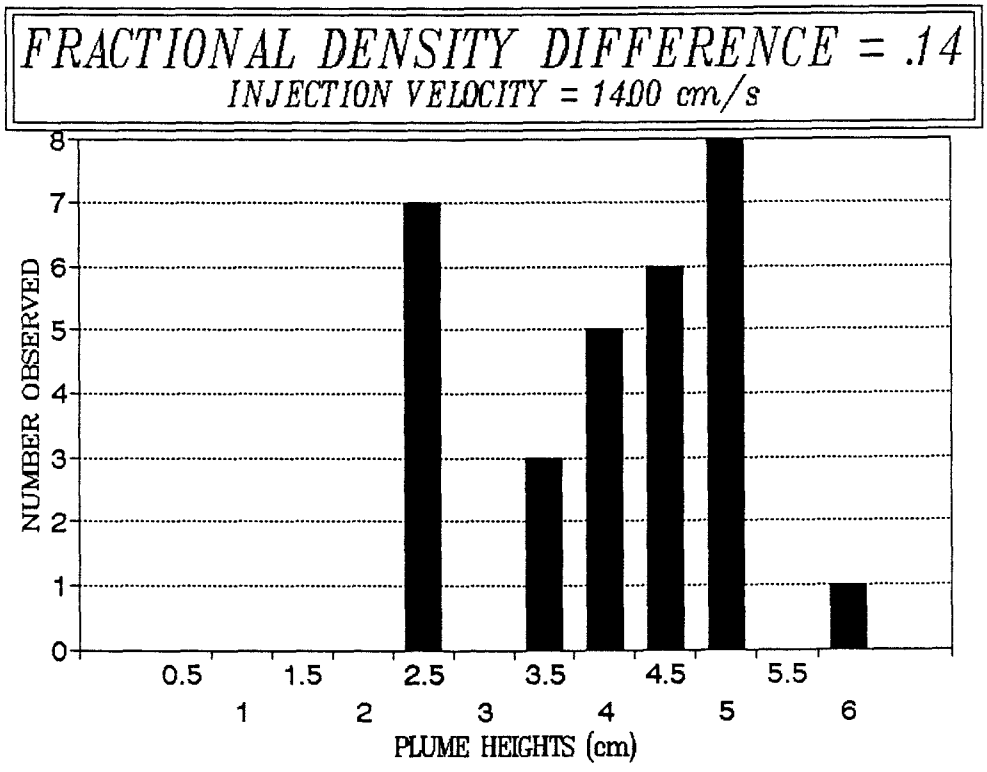
FRACTIONAL DENSITY DIFFERENCE = .14
INJECTION VELOCITY = 1400 cm/s
NUMBER OBSERVED
0
1
2
3
4
5
6
7
8
0.5
1
1.5
2
2.5
3
3.5
4
4.5
5
5.5
6
PLUME HEIGHTS (cm)

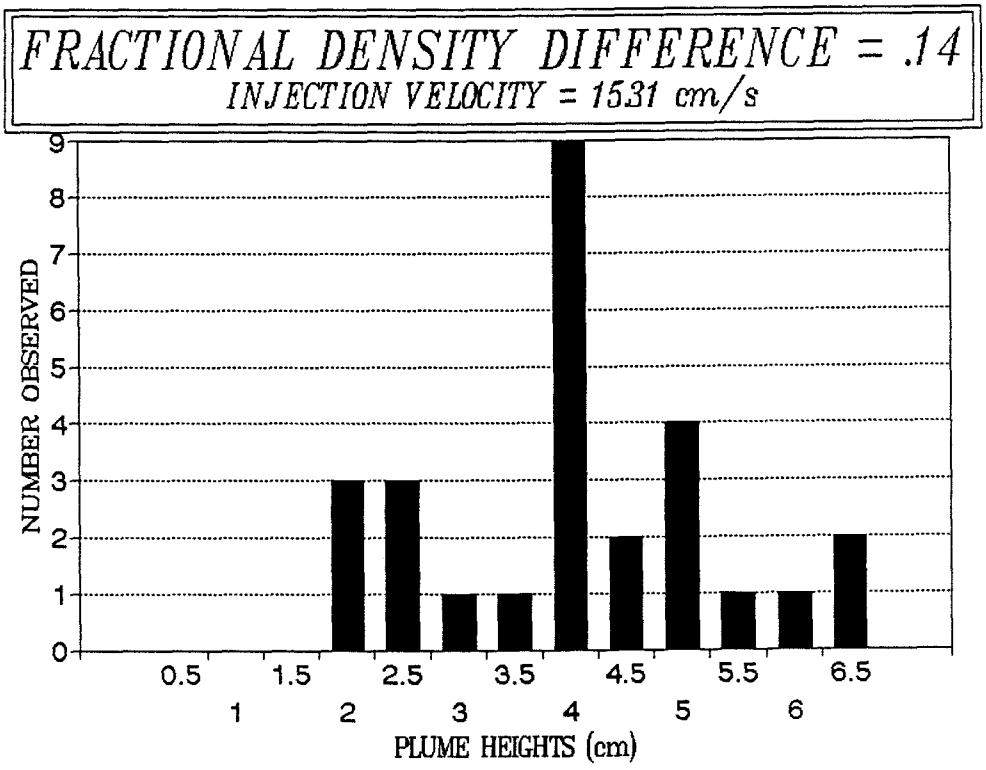
FRACTIONAL DENSITY DIFFERENCE = .14
INJECTION VELOCITY = 1531 cm/s
NUMBER OBSERVED
0
1
2
3
4
5
6
7
8
9
0.5
1.5
2.5
3.5
4.5
5.5
6.5
1
2
3
4
5
6
PLUME HEIGHTS (cm)

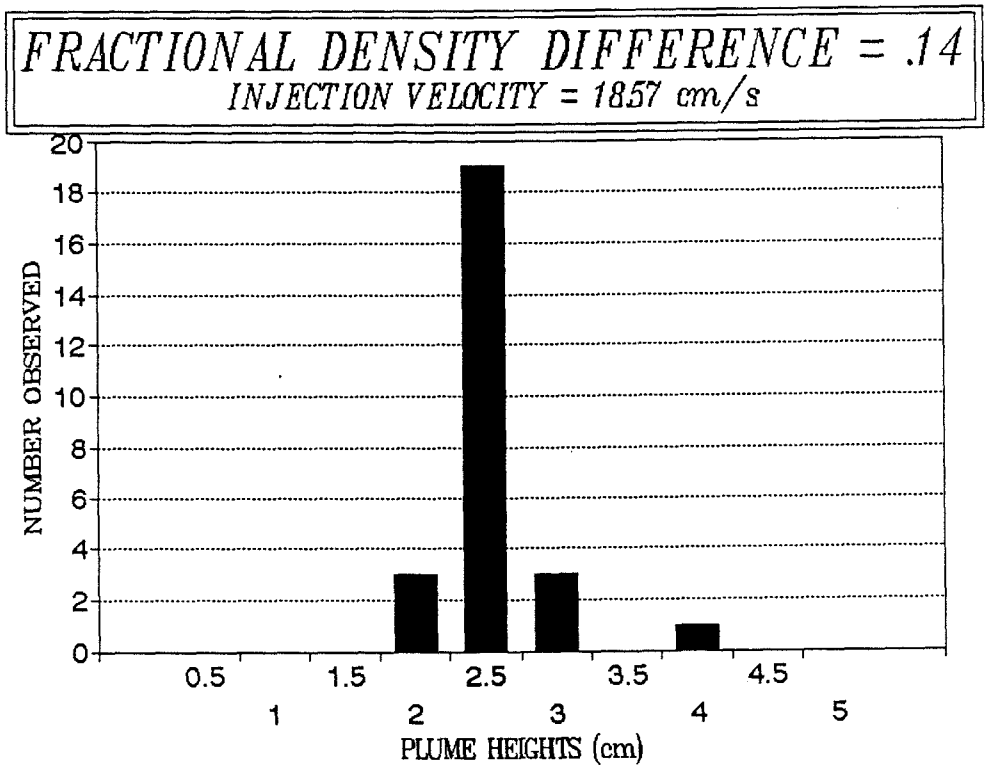
FRACTIONAL DENSITY DIFFERENCE = .14
INJECTION VELOCITY = 1857 cm/s
NUMBER OBSERVED
0
2
4
6
8
10
12
14
16
18
20
0.5
1
1.5
2
2.5
3
3.5
4
4.5
5
PLUME HEIGHTS (cm)

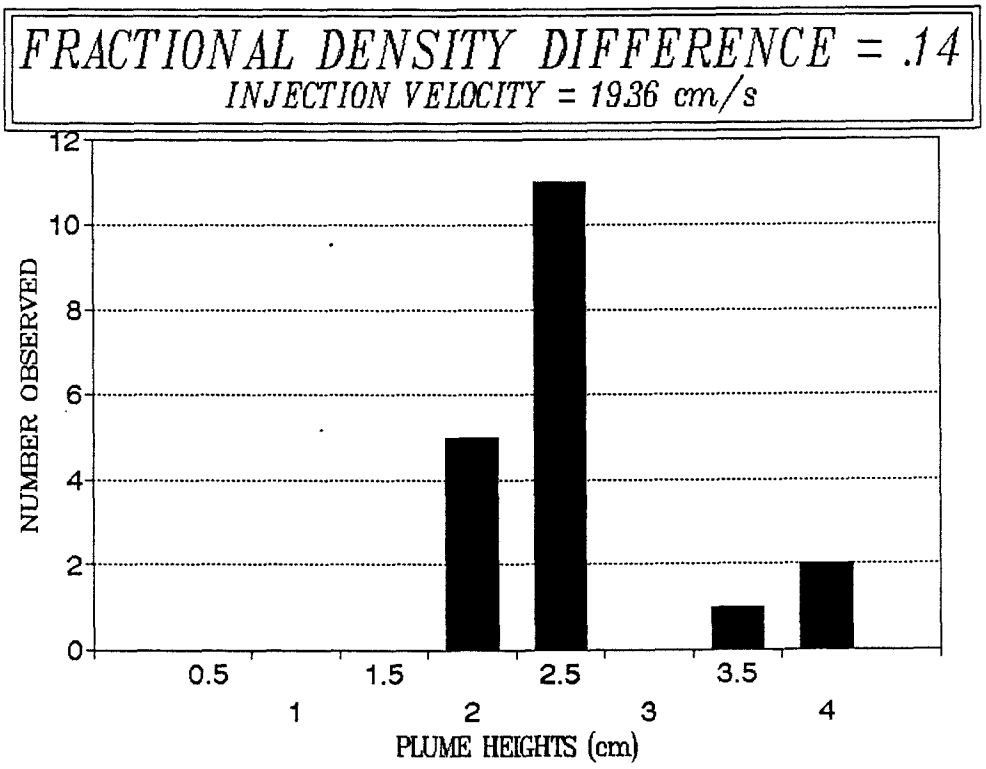
FRACTIONAL DENSITY DIFFERENCE = .14
INJECTION VELOCITY = 1936 cm/s
NUMBER OBSERVED
12
10
8
6
4
2
0
0.5
1.5
2.5
3.5
1
2
3
4
PLUME HEIGHTS (cm)

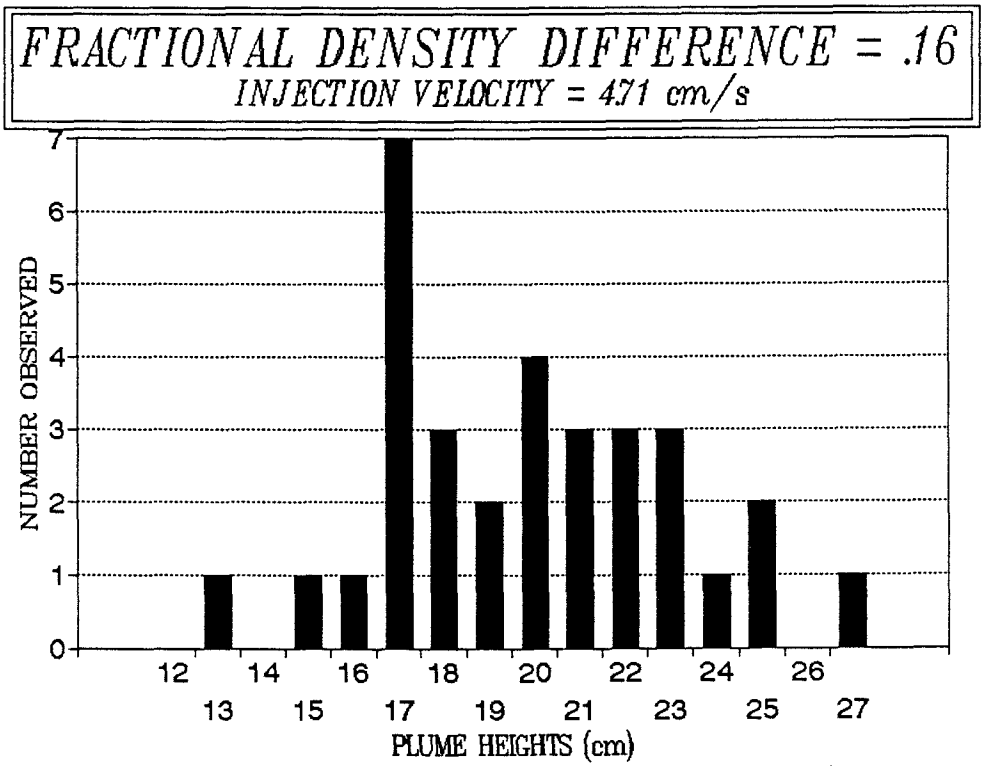
FRACTIONAL DENSITY DIFFERENCE = .16
INJECTION VELOCITY = 471 cm/s
NUMBER OBSERVED
0
1
2
3
4
5
6
7
12
13
14
15
16
17
18
19
20
21
22
23
24
25
26
27
PLUME HEIGHTS (cm)

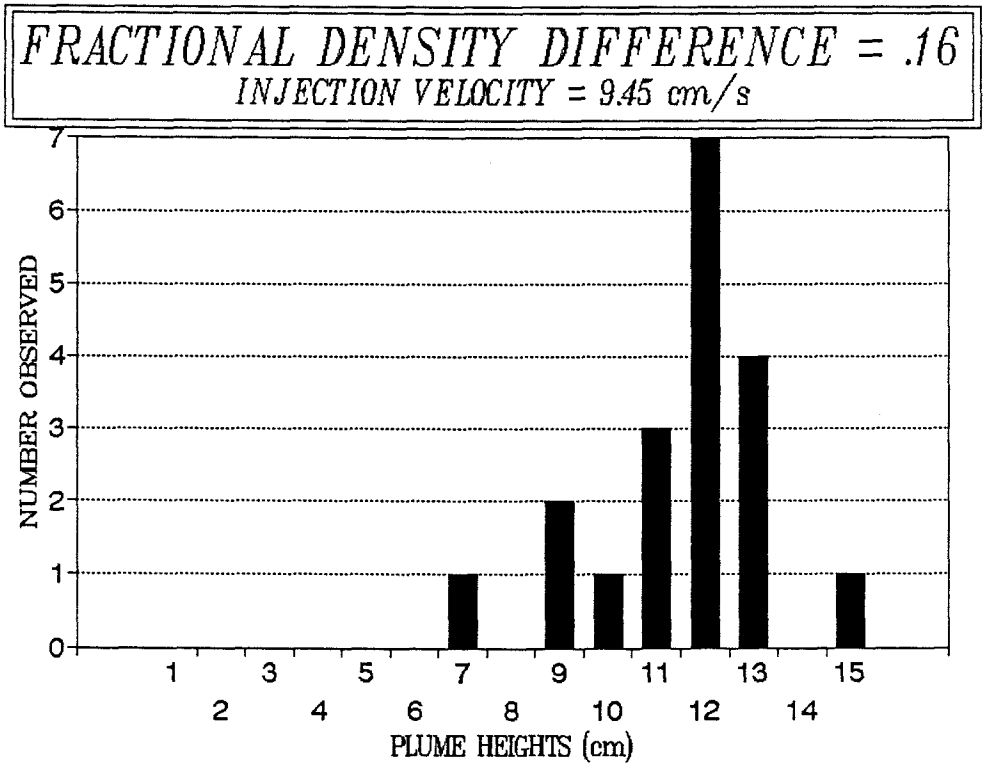
FRACTIONAL DENSITY DIFFERENCE = .16
INJECTION VELOCITY = 9.45 cm/s
NUMBER OBSERVED
0
1
2
3
4
5
6
7
1
2
3
4
5
6
7
8
9
10
11
12
13
14
15
PLUME HEIGHTS (cm)

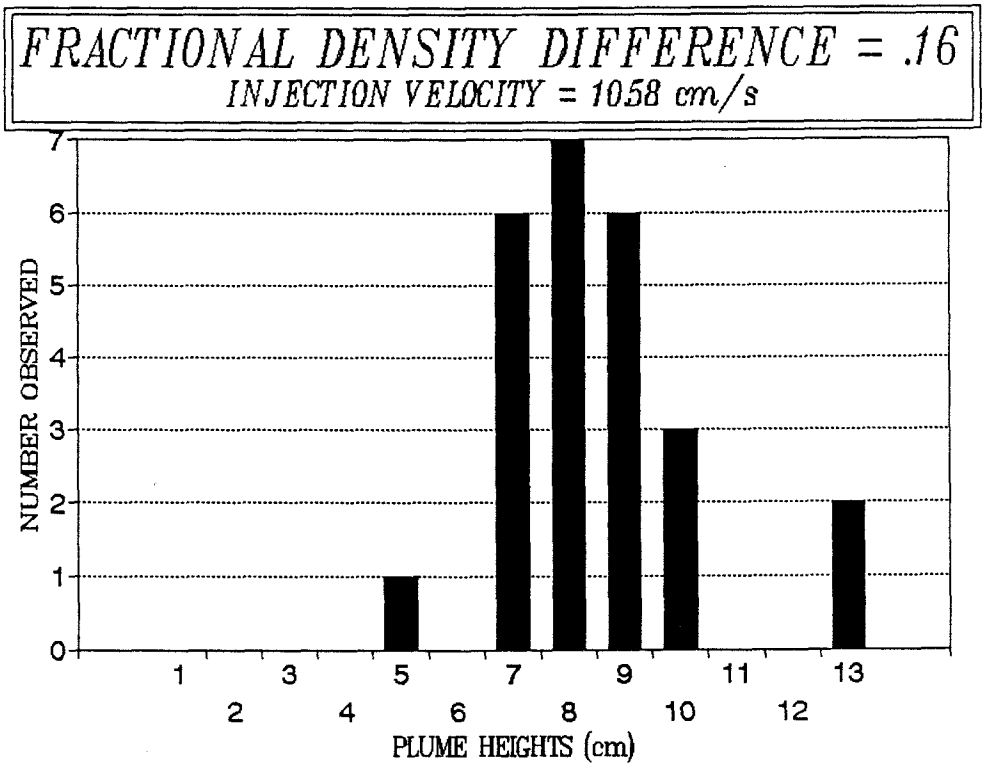
FRACTIONAL DENSITY DIFFERENCE = .16
INJECTION VELOCITY = 1058 cm/s
NUMBER OBSERVED
0
1
2
3
4
5
6
7
1
2
3
4
5
6
7
8
9
10
11
12
13
PLUME HEIGHTS (cm)

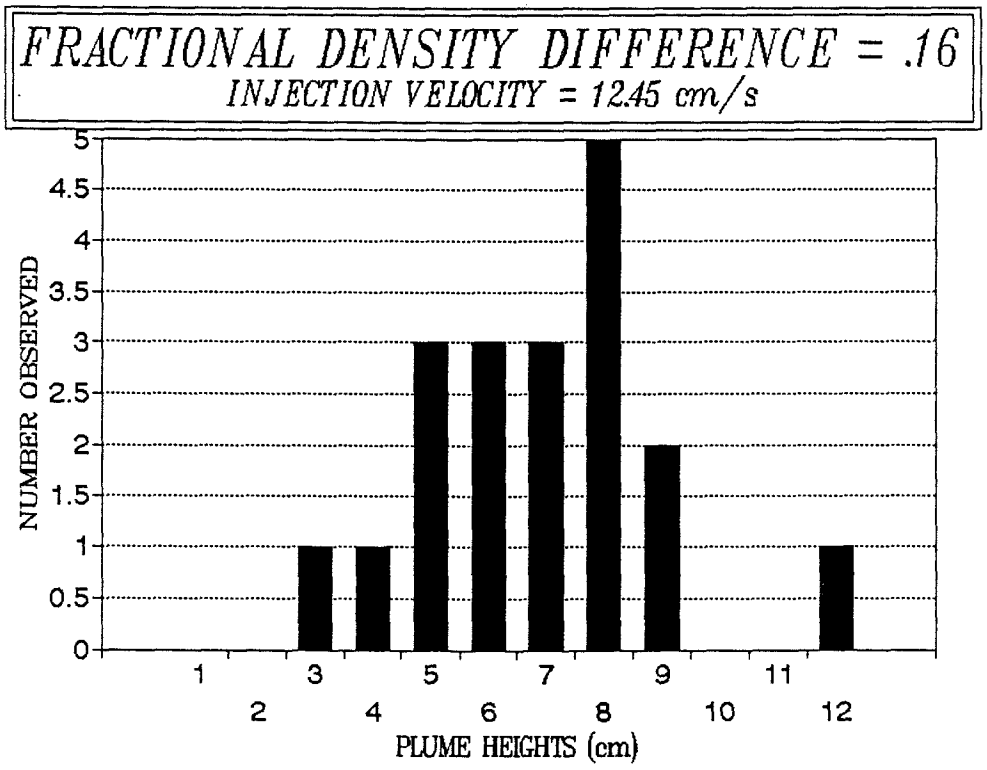
FRACTIONAL DENSITY DIFFERENCE = .16
INJECTION VELOCITY = 12.45 cm/s
NUMBER OBSERVED
0
0.5
1
1.5
2
2.5
3
3.5
4
4.5
5
1
2
3
4
5
6
7
8
9
10
11
12
PLUME HEIGHTS (cm)

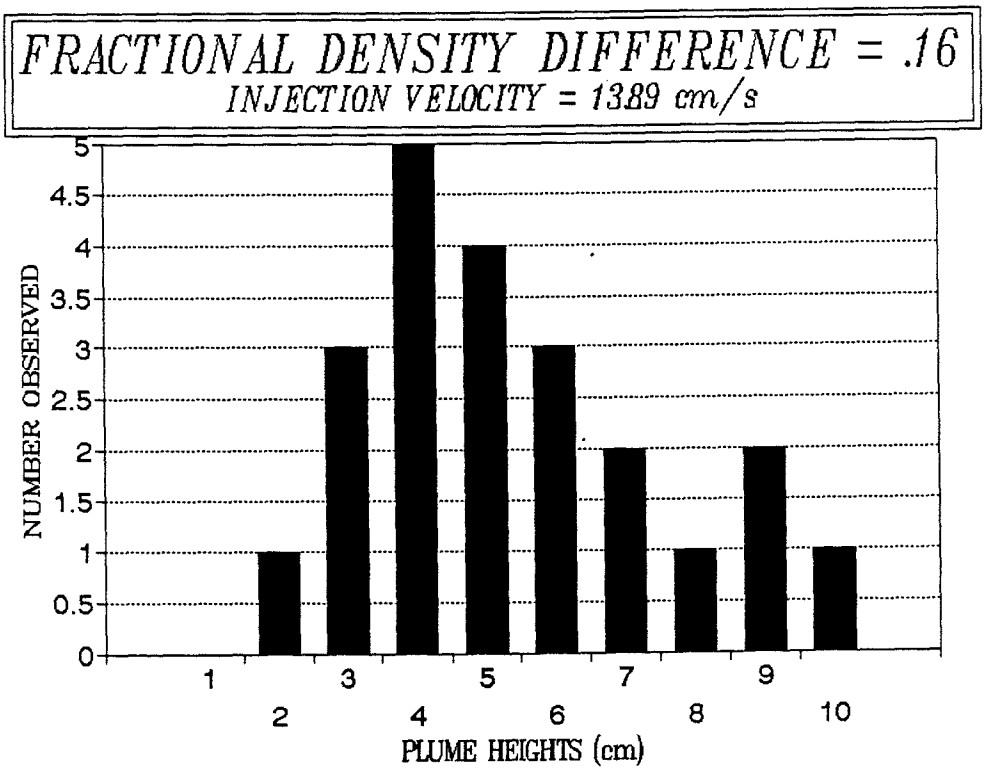
FRACTIONAL DENSITY DIFFERENCE = .16
INJECTION VELOCITY = 1389 cm/s
NUMBER OBSERVED
0
0.5
1
1.5
2
2.5
3
3.5
4
4.5
5
1
2
3
4
5
6
7
8
9
10
PLUME HEIGHTS (cm)

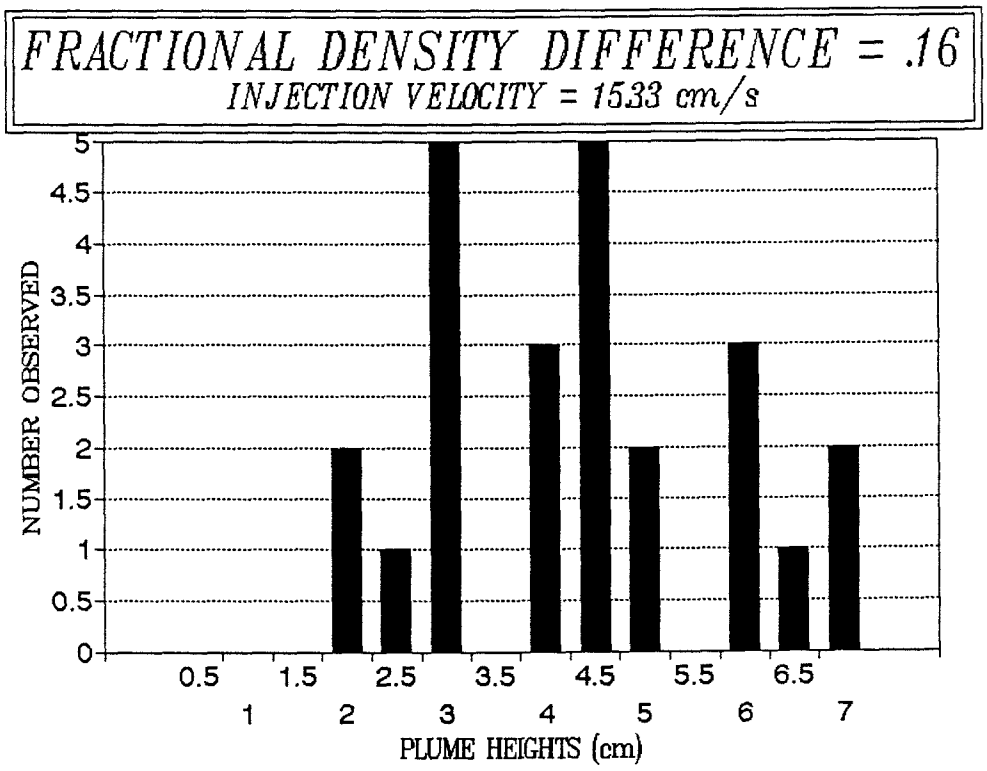
FRACTIONAL DENSITY DIFFERENCE = .16
INJECTION VELOCITY = 1533 cm/s
NUMBER OBSERVED
0
0.5
1
1.5
2
2.5
3
3.5
4
4.5
5
0.5
1
1.5
2
2.5
3
3.5
4
4.5
5
5.5
6
6.5
7
PLUME HEIGHTS (cm)

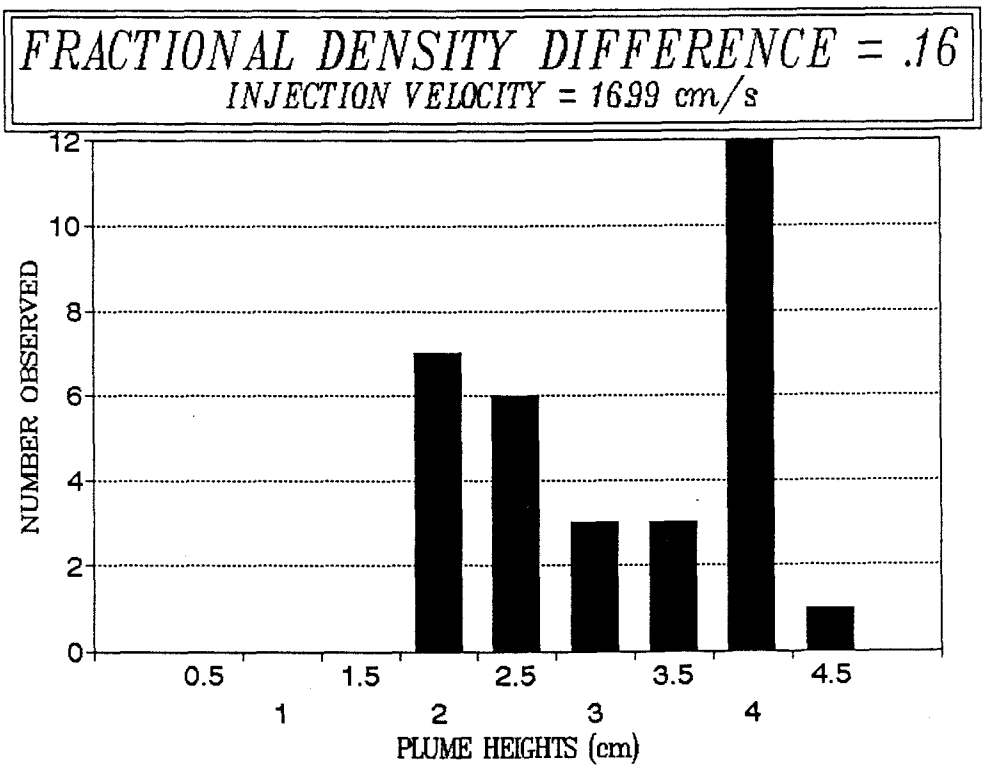
FRACTIONAL DENSITY DIFFERENCE = .16
INJECTION VELOCITY = 1699 cm/s
NUMBER OBSERVED
0
2
4
6
8
10
12
0.5
1
1.5
2
2.5
3
3.5
4
4.5
PLUME HEIGHTS (cm)

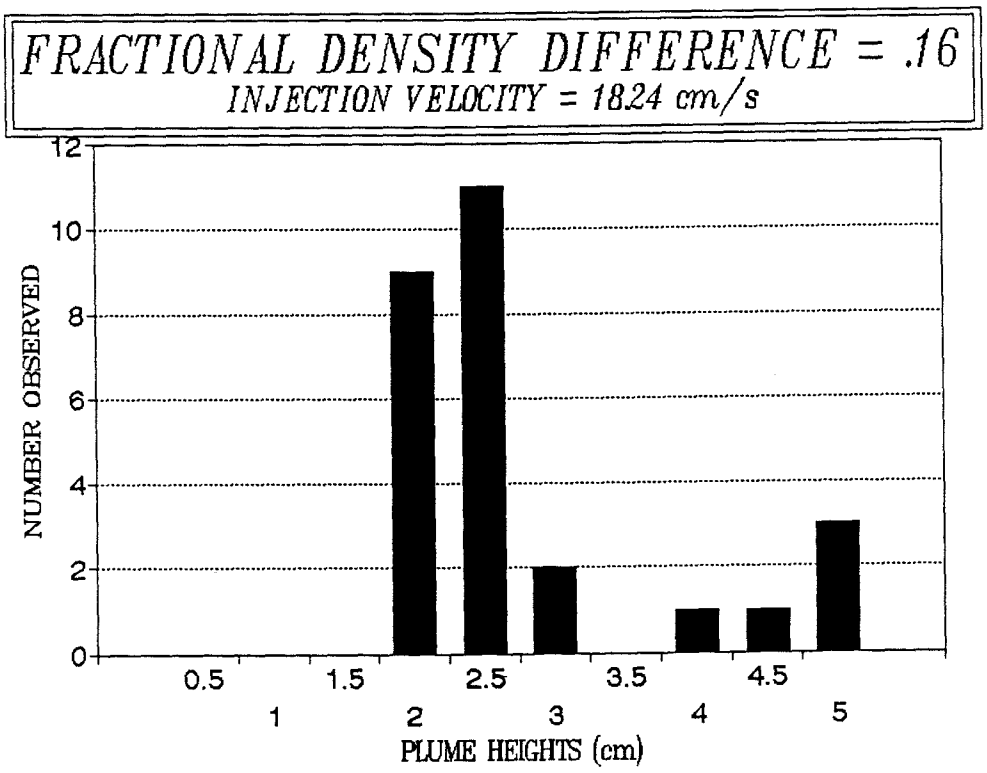
FRACTIONAL DENSITY DIFFERENCE = .16
INJECTION VELOCITY = 18.24 cm/s
NUMBER OBSERVED
0
2
4
6
8
10
12
0.5
1
1.5
2
2.5
3
3.5
4
4.5
5
PLUME HEIGHTS (cm)

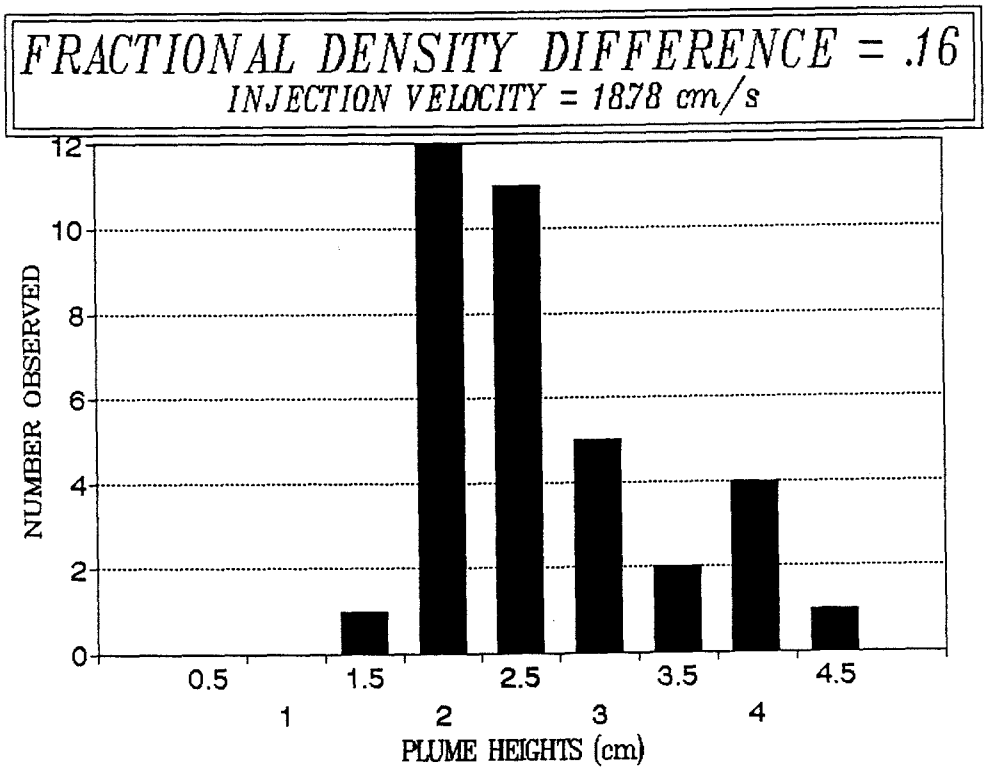
FRACTIONAL DENSITY DIFFERENCE = .16
INJECTION VELOCITY = 1878 cm/s
NUMBER OBSERVED
0
2
4
6
8
10
12
0.5
1
1.5
2
2.5
3
3.5
4
4.5
PLUME HEIGHTS (cm)

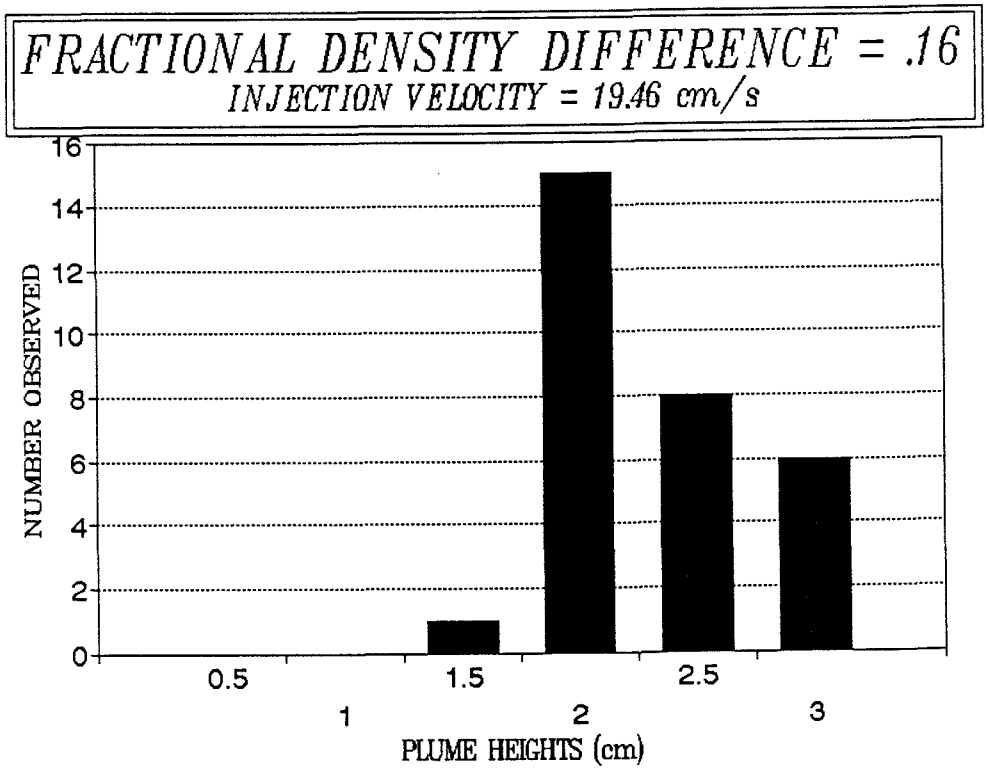
FRACTIONAL DENSITY DIFFERENCE = .16
INJECTION VELOCITY = 19.46 cm/s
NUMBER OBSERVED
16
14
12
10
8
6
4
2
0
0.5
1
1.5
2
2.5
3
PLUME HEIGHTS (cm)

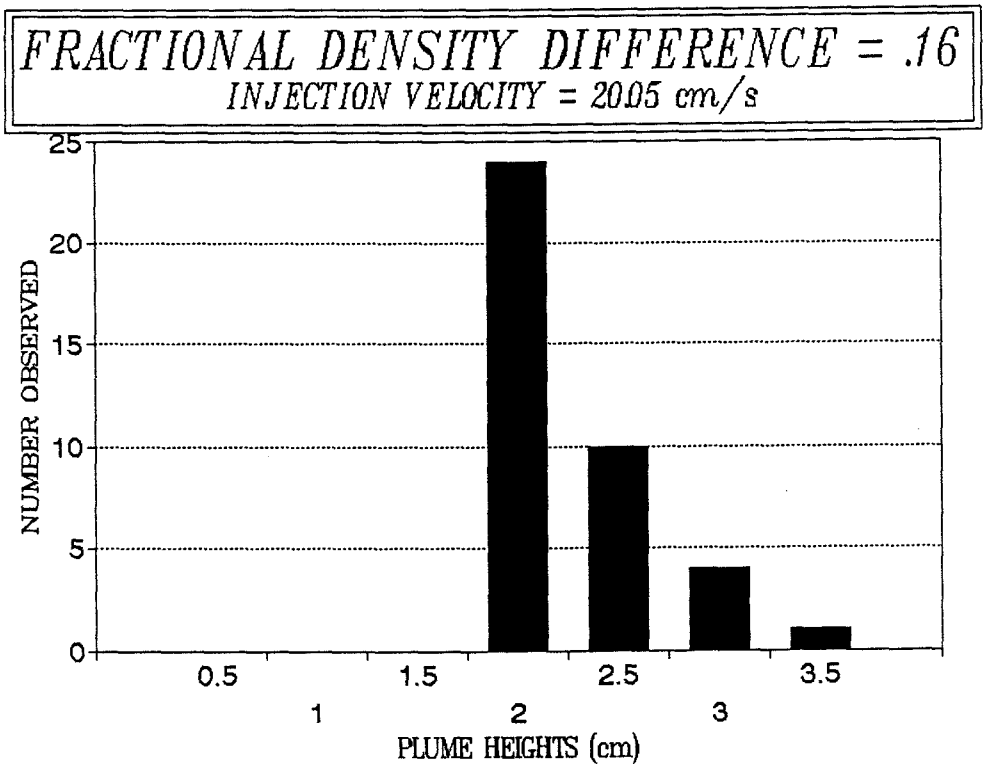
FRACTIONAL DENSITY DIFFERENCE = .16
INJECTION VELOCITY = 20.05 cm/s
NUMBER OBSERVED
25
20
15
10
5
0
0.5
1
1.5
2
2.5
3
3.5
PLUME HEIGHTS (cm)